UNIVERSIDAD DE MURCIA

FACULTAD DE MEDICINA

Adaptive Optics and Pulse Compression in Multiphoton Microscopy. Applications to Ocular Tissues

Óptica Adaptativa y Comprensión de Pulsos en Microscopía Multifotónica. Aplicaciones en Tejidos Oculares

D. Martin Skorsetz

2016

Universidad de Murcia

Departamento de Física

Laboratorio de Óptica

ADAPTIVE OPTICS AND PULSE COMPRESSION IN MULTIPHOTON MICROSCOPY. APPLICATIONS TO OCULAR TISSUES

ÓPTICA ADAPTATIVA Y COMPRESIÓN DE PULSOS EN MICROSCOPÍA MULTIFOTÓNICA. APLICACIONES EN TEJIDOS OCULARES

Doctoral Thesis presented at the Facultad de Medicina
of the Universidad de Murcia by:

Martin Skorsetz

To attain the PhD degree from the Universidad de Murcia

Junio 2016

Dr. D. Juan Manuel Bueno García, Profesor Titular de Universidad del Área de Óptica en el Departamento de Física de la Universidad de Murcia,

Dr. D. Pablo Artal Soriano, Catedrático de Universidad del Área de Óptica en el Departamento de Física,

AUTORIZAN:

La presentación de la Tesis Doctoral titulada "Adaptive optics and pulse compression in multiphoton microscopy. Applications to ocular tissues", realizado por D. Martin Skorsetz, bajo su inmediata dirección y supervisión, y que presenta para la obtención del Grado de Doctor por la Universidad de Murcia.

En Murcia, a 17 de Junio de 2016

Resumen

Durante las dos últimas décadas las técnicas de microscopía multifotónica (o no lineal), entre ellas la fluorescencia a 2 fotones (TPEF, del inglés *Two-Photon Excitacion Fluorescence*) y la generación de segundo armónico (SHG, del inglés *Second Harmonic Generation*), se han convertido en potentes herramientas para la visualización de tejidos biológicas.

Dichas técnicas permiten el registro de imágenes de capas profundas de las muestras debido a su confocalidad intrínseca. Sin embargo, las aberraciones del sistema óptico y del propio tejido limitan la calidad de la técnica. La calidad de las imágenes registradas se reduce progresivamente conforme los planos se sitúan más dentro de la muestra. La incorporación de óptica adaptativa permite la manipulación del frente de onda para minimizar el impacto de dichas aberraciones y restaurar la calidad de imágenes.

Por otra parte, la dispersión óptica de los componentes del microscopio así como de la propia muestra, hacen que las componentes espectrales de los pulsos ultracortos utilizados viajen a diferentes velocidades. Esto se traduce en un ensanchamiento temporal de los pulsos que reduce la eficiencia de los procesos multifotónicos. Para compensar estos efectos de dispersión normalmente se utilizan los compresores de pulsos, capaces de modificar la fase de los diferentes componentes de frecuencia de los pulsos y comprimirlo temporalmente.

En ese sentido la presente Tesis Doctoral se concentra en mejorar las imágenes de microscopia multifotónica mediante manipulaciones espaciales y temporales de un haz láser ultrarrápido ultraintenso por medio de la corrección de aberraciones y la compresión de pulsos, respectivamente. Para corregir el frente de onda se ha utilizado un modulador espacial de cristal líquido y un espejo deformable. Para optimizar las propiedades temporales de los pulsos de luz se ha empleado un compresor de pulsos variable. Se ha prestado especial atención a los efectos producidos en las imágenes multifotónicas de los tejidos oculares.

Los principales objetivos de este trabajo son los siguientes:

- Manipulación controlada del frente de onda del haz láser para mejorar plano a plano las imágenes de microscopía multifónica de tejidos gruesos.
- Análisis de los efectos de diferentes parámetros sobre la corrección de la frente de onda: profundidad del plano, tamaño de la imagen registrada y secuencia de los coeficientes de Zernike utilizados.
- Estudio del efecto de la aberración esférica en función de la profundidad de la muestra.
- Determinación de un valor global de aberración esférica que permita la optimización de imágenes multifotónicas de muestras gruesas enteras y así evitar correcciones individuales plano a plano.

- Pre-compensación temporal del pulso para mejorar la calidad de las imágenes de microscopía multifotónica.
- Evaluación de la reducción de la potencia del láser necesaria para minimizar el daño en muestras biológicas durante el uso de la compresión de pulsos.

Estructura de la Tesis

La presente Tesis Doctoral se divide en 6 capítulos que se describen de forma somera a continuación.

El ***Capítulo 1*** incluye una descripción general de las diferentes técnicas de microscopía, especialmente de la microscopía multifotónica, así como de los láseres de femtosegundos. También se revisan los conceptos de óptica adaptativa y de compresión temporal de pulsos.

En el ***Capítulo 2*** se describe el microscopio multifotónico aquí utilizado. El sistema combina un microscopio invertido con un láser de femtosegundos, una unidad de escaneo, un motor-Z y una unidad de detección. Las señales TPEF y SHG se registraron en reflexión utilizando un objetivo de no inmersión.

El ***Capítulo 3*** se centra en el desarrollo de una técnica de óptica adaptativa sin sensor de frente de onda utilizando un algoritmo de tipo *hill-climbing* (o "aproximaciones sucesivas") con el objeto de mejorar la calidad de las imágenes obtenidas con el microscopio multifotónico descrito en el Capítulo 2. Como elemento adaptativo se utiliza un modulador espacial de cristal líquido con el que se generan los modos de Zernike de forma sistemática durante el registro de imágenes.

Un método alternativo para aumentar la profundidad de foco en microscopía multifotónica se presenta en el ***Capítulo 4***. La técnica se basa en la manipulación del patrón de aberración esférica del haz incidente con un módulo de óptica adaptativa utilizando un espejo deformable y un sensor de Hartmann-Shack.

En el ***Capítulo 5*** se estudian de los efectos sobre la calidad de las imágenes multifotónicas de una técnica de pre-compresión temporal de pulsos a través de un compresor variable formado por una pareja de prismas. La configuración óptima del compresor de pulsos se determinará con un procedimiento basado en el registro de tomografías de las muestras bajo estudio. Adicionalmente, se presenta un método simple basado en la reducción de la potencia del láser para evitar producir daño sobre las muestras biológicas cuando se utilizan técnicas de compresión de pulsos.

Finalmente el ***Capítulo 6*** contiene las conclusiones de este trabajo.

Conclusiones de la Tesis

1. Se ha desarrollado un microscopio multifotónico que incluye un modulador espacial de cristal líquido en la vía de iluminación para corregir plano a plano las aberraciones inducidas por la muestra. El procedimiento experimental se basa en una técnica de óptica adaptativa sin sensor de frente de onda y un algoritmo tipo *hill-climbing*. A pesar de utilizar un objetivo en aire con baja apertura numérica y una configuración de microscopio en reflexión, el método es capaz de generar imágenes TPEF y SHG con calidad notablemente mayor.

2. Aunque la corrección de óptica adaptativa es particular para cada muestra, la cantidad de aberración aumenta linealmente con la profundidad. Por otra parte, el frente de onda que optimiza la imagen en una zona determinada no depende del área registrada. Sin embargo, esto puede depender de la estructura de la muestra y la profundidad del plano de interés.

3. La combinación de los modos de Zernike que optimiza la imagen multifotónica depende de la secuencia de control de la corrección. El algoritmo *hill-climbing* es eficiente para ambas direcciones creciente y decreciente. Aunque los mapas de aberración óptimos difieren entre ambas secuencias de control, las imágenes finales mejoradas son similares.

4. Se encontró que la aberración esférica es el término de aberración dominante, especialmente en los planos más profundos de las muestras. La contribución de este término de aberración es tal, que las imágenes que proporciona son de calidad similar a las obtenidas cuando se tiene en cuenta también otros términos como el coma y el astigmatismo.

5. Se ha utilizado un módulo de óptica adaptativa compuesto por un sensor de Hartmann-Shack y un espejo deformable para manipular el patrón de aberración esférica del haz láser incidente e incrementar la profundidad de foco.

6. Utilizando imágenes de tomografía rápida se determinó un patrón de aberración esférica único y óptimo que evita la corrección plano a plano. Un único valor de aberración esférica reduce la calidad de imagen de los planos más superficiales. Sin embargo las imágenes en las capas más profundas mejoran con respecto a las condiciones originales.

7. Para pre-compensar la dispersión de los pulsos láser producidos por la óptica del microscopio y la muestra se ha usado un compresor de pulsos variable. Esta operación aumenta la eficiencia de los procesos multifotónicos de forma que las señales TPEF y SHG aumentan un factor 2x o más.

8. El estado de compresión óptimo que proporciona la mejor imagen depende de la muestra, pero para cada una de ellas es constante con la profundidad.

9. Esta operación de compresión de pulsos permite la reducción de la potencia del láser de iluminación, lo que minimiza los posibles efectos secundarios no controlados de daño térmico o de foto-blanqueo (del inglés *photo-bleaching*). Esto es de vital importancia en muestras

biológicas, más propensas a este tipo de daño. Los resultados muestran que la operación de compresión permite una reducción de la potencia de aproximadamente un 50%.

Índice

Summary

During the last two decades multiphoton (or nonlinear) microscopy, including two photon excitation fluorescence (TPEF) and second harmonic generation (SHG), has become a powerful tool for visualization of biological tissue.

Such techniques allow the registration of images of deeper layers of the samples due to their inherently confocality. However, aberrations in the optical system and the specimen-induced ones limit the quality of this technique. The quality of the recorded images is progressively reduced when imaging deeper layers within the sample. The implementation of adaptive optics techniques allows the manipulation of the wavefront to minimize the impact of those aberrations and restore the quality of the images.

Furthermore, the optical dispersion of the microscope components and the sample itself also affect the imaging recording technique. Due to this, different frequency components of the ultrashort pulses travel at different speed through the optics of the microscope. This leads to a temporal broadening of the pulses, which reduces the efficiency of multiphoton processes. To compensate for these dispersion effects pulse compressors are usually used, which are able to modify the phase of the different frequency components of the pulse.

In that sense, this Doctoral Thesis is focused on improving multiphoton microscopy images by spatial and temporal beam manipulations of the ultra-fast ultra-intense laser beam through the correction of aberrations and pulse compression, respectively. To correct the wavefront, both a liquid-crystal spatial light modulator and a deformable mirror were used. To optimize the temporal properties of the pulses, a variable pulse compressor has been employed. Particular attention has been paid to the effects on multiphoton images of ocular tissues.

Table of contents

List of abbreviations

AO	adaptive optics
DM	deformable mirror
DOF	depth of focus
ERM	epiretinal membrane
fs	femtosecond
HS	Hartmann-Shack
LCoS	liquid-crystal on silicon
MP	multiphoton
PCS	pulse compression state
RMS	root-mean squared
SA	spherical aberration
SHG	second harmonic generation
SLM	spatial light modulator
TPEF	two-photon excitation fluorescence
WA	wavefront aberration
WFSL	wavefront sensor-less

CHAPTER 1

INTRODUCTION

This introductory chapter gives an overview of the different microscope techniques with special emphasis on multiphoton (MP) microscopy and the high-power ultrafast laser systems behind it. The concepts of adaptive optics (AO) and pulse compression are also revised. Finally, the motivation and goal of this Thesis as well as the outline of the present work are also presented.

1.1. Principles and types of microscopy

Microscopy is the technical and research field where microscopes are used to image samples and objects which cannot be seen with the "naked eye". Early microscopes only magnified the object under investigation. The oldest designs of microscopes are from the 17th century. Antoni van Leeuwenhoek (1632-1732), a Dutch cloth merchant and amateur scientist, used only a single glass lens in his simple microscope to observe blood cells, bacteria and microorganisms. Robert Hooke (1635-1703) used a compound microscope, composed of two lenses.

Light microscopy (or optical microscopy) has become one of the most useful tools in medicine and biology. The most common type of microscopy in this kind of research is fluorescent microscopy (Pawley, 1995). Other microscopy techniques, such as scanning electron microscopy, do not use visible light to illuminate the sample under study.

In order to get high resolution optical imaging, scientists have developed various techniques, including wide-field, confocal and MP microscopy. Compared to the rest, the latter presents several advantages as it will be explained in this chapter.

1.1.1. Linear (wide-field) fluorescence microscopy

Fluorescence consists of the molecular absorption of light energy at one wavelength and reemission of a longer wavelength. In a general sense, it is known as linear microscopy since only one photon is absorbed by the molecule at a time. This process can typically be illustrated by the Jablonski energy diagram (Figure 1.1(a)). The electron at the ground level gains energy by absorbing one photon and "jumps up" to a higher level. Then, this excited electron loses some of that energy and "jumps back" to the ground level by emitting another photon. Due to the loss of energy at the upper levels, the emitted light is always of longer wavelength than the excitation one. This shift between excitation and emission is known as Stokes' shift (Figure 1.1(b)).

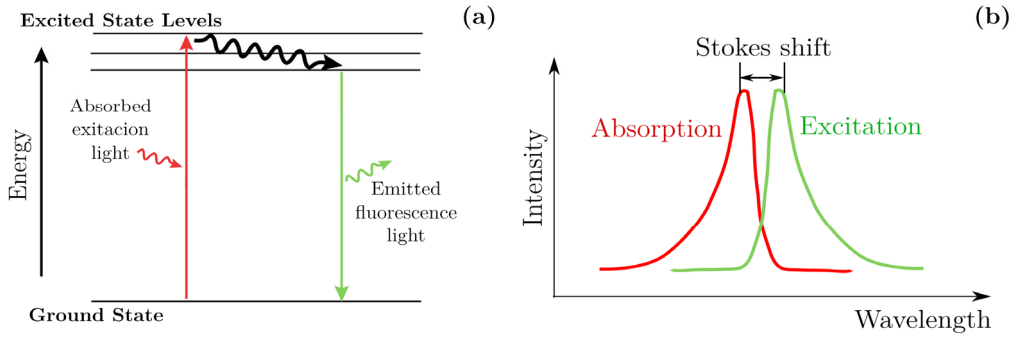

Figure 1.1: (a) Jablonski diagram representing the typical process of molecular fluorescence. (b) Stokes' shift produced during the event of fluorescence.

Wide-field (or bright-field) microscopy is the most widely used fluorescence microscopy technique where the entire specimen is uniformly illuminated. The source of light is usually a mercury or xenon lamp. The excitation wavelength can be selected by an excitation filter. UV or blue-green excitation wavelengths are often used. A dichroic mirror separates the excitation wavelengths from the fluorescent radiation. The emitted light passes once again the dichroic mirror, the emission filter and reaches the detector (eye, CCD,...) as shown in Figure 1.2.

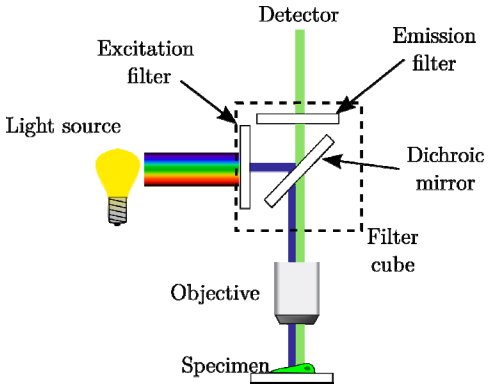

Figure 1.2: Schematic of a fluorescence microscope. Adapted from (Cristóbal *et al.*, 2011).

The out-of-focus signal is noticeable and an inherently limitation. Although this provides poor axial resolution, this technique offers live cell imaging when combined with sensitive detection systems. Furthermore, due to highly sensitive cameras, wide-field techniques often require lower energy of excitation light than other laser scanning techniques. Nowadays fluorescence microscopy is often used in biomedical research and it is the basis of one of MP microscopy techniques, as it will be shown in the following sections.

1.1.2. Confocal laser scanning microscopy

Confocal microscopy was developed with the aim to reduce some limitations of the traditional fluorescence microscopes (mainly out-of-focus light). In a conventional wide-field microscope all parts of the specimen are excited at the same time. Then, the detected light (fluorescence) includes light coming from sample's planes located both behind and in front of the imaged plane. This unwanted light contributes as a background, reducing the quality of the recorded image. In contrast, and in order to eliminate the out-of-focus signal, a confocal microscope uses a pinhole in front of the detector in an optically conjugated plane with the imaged plane (Figure 1.3). To illuminate the sample under study, a XY raster scan is used. The experimental system is usually named as confocal scanning laser microscope.

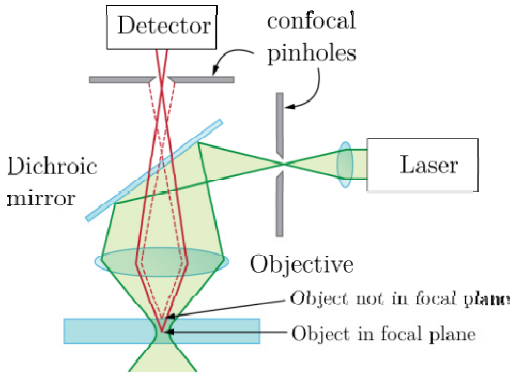

Figure 1.3: Confocality principle. The-out-of-focus light (red dotted lines) is eliminated by the (confocal) pinhole. Only signal from the focal plane (red solid lines) reaches the detector. Different depth positions can be driven by a stepper motor that changes the position of the aperture in Z-direction. Adapted from (Cox, 2002).

Figure 1.4 compares images of a mouse intestine sample recorded with both wide-field and confocal microscopy. With the former, the signal from the focal plane is mixed with light from other planes and the final image appears blurred. In the confocal image, the signal contributing to the image comes only from a single plane what makes this appear much sharper.

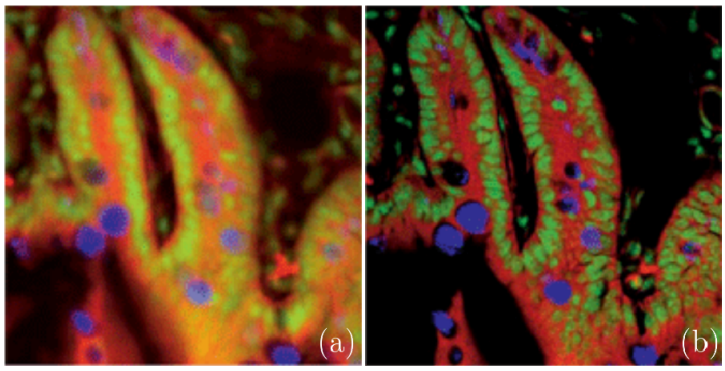

Figure 1.4: Comparison of a wide-field microscopy fluorescent (a) and a confocal laser scanning microscope image (b) of a mouse intestine. Figure adapted from Carl Zeiss web site.

1.1.3. Non-linear microscopy: two-photon excitation fluorescence and second harmonic generation

Non-linear (or in general, MP) microscopy can be achieved when the sample under study absorbs two or more photons instead of one. Two-photon absorption process was first described by Maria Göppert-Mayer in her doctoral dissertation in 1931 (Göppert-Mayer, 1931). This early description was just a theoretical hypothesis and it did not come true until the invention of ultrafast high power lasers. This was due to the fact that non-linear processes require a high flux of photons concentrated in a "very small" volume (~ one femtoliter). This can be achieved using those ultrafast (femtosecond, fs) laser systems (usually Ti-Sapphire

lasers). Whereas linear (single-photon) fluorescence is proportional to the illumination intensity, MP signal is proportional to the square of the incident intensity.

The simplest case of this type of non-linear microscopy is the so called two-photon excitation fluorescence (TPEF). In this technique there is a quasi-simultaneous absorption of two photons of identical frequencies (in the infrared range) that excites a molecule from a ground state to a higher energy electronic state. Later, a unique photon (in the visible range) is emitted. This emitted photon has a wavelength "a little" longer than half of the incident photons. This process is presented in Figure 1.5 by means of the Jablonski diagram and compared to the process involving one-photon absorption (i.e. linear or single-photon fluorescence).

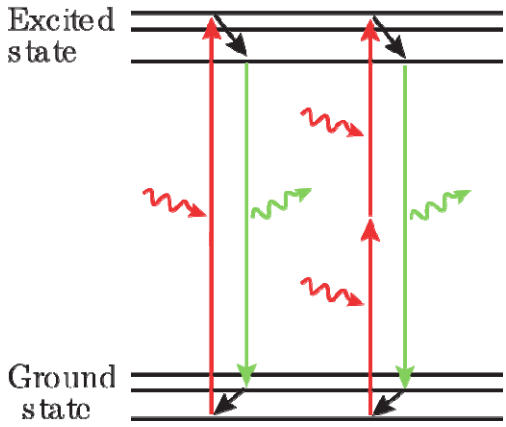

Figure 1.5: Jablonski diagram illustrating single photon (left) and two-photon absorption (right). Adapted from (Helmchen and Denk, 2005).

TPEF was experimental demonstrated in Cornell University (Denk *et al.*, 1990). At that time the authors combined advanced laser systems and scanning techniques to observe specimens under infrared wavelength two-photon excitation. Compared to linear fluorescence, TPEF microscopy presents advantages such as:

(1) Non-linear signal is only produced in the focal volume, what provides intrinsic confocality (pinholes are not necessary) and inherent optical sectioning (see Figure 1.6).

(2) Photo-toxicity and side effects due to photo-bleaching are minimized.

(3) The use of infrared light allows deeper penetration (i.e. lower scattering) within the tissues under analysis.

(4) Since TPEF detects endogenous signal, samples do not require staining procedures or the use of markers.

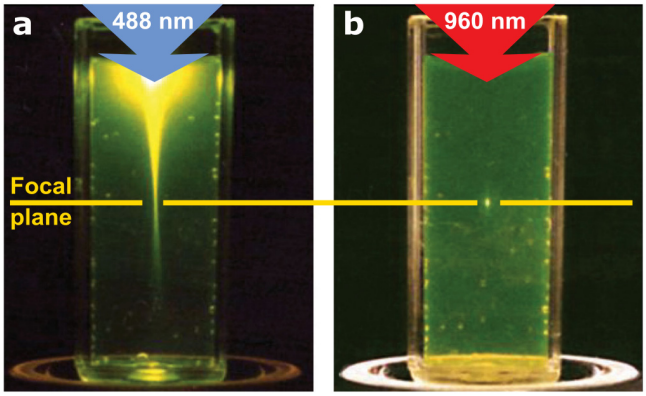

Figure 1.6: Direct comparison of linear fluorescence (left) and TPEF (right). The linear fluorescence generated along the focusing cone of the illumination pathway can be observed, what significantly reduces the performance of the imaging technique. In TPEF only signal from the focal volume is observed (Zipfel *et al.*, 2003).

Another type of MP process is known as Second Harmonic Generation (SHG). In SHG, the interaction of two photons with a non-linear material creates a new photon with twice the energy and half the wavelength of the incident light. The pair of absorbed photons goes up to a virtual energy state what implies that there is no energy loss. Figure 1.7 presents a comparison of single-photon, TPEF and SHG processes. SHG signal is sensitive to non-centrosymmetric spatial arrangements such as collagen structures. The lack of a center of symmetry in an organized material presents a strong SHG efficiency (Campagnola *et al.*, 2001).

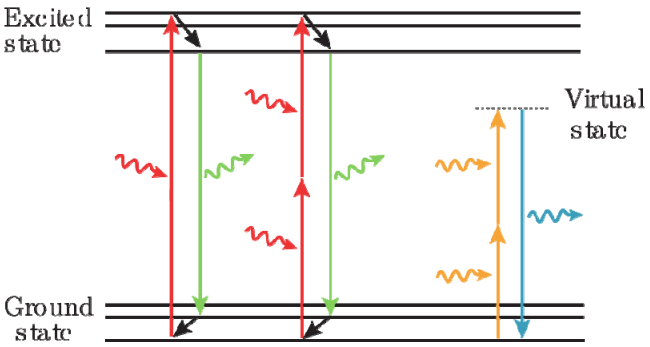

Figure 1.7: Schematic comparison of linear fluorescence, TPEF and SHG. Adapted from (Helmchen and Denk, 2005).

TPEF and SHG are the most commonly used MP techniques. When imaging a tissue under MP microscopy both signals must be separated out. For these, spectral filters are used: broad and narrow band respectively. The corresponding emission spectra for an excitation light of 850 nm are shown in the schematic of Figure 1.8. As already explained, the SHG signal has exactly half of the wavelength of the excitation light. TPEF signal is commonly located in the 450–600 nm range. Since the emission spectra do not overlap, both signals can be analyzed independently.

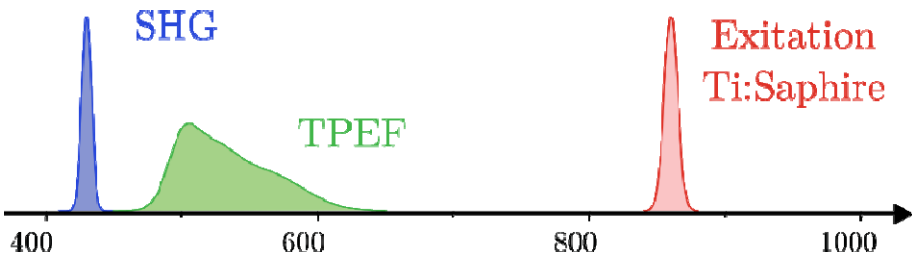

Figure 1.8: Excitation (Ti-Sapphire laser) and emission spectra in MP imaging microscopy. Adapted from (Olivier, 2009).

Figure 1.9 depicts the optical setup of a typical MP microscope. This combines an ultrafast laser system, a beam scanner unit and a microscope. A detailed description of the MP microscope used in this Thesis can be found in Chapter 2.

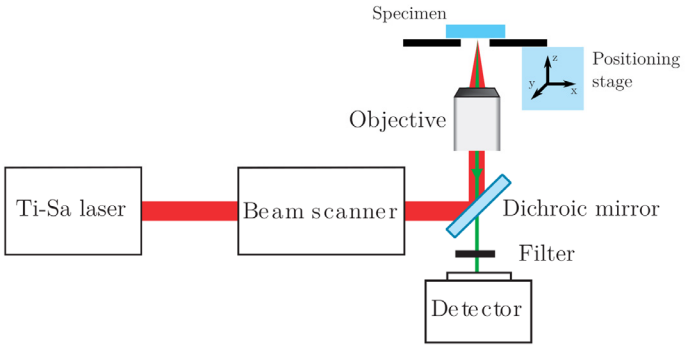

Figure 1.9: Schematic diagram of a MP microscope. Adapted from (Olivier, 2009).

Both, TPEF and SHG microscopy techniques are being used in biomedicine and related fields to image different types of cells, tissues and organs: muscles, lung, brain, intestine, skull bone, fish larvae and mouse embryos, among others. MP imaging of ocular tissues (mainly cornea and retina) have also taken some importance in the last years (Aptel *et al.*, 2010; Olivier *et al.*, 2010; Bueno *et al.*, 2011a; 2011b; Huss, 2012).

1.2. Femtosecond lasers and pulse compression

1.2.1. Concept of femtosecond laser

The use of fs-lasers (ultrafast or mode-locked) as illumination source is the basis for MP microscopy. The most extended has been the Ti-Sapphire laser system. A typical Ti-Sapphire source provides light pulses of about 120 fs (or less) and bandwidths of 30 nm (or less). Ti-Sapphire crystals are usually pumped by a frequency-doubled solid-state laser (Eichler & Eichler, 2010). This pumping source mainly consists of a laser source (incorporating an array of 808-nm diodes of 20 mW) focused into an optical fiber. This optical fiber leads the light to the laser head composed of two crystals into a resonator, a Nd:YAG and a SHG crystal. The former produces light of 1064 nm. The latter is used to frequency-double the signal to 532 nm.

The second component of the fs-laser usually consists of a broadband Ti-Sapphire crystal used as laser medium (see the rest of components in Figure 1.10).

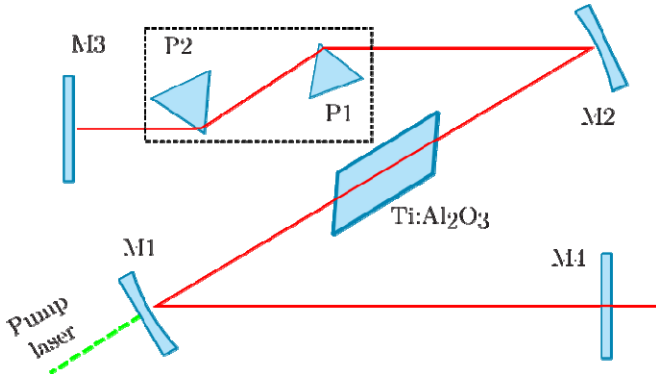

Figure 1.10: Elements of the cavity setup of a Ti-Sapphire laser. P1 and P2, prims; M1-M4, high reflecting mirrors. The prims are used to compensate chromatic dispersion (see below). M1 and M2 act as folding mirrors. The distance between M3 and M4 defines the repetition rate of the fs-laser, that is, the number of pulses emitted per second.

The concept of mode-locking or repetition rate (i.e. light pulse generation) is briefly explained in the following. The frequency spectrum of a pulse is described by a frequency comb, which consists of cavity waves (called longitudinal modes) with discrete frequencies, as shown in Figure 1.11.

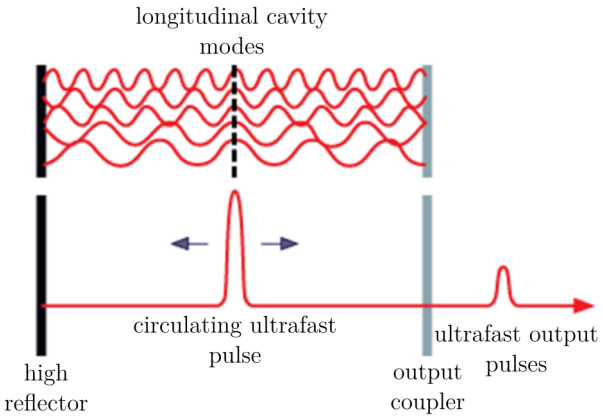

Figure 1.11: Principle of mode locking with five cavity modes. Only at one point the frequency components interfere constructively and produce a light pulse.

The superposition of these modes interferes destructively everywhere within the cavity except at one point, where a constructive interference is produced. This leads to the generation of a pulse. To get ultrashort pulses the number of interacting modes has to be very high: 10^6 modes to produce 10-fs laser pulses.

Moreover, Figure 1.12 shows a simplified laser cavity that consists of a pair of mirrors separated by a distance L (and including a gain medium and other components). This laser cavity length determines the repetition rate of the ultrashort pulse (Träger, 2007). The distance between two consecutive pulses in a pulse train is 2L. The so called round trip time

T_{RT} is given by 2L/c, being c the speed of light. The repetition rate is defined as the inverse of the round trip time, that is $1/T_{RT}$ =c/2L. For a repetition rate of 100 MHz a round trip time of 10 ns is required. For a round trip time of 10 ns a cavity length of 1.5 m is needed.

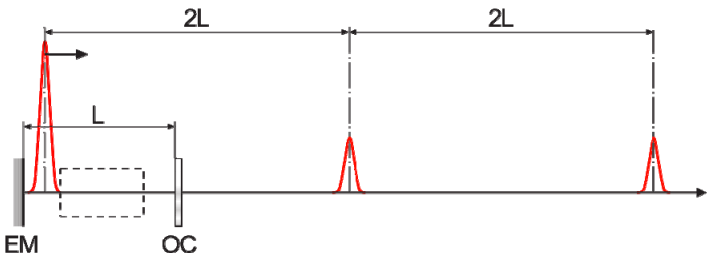

Figure 1.12: Schematic of a pulse train in a mode-locked laser cavity. Dashed box represents the gain medium and other laser components. EM and OC are the mirrors limiting the cavity length. This length determines the repetition rate of the laser system. Figure taken from (Träger, 2007).

In addition, let us assume a mode-locked laser with an average power of 500 mW. If the repetition rate is 100 MHz, the energy per pulse will be 5 nJ. If the pulse duration is 100 fs, it is easy to understand "how powerful" an ultrashort laser pulse is. These high repetition rates of ultrafast laser systems provide then high photon flux at a focal point, what is essential to produce MP effects in a material. In particular, the larger the amount of photons, the higher the probability of two-photon absorption. These conditions cannot be reached with a "regular" (continuous wave, or CW) laser. This is schematically shown in Figure 1.13.

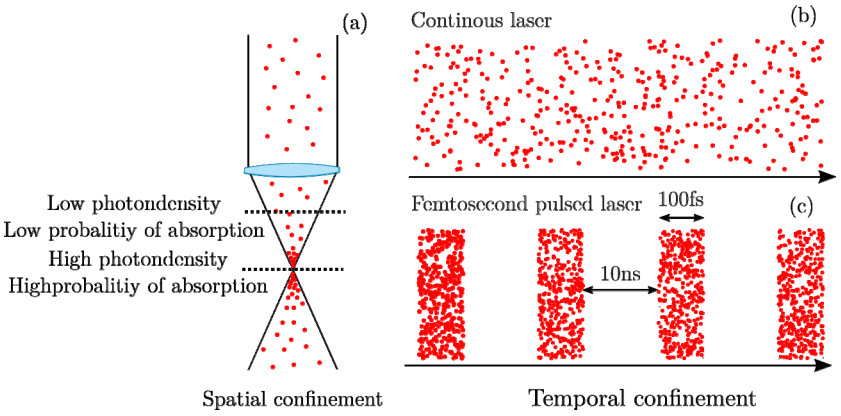

Figure 1.13: Comparison of a continuous and a mode-locked laser. Adapted from (Olivier, 2009).

1.2.2. Pulse duration measurement: Autocorrelation

The duration of a fs-pulse cannot be measured with conventional photoelectric devices. The only event that is short enough is the pulse itself, that is, the pulse itself has to be used to measure its own width. This is called autocorrelation. In this operation, the pulse is split into two pulses and a variable delay of one with respect to the other is introduced. Then, the pulses are recombined and focused into a non-linear element (usually a SHG crystal). The temporal overlap produces a non-linear signal (termed as autocorrelation function) that is related to the

pulse duration when a particular pulse shape (usually Gaussian) is assumed. The final signal reaches a photo-detector. Figure 1.14 shows the schematic of an autocorrelator.

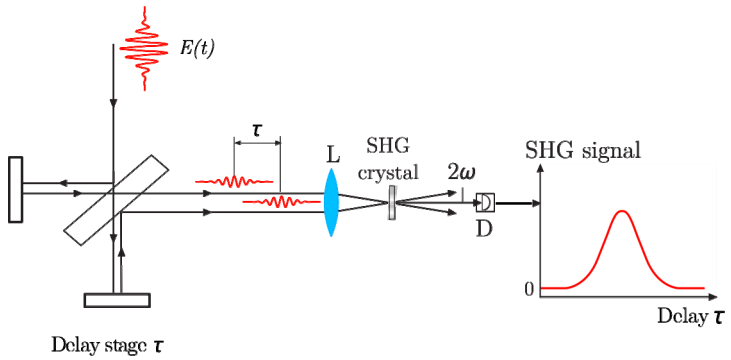

Figure 1.14: Schematic diagram of an autocorrelator. The incoming laser beam is split into two beams by a beam splitter. One of these beams is delayed with respect to the other one. A lens L is used to focus the two beams in a non-linear element. The signal is detected with a photo-detector. Figure adapted from (Träger, 2007).

However, autocorrelation only measures the pulse duration for an assumed pulse shape. They have no information about the actual shape of the pulse.

Frequency-resolved optical gating (FROG) is an interferometer-based spectrally-resolved autocorrelation technique (DeLong *et al.*, 1994; Trebino and Kane, 1993; Trebino *et al.*, 1997). It allows spectral resolved measurements, providing a two-dimensional data set in the time-frequency domain to estimate the pulse shape. The amplitude and phase of the pulse can be reconstructed via iterative retrieval algorithms. Instead of a photodiode a spectrometer is used. A more complicated technique is the spectral phase interferometry for direct electric–field reconstruction (SPIDER) (Dorrer *et al.*, 1999; Gallmann *et al.*, 1999; Iaconis and Walmsley, 1998). This is an interferometric pulse characterization procedure in the frequency domain, based on spectral interferometry. Finally, a non-interferometric approach known as MP intrapulse interference phase scan (MIIPS) combines pulse measurement and dispersion compensation (Pastirk *et al.*, 2003; Xu *et al.*, 2006). This technique offers the possibility of selective excitation without laser tuning (Ogilvie *et al.*, 2006; Pastirk *et al.*, 2003; Schelhas *et al.*, 2006).

1.2.3. Pulse dispersion and pulse compression

The spectral bandwidth of a laser pulse is inversely related to the pulse duration (or pulse length). This means that the shorter the pulse the broader the spectrum. As an example, the bandwidth of a pulse of 100 fs with a wavelength of 800 nm is about 20 nm. These spectral components propagate with different speeds when travelling through the optical components of an experimental system. This is due to the wavelength dependence of the refractive index, known as optical dispersion (usually understood as “positive optical dispersion”). With dispersion, shorter frequency components of the pulse travel faster than longer components (i.e.

red components travel faster than blue), what leads to a spread of the pulse in time (see Figure 1.15).

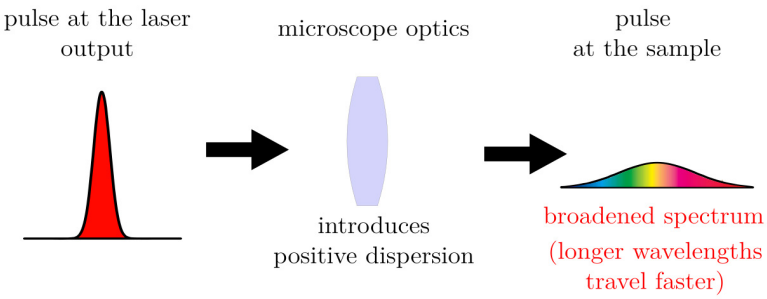

Figure 1.15: Broadening of a fs-pulse when passing a set of optical elements.

In general, this chromatic dispersion is explained by the spectral phase of the frequency components of fs-pulses, what represents the phase delay of each frequency component. The spectral phase dispersion, $\Phi_D(\omega)$, can be compensated by introducing the opposite amount of compensation dispersion, $\Phi_C(\omega)$. Only a zero spectral phase difference (all components have the same phase) leads to a transform-limited pulse with the shortest pulse duration (i.e. $\Phi_D(\omega)+\Phi_C(\omega)=0$).

Then, it is possible to minimize the dispersion effects by pre-compensating the broadening of the laser pulse. This can be achieved by introducing an "opposite dispersion" (understood as "negative dispersion") as indicated in Figure 1.16.

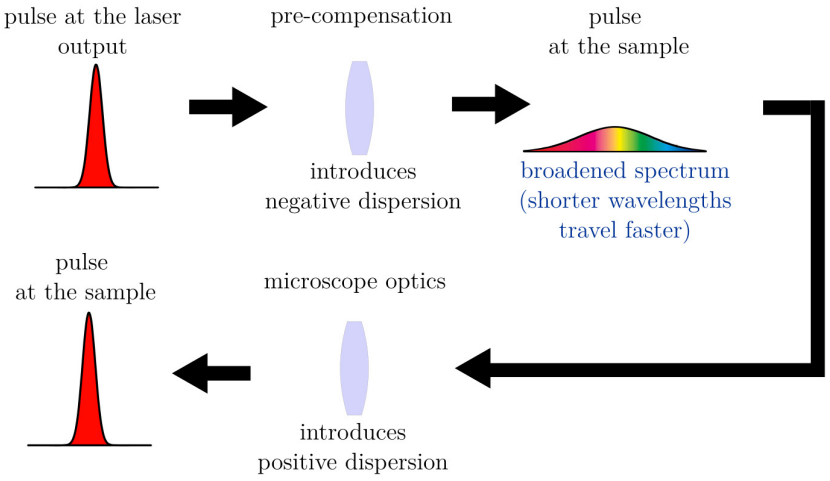

Figure 1.16: Pre-compensation of dispersion in a fs-pulse.

In a MP microscope, the fs-pulses of a Ti-Sapphire laser source are broadened in time before reaching the sample (and when passing a thick sample). This pulse broadening limits the effectiveness of MP microscopy, decreases intrinsic optical sectioning capabilities and reduces image quality. More laser power is then needed, what might produce unwanted side effects of photo-damage or photo-toxicity, of special importance when imaging biological samples. For

example, a 2-fold pulse broadening requires a 1.4-fold increase in the laser power (Fermann *et al.*, 2002; Zipfel *et al.*, 2003).

New methods of pulse compression or pulse shaping are now available to counteract pulse dispersion and thereby to improve penetration depth capabilities and enhance MP imaging. Some of these techniques are presented in the following.

The typical optical components involved in pulse compression operations are diffraction gratings, chirped mirrors and prisms (Figure 1.17). The main idea of these devices is to introduce negative dispersion to compensate for the positive dispersion induced by the microscope optics (lenses, objective, etc) (Fork *et al.*, 1984; Treacy, 1969).

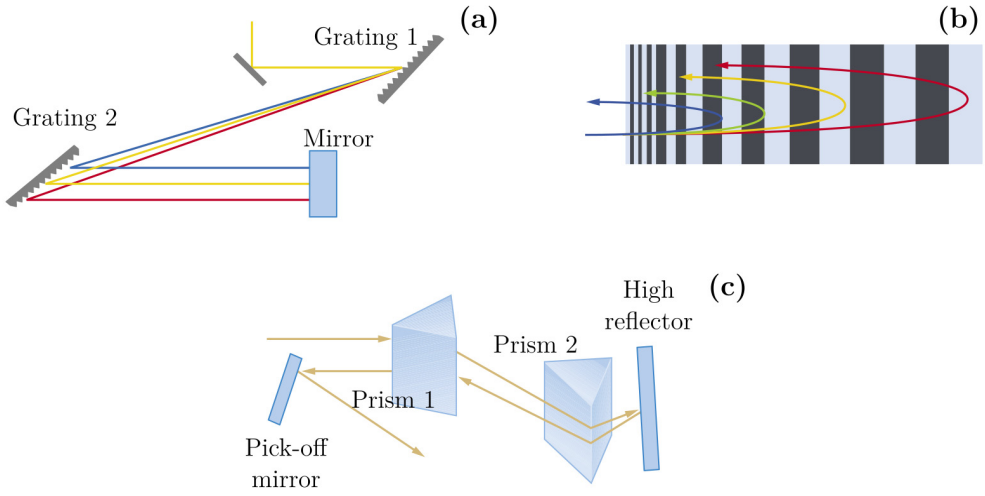

Figure 1.17: Pulse compressing techniques. (a) Gratings, (b) chirped mirrors, (c) prisms. Figure adapted from (David *et al.*, 2007).

The simplest ways for pulse compression are prisms (Fork *et al.*, 1984) and gratings (Treacy, 1969). In the former configuration, two prisms and a high reflecting mirror are often used (Figure 1.18). The first prism introduces a negative angular dispersion, and the second prism re-collimates the beam. The amount of dispersion introduced can be controlled by adjusting the distance between the prisms. A mirror is used to recombine the transversal chirped frequency components of the pulse. It re-directs the light beam once again through the two prisms. This mirror is slightly tilted to reflect the light with an offset in the vertical direction. Alternatively, a second prism pair can be used to recombine the pulse (this is called a four-prism pulse compressor).

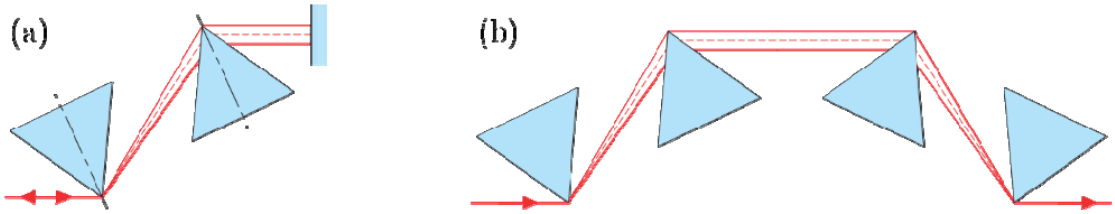

Figure 1.18: Pulse compressor with a two-prism (a) and a four-prism (b) configuration.

With a similar configuration a pair of gratings can also be used to create a pulse compressor (Figure 1.17(a)). Now the distance between the gratings determines the introduced negative dispersion. Compared to prisms, gratings have higher losses what is not much suitable for MP microscopy. However, since a grating glass is more dispersive than a prism, they need a relatively shorter compression length and then less physical space in the experimental optical table is required.

The third possibility for pulse compression is the use of chirped mirrors (Figure 1.17(b)). These consist of multilayer mirrors to provide wavelength-dependent penetration depth. Although chirped mirrors can accurately control dispersion, this is shorter than that corresponding to prims or gratings.

The pulse compressor techniques involving prisms, gratings or chirped mirrors are understood as static approaches. Pulse shaping techniques are also available for dynamic dispersion corrections. They use liquid-crystal or acousto-optic modulators and deformable mirrors (DM) to compensate for the required dispersion.

1.3. Aberrations and adaptive optics

1.3.1. Concept of wavefront aberration

The wavefront is defined as the surface of equal phase of the light beam. A collimated beam has associated a flat wavefront and a convergent beam a circular one. Any deviation of these ideal shapes is called wavefront aberration (WA). These distortions occur when the light beam is reflected at a non-uniform surface or it passes through an inhomogeneous medium with different refractive indices (Figure 1.19).

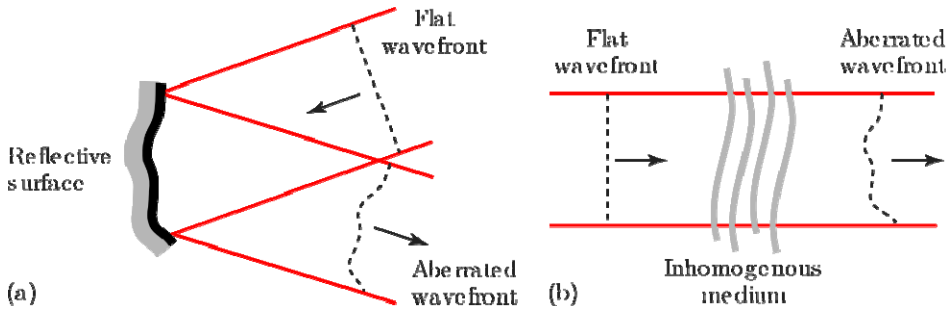

Figure 1.19: Concept of WA. Adapted from (Cristóbal *et al.*, 2011).

The WA can be mathematically described by means of a linear combination of orthogonal functions defined in a circular aperture (i.e. over the unit circle) known as Zernike polynomials, Z_n^m. These were introduced by Fritz Zernike in 1934. Since the individual terms can be associated with particular aberration terms, (astigmatism, defocus, coma,…), they are commonly used to describe the aberrations of an optical system.

Although different notations are used for the Zernike expansion, here we will adopt the double-index convention of the Optical Society of America, where the sub-index indicates the radial order and the super-index the frequency. With this notation the WA can be written as:

$$WA(\rho,\theta)=\sum_{n=0}^{\infty}\sum_{m=-n}^{n}c_n^m\cdot Z_n^m(\rho,\theta) \tag{1.1}$$

with (ρ,θ) being the radial coordinates and c_n^m the coefficients of the expansion series.

Figure 1.20 depicts several Zernike polynomial orders. It is interesting to notice that piston (Z_0^0) and tilts (Z_1^{+1} and Z_1^{-1}) do not compromise the image quality.

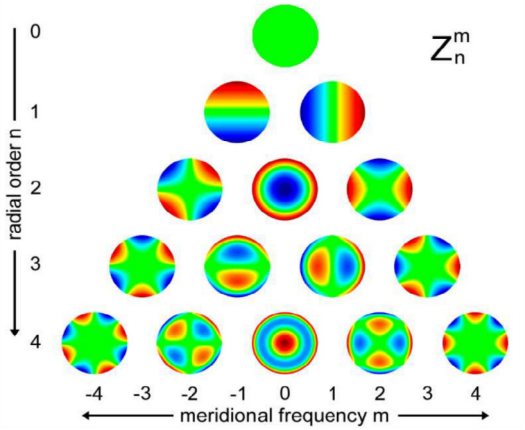

Figure 1.20: Zernike polynomials up to 4th order (the first 15 Zernike terms).

A common metric is the root-mean squared (RMS) wavefront error. This is defined as the standard deviation of the WA and can be described as:

$$RMS=\sqrt{\sum\left(c_n^m\right)^2} \tag{1.2}$$

The RMS will be zero for a perfect optical system (no aberrations present). For real systems, the higher the RMS value, the lower the quality.

1.3.2. Basics of adaptive optics

AO techniques are used to correct the WAs of a distorted light beam. They were originally used in Astronomy. Since the atmosphere is turbulent with time-varying changes in refractive index, optical images of astronomical objects viewed with ground-based telescopes are blurred.

An AO device is usually composed of two elements working in closed loop (Figure 1.21): a wavefront sensor to measure the WA and an adaptive element for corrections. The corrector is often a DM or a liquid-crystal spatial light modulator (SLM). The incoming distorted WA is measured by the sensor and, via a feedback-loop, the "opposite" wavefront is

generated by the corrector to cancel out (or minimize) the WA. The quality of the acquired image can then be restored (up to a diffraction limit, theoretically).

The most used wavefront sensor is the Hartmann-Shack (HS). This is composed of an array of microlenses and a CCD camera. The wavefront is sampled by the microlenses and the image of a set of spot is formed on the CCD. If the WA is null there is a regular distribution of spots. Otherwise, each spot moves from the ideal position. The difference between both locations is used to estimate the corresponding WA.

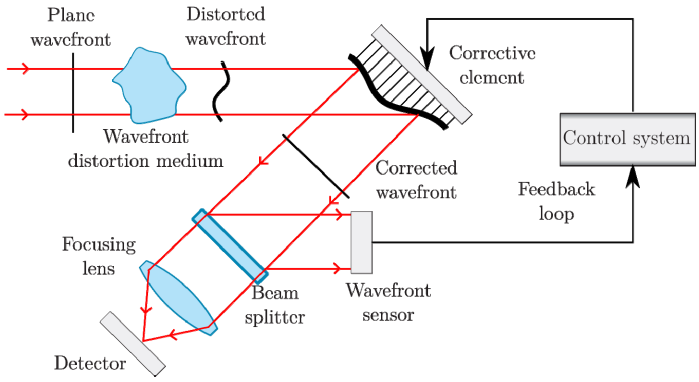

Figure 1.21: Schematic of a direct wavefront sensing AO device. Figure adapted from (Lubeigt *et al.*, 2010).

Once the WA is measured, its correction is based on the modification of the optical path length (L) of the light beam. Since L=n · d with n being the index of refraction and d the distance travelled by the light beam, the WA can be changed by varying any of both parameters. In particular, a SLM changes the former and a DM the latter one.

A DM is composed of moving reflective elements (moved through the so-called actuators) to locally modify the optical pathway. Figure 1.22 shows some of the DM setups available. The main advantages of DMs are their high optical efficiency, as well as their polarization and wavelength independence.

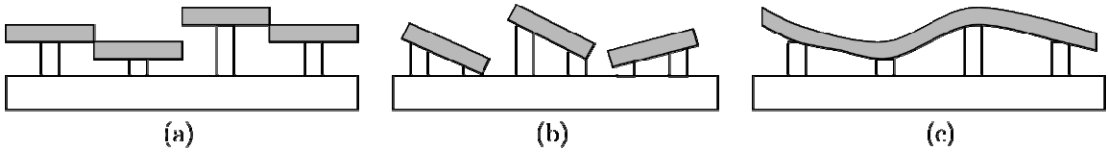

Figure 1.22: Several types of deformable mirrors: piston-like (a), piston-tilt-like (b) and continuous membrane (c). Adapted from (Cristóbal *et al.*, 2011).

A SLM is a refractive device (working in transmission or reflection) used to spatially modulate the amplitude and/or the phase of a light beam. Instead of actuators, it has “pixels”. Changes in the index of refraction of these pixels are used to locally modify the optical path length of the light travelling through it. These pixel-by-pixel changes depend on the voltage applied, which modify the orientation of the internal molecules of the liquid crystal (Figure 1.23).

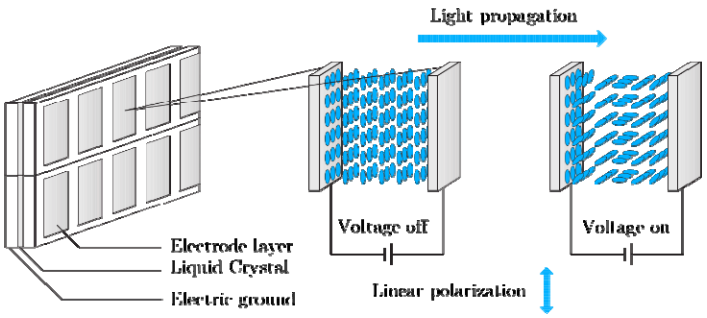

Figure 1.23: Liquid-crystal SLM. The applied voltage changes the index of refraction. Adapted from (Träger, 2007).

The main advantage of the SLMs is that they can generate very complex WA pattern due to large amount of pixels. The high absorption coefficient and the linearly polarized light required for an accurate behavior are the main drawbacks.

1.4. Adaptive optics in multiphoton microscopy

Over the last two decades MP microscopy has become a useful tool in biological and biomedical research, since the technique provides optical sectioning and 3D imaging in thick samples. However, the performance of MP microscopes is affected by aberrations introduced by the specimen (inhomogeneities), the laser beam, the optical components of the microscope (lenses, objective,…) and those due to the difference refractive index between the immersion medium and the sample under study. These lead to limitations, especially when focusing deep into the specimen, and compromise the quality of the images from those deeper layers.

Figure 1.24 shows this in a schematic way. If the optics is perfect, a plane wavefront turns into a spherical one and the laser beam is focused to a diffraction-limited laser spot (Figure 1.24(a)). However in the presence of aberrations (from the optics and specimen-induced) this wavefront is not spherical anymore and the focal spot increases in size, leading to the loss of signal, contrast and resolution (Figure 1.24(b)). If AO modifies the WA in an appropriate way, the focal spot can be restored (Figure 1.24(c)).

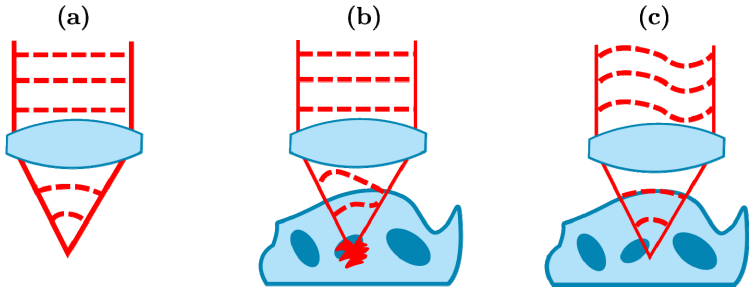

Figure 1.24: (a) Correction of aberrations in microscopy. (a) Ideal situation with no aberrations present. (b) Focal spot enlargement due to aberrations, (c) Compensation for aberrations using AO.

AO has been demonstrated in a range of microscope modalities, including wide-field, confocal and MP microscopy (Neil *et al.*, 2000; Marsh *et al.*, 2003; Kner *et al.*, 2010; Tao *et al.*, 2011; Gould *et al.*, 2012; Lenz *et al.*, 2014).

The correction of aberrations (mainly specimen-induced) in AO microscopes is carried out by means of two methods: direct and indirect wavefront sensing. In direct wavefront sensing a wavefront sensor is used to measure the plane-by-plane aberrations. The adaptive element (either a DM or a SLM) corrects for them in a controlled closed-loop.

However, direct wavefront sensing has always been challenging. Since biological tissues do not usually behave like point sources (or guide star, as known in Astronomy), the measurement of the WA within the sample is very difficult. This often requires the use of fluorescence beads, either natural or artificial (Tao *et al.*, 2013; Aviles-Espinosa *et al.*, 2011). Another method uses the coherence properties of the laser light and the properties of interference. This is called coherence-gated wavefront sensing (Rueckel et al., 2006).

To avoid the measurement of the specimen aberrations, an indirect wavefront sensing has been reported (Booth, 2004, 2007; Débarre *et al.*, 2009). This is a simpler technique that only needs a correcting device and the use of a wavefront sensor is avoided (Figure 1.25). With this procedure the acquired image is improved in a closed-loop operation (algorithm) through the optimization of a pre-defined image quality metric. This is known as a wavefront sensor-less (WFSL) procedure and it often uses a sequential modal correction of the different Zernike terms. Another indirect method is based on the so called pupil segmentation phasing method. This has successfully been used to correct aberrations at depth of 400 µm in brain tissue (Ji *et al.*, 2010).

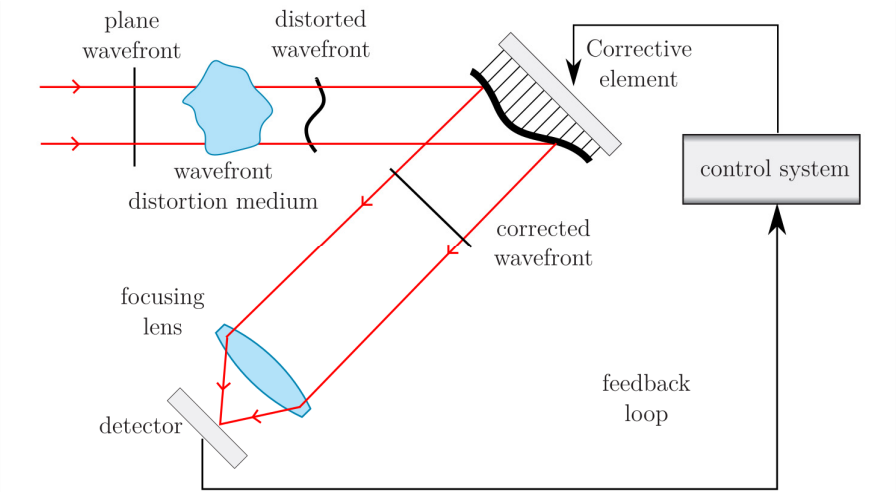

Figure 1.25: Indirect wavefront sensing. Adapted from (Lubeigt *et al.*, 2010).

Different algorithms for WFSL have been described: hill-climbing (Albert *et al.*, 2000; Marsh et al., 2003), genetic learn (Sherman *et al.*, 2002), random search (Wright *et al.*, 2005) or modal wavefront sensing (Neil *et al.*, 2000; Booth, 2002). Roughly speaking, these

optimization algorithms can be divided in deterministic and stochastic approaches. The simplest approach is to optimize Zernike polynomials in a deterministic manner Zernike term per Zernike term. It is simple, but is time-consuming.

Stochastic parallel gradient descent algorithms maximize (or minimize) the metric signal by using randomized perturbations of control parameters (Vorontsov *et al.*, 1997; Vorontsov *et al.*, 2000). It has been shown to be useful in MP microscopy of retinal tissues (Palczewska et al., 2010). Another approach is the called simulated annealing procedure. This is a generic probabilistic method for global optimization problems (Zommer *et al.*, 2006). Both algorithms were used and compared when improving retinal imaging for example. Another study also compared the performance of different WFSL methods: genetic, hill-climbing, random search and adaptive random search (Wright *et al.*, 2005).

1.5. A general description of ocular tissues

Microscopy techniques are oriented to the analysis of samples of interest in the different fields of research. In particular, ocular tissues are a paradigmatic example of specimens that might be of relevant importance in both scientific and clinical environments. Since some of these tissues will be used here, a brief description is presented.

The eye is a convergent optical system that focuses the light onto the retina by means of two lenses: the cornea and the crystalline lens. The lenses are the optical part of the ocular globe and the retina is the sensory receptor part. This is responsible for signal detection (Rhoades & Tanner, 2003) and the conversion of light into electrical impulses. The part of the retina in contact with the vitreous body is covered by nerve fiber bundles that transmit the electrical signal from the retina to the brain through the optic nerve head. In humans, the ocular globe has a diameter of about 24 mm. The connective white opaque tissue surrounding the eye is called sclera.

The cornea is a transparent connective tissue located at the front of the eye that allows light rays to pass into the interior of the eye (2/3 of the ocular refraction power are provided by the cornea). It consists of five layers: epithelium, Bowman's membrane, stroma (including keratocytes), Descemet's membrane and endothelium (see Figure 1.26). The 90% of the cornea is occupied by stroma, mainly composed of collagen. This corneal stoma provides a significant SHG signal. Ocular TPEF signals are obtained from the epithelium, the endothelium and the keratocytes. Detailed information of the MP images of the corneal structures can be found, for example, in (Bueno *et al.*, 2011a; 2011b).

The retina is a multilayered tissue with a total thickness of 200-400 µm. It is a light sensitive tissue, with different sets of cellular layers that extends from the photoreceptors (outer retina) to the ganglion cell layer (inner retina). Figure 1.27 shows the different layers of the human retina. The retinal pigment epithelium (or RPE) is a pigmented layer connected to

the outer segments of the photoreceptors. The layer between the sclera and the retina is known as choroid. This contains the vascular layer of the eye and provides oxygen and nutrients to the retina.

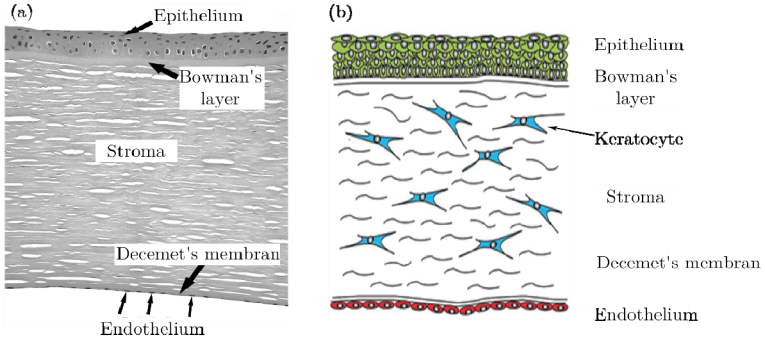

Figure 1.26: Histological microscope image of a cornea. Adapted from (Meeney & Mudhar, 2013). (b) Schematic cross-section of the human cornea. Keratocytes (or corneal fibroblasts) are specialized cells located within the stroma. Adapted from (Secker & Daniels, 2009).

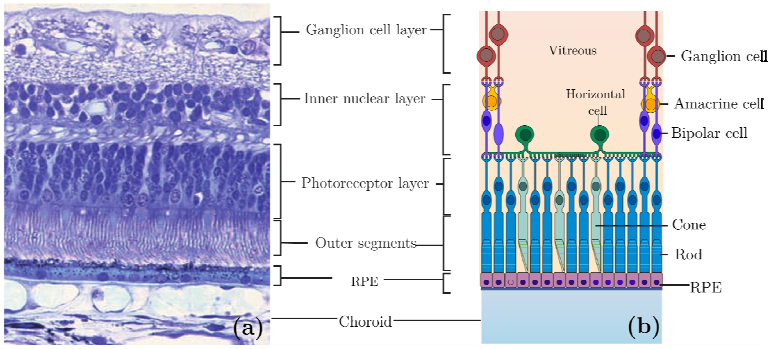

Figure 1.27: Retinal layers in a human retina. (a) Real histological section adapted from (Wright *et al.*, 2010). (b) Schematic of the retina adapted from (Zhang *et al.*, 2012).

1.6. Motivation, aim and outline of this work

MP microscopy is a powerful tool in biomedical imaging that combines advanced optical techniques of laser scanning microscopy with long-wavelength non-linear excitation. The technique provides non-invasively marker-free images with sub-micron resolution. It is intrinsically confocal what allows three-dimensional resolved microscopy imaging of both static and, more recently, dynamical structures.

However, imaging deeper layers within the tissue is limited by some factors that have not completely over-passed at the moment. Although AO procedures and pulse shaping techniques have been shown to improve MP images the techniques need to be optimized and improved, especially when applied to biological specimens, where effects of photo-damage and photo-toxicity are critical.

Furthermore, the use of MP microscopy in the visualization of ocular structures is a topic of interest for both basic research and clinical environment. The different ocular tissues

provide TPEF and/or SHG signal. Then, MP microscopy has big potential for ophthalmologic applications, since it might provide information not available with other techniques such as confocal microscopy or regular ophthalmoscopes. Since ocular pathologies modify the morphology of the different ocular structures, an optimized visualization would be of interest for early diagnosis and follow-up procedures.

In that sense, this works concentrates on improving MP microscopy imaging by spatial and temporal manipulations of the illumination laser beam through aberration correction and pulse compression respectively. Special attention has been paid to the enhancement of MP images of ocular tissues. The main objectives of this Doctoral Thesis are the following:

- Controlled manipulation of the WA of the laser beam to get improved plane-by-plane MP images of thick tissues.
- Analysis of the effects of different parameters on the WA correction: depth location of the plane, size of the imaged area and sequence of the Zernike mode correction.
- Study of the effect of the spherical aberration (SA) as a function of the specimen's depth.
- Determination of a global SA value that allows the MP imaging optimization of entire samples (avoid individual layer corrections).
- Pre-compensation of the laser pulse temporal length to improve MP imaging.
- Evaluation of the required laser power reduction to minimize damage in biological samples while using a pulse compression operation.

The outline of this thesis is briefly described in the following.

Chapter 1 serves as introduction and gives an overview of the microscopy techniques and an introduction to MP microscopes. The concepts of fs-lasers and pulse compression are also reviewed. Basic ideas on WAs and AO are also explained, including a section centred on AO in microscopy.

Chapter 2 describes the custom-made MP microscope used in this thesis.

Chapter 3 deals with a WFSL AO technique based on a hill-climbing algorithm to enhance the quality of images acquired with the described MP microscope. A liquid-crystal SLM was used as an adaptive element to systematically generate Zernike modes during image recording.

Chapter 4 is dedicated to investigate the effects of SA in MP microscopy imaging. Instead of a SLM, the combination of a HS and a DM was implemented into the microscope. This AO device was used to generate different SA values while fast tomography MP imaging. These controlled amounts of SA were used for extending depth-of-focus (DOF) when imaging deeper locations within the samples.

Chapter 5 is centered on maximizing the effectiveness of MP processes with pulse compression effects. The effects of pulse broadening due to the microscope optics are pre-compensated by means of a two-prism pulse compressor device. Fast tomographic imaging is also used to show the optimization of MP images in thick tissues.

Chapter 6 finally presents the conclusions and summarizes the main contributions of this research.

CHAPTER 2

Customized multiphoton microscope

This chapter describes the custom-made MP microscope. This combines an inverted microscope with a fs-laser, a scanning unit, a Z-control motor and a photon counting detection unit. Both TPEF and SHG signals were collected in the backscattered direction through a non-immersion objective.

2.1. Experimental setup

A schematic diagram of the MP microscope is presented in Figure 2.1, and a general view of the actual setup is shown in Figure 2.2. The main components are described in detail in the following sections.

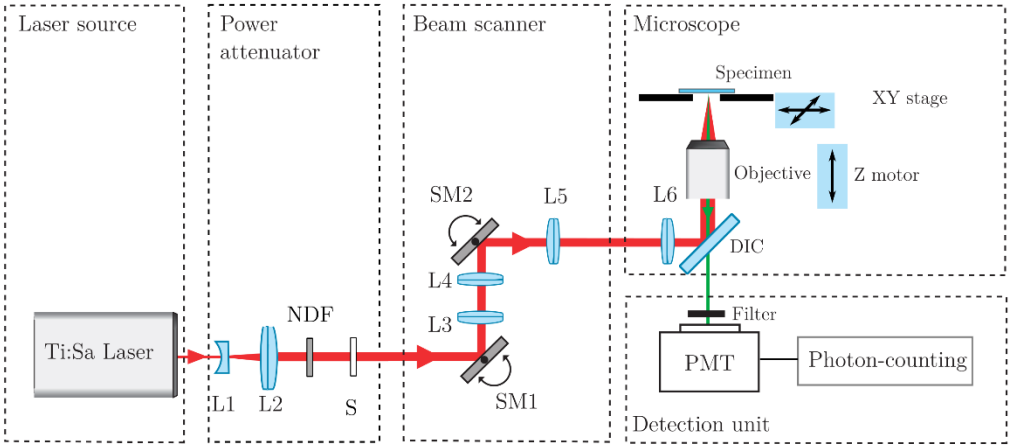

Figure 2.1: Schematic setup of the MP microscope used in this Thesis. L1-L6, lenses; NDF, neutral density filter; S, shutter; SM1 and SM2, scanning mirrors; DIC, dichroic mirror; PMT, photomultiplier tube.

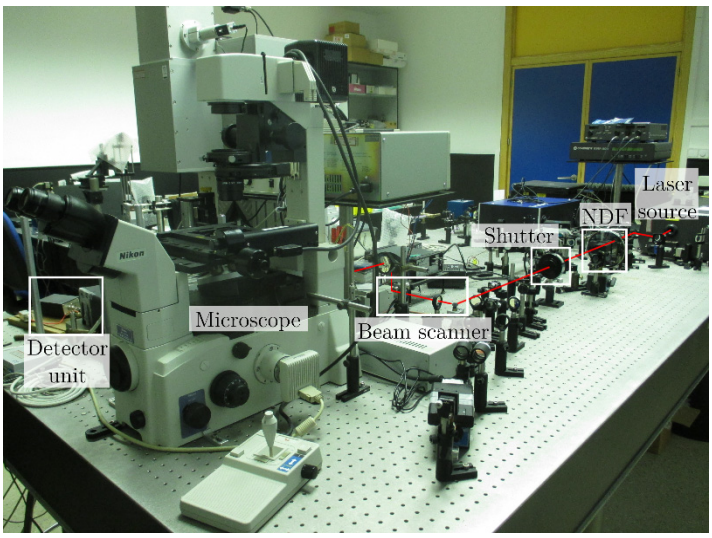

Figure 2.2: Picture of the MP microscope. See text for details.

2.1.1. Laser source

The laser is a tunable mode-locked Ti-Sapphire laser (Mira 900, Coherent, St. Clara, CA, USA) pumped by a Nd-YAG solid state laser (Verdi V6, Coherent, St. Clara, CA, USA) with a wavelength of 532 nm. Two 808-nm diode arrays included in the power supply are used to pump over the Verdi V6 laser head.

The Ti-Sapphire laser emits light pulses of approximately 120 fs (as stated by the manufacturer) at a repetition rate of 76 MHz. The average power is about 800 mW and the

peak power up to 130 kW. Although this is a tunable laser, a fixed wavelength of 760 nm is used. Figure 2.3 shows the components of the laser system.

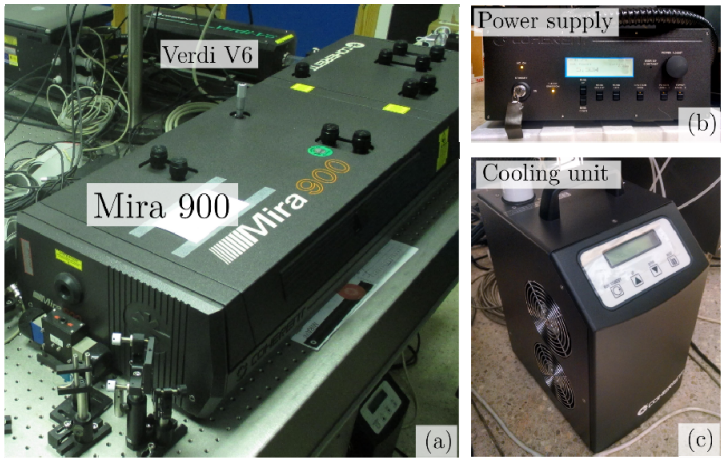

Figure 2.3: (a) Mira 900 and Verdi V6 laser systems. (b) Power supply including the diode arrays for Verdi V6 pumping. (c) Cooling unit required to cool down both laser systems.

Figure 2.4 shows the components of the Ti-Sapphire laser cavity. The continuous green laser beam from the Verdi V6 is focused with a lens L onto the Ti-Sapphire crystal which is situated between two concave mirrors M4 and M5.

The entire cavity of the laser ranges from the mirror serving as an output-coupler (OC) to the high-reflecting mirror HR6. The cavity length (L_C) is about 2 m, it is responsible for the round trip of each pulse and determines the repetition rate. Assuming that the pulse passes L_C twice at the speed of light in vacuum (c), the repetition rate can be calculated as $c/2L_C$=76 MHz.

The laser cavity can be divided into two arms. The first arm contains the optical path from HR4 to HR6. Due to the broad spectral bandwidth of the Ti-Sapphire crystal, intra-cavity dispersion is an issue in this type of lasers. Here a simple pulse compressor consisting of 2 prisms (P1 and P2) and a folding mirror (HR5) are introduced in this first arm to compensate for the possible intra-cavity pulse dispersion. The other arm (from OC to HR4), contains two other important optical components. A birefringent filter (BRF) located between HR1 and HR2 provides a tunable wavelength between 700 and 900 nm. Furthermore, a starter is needed to start up and maintain the self-mode-locking modes. The starter (see the element in front of HR2) introduces small fluctuations in the cavity length by means of a pair of fast rotating Brewster plates. The slit in front of OC is used to block the continuous component (i.e. the CW component) of the laser emission and let pass only the pulsed one (i.e. the mode-locked signal). Additional information on this laser system can be found in the user's manual of the Mira 900, although it is not necessary for the goal of this Thesis.

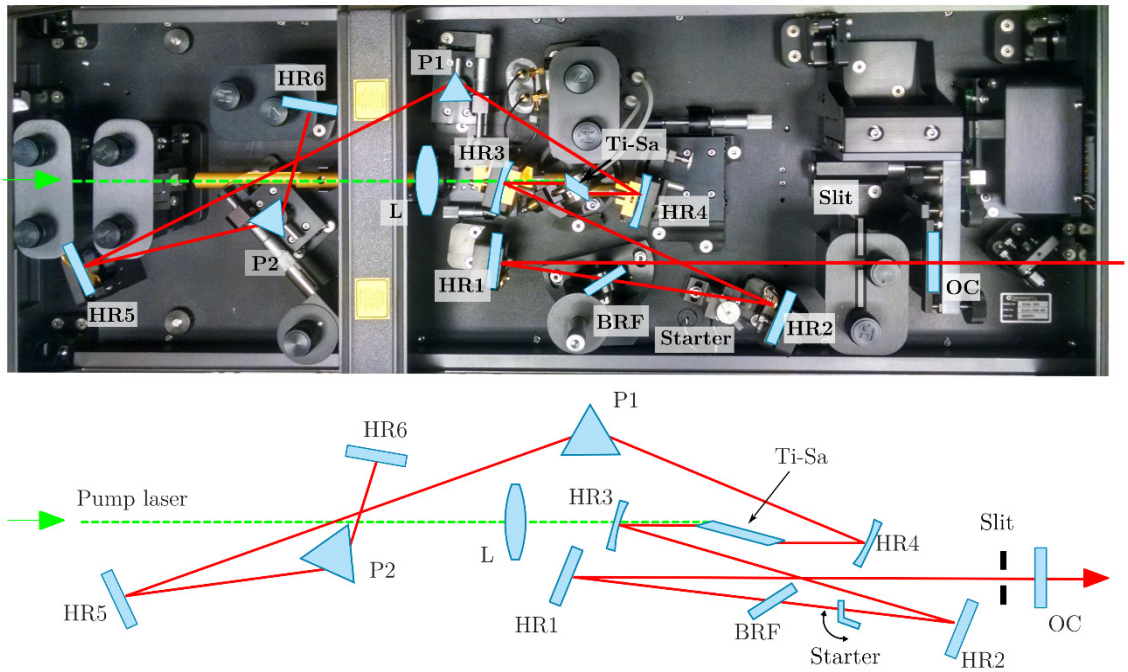

Figure 2.4: Picture and schematic of fs-laser cavity (Mira 900). OC, output coupler mirror, HR1-HR6, high reflecting mirrors; P1-P2, prisms; BRF, birefringent element; L, convergent lens; Ti-Sa, Ti-Sapphire crystal. Further details can be found in the text.

2.1.2. Illumination path

The beam firstly passes a pair of lenses, L1 and L2, set in a Galilean configuration and used as a 3x beam expander. L1 has negative power (f_{L1}=25 mm) and L2 positive (f_{L2}=75 mm). This Galilean configuration is preferred in high power laser systems to avoid air breakdown. A variable neutral density filter (NDF) controls the power of the beam reaching the sample. An electro-mechanical shutter (Uniblitz, Vincent Associate, Rochester, NY, USA) is used to block out the light when necessary.

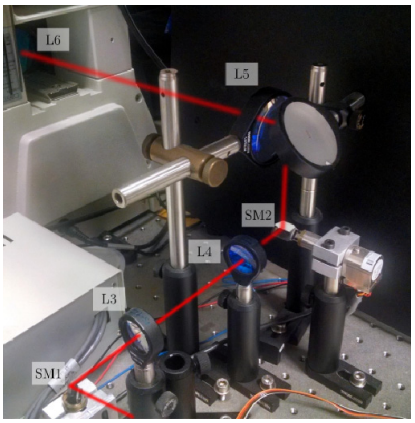

Figure 2.5: Elements of the scanning unit. SM1 and SM2, scanning mirrors; L3-L5, lenses.

The collimated laser beam passes through a pair of non-resonant galvanometric mirrors, SM1 and SM2 (GSI, VM1000, Billerica, MA, USA) coupled by a telescopic system of two

lenses, L3 and L4 (f_{L3}= f_{L4}=50 mm) (Figure 2.5). SM1 and SM2 are optically conjugated with the entrance pupil of microscope objective (through lenses L5 and L6, f_{L5}=f_{L6}=150 mm) and produce an XY scanning movement over the sample to be imaged. The speed of this scanning unit can be controlled directly with the control software.

2.1.3. Inverted microscope

A modified commercially available inverted microscope (Nikon TE2000-U, Tokyo, Japan) was used as imaging platform. A picture of the instrument is shown in Figure 2.6.

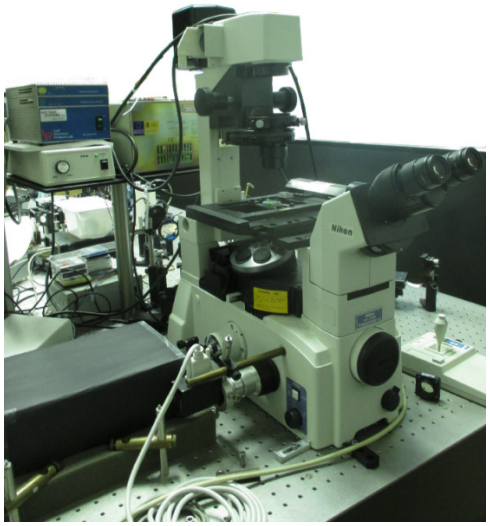

Figure 2.6: Picture of the inverted microscope used in this work.

The beam from the scanning unit enters the microscope, it is reflected in a dichroic mirror (DIC), passes an air long-working distance microscope objective (Nikon ELDW Series) and is focused on the sample under study. The microscope objective used was a 20x/0.5 NA. Figure 2.7 shows the lateral view of the microscope with the light pathway superimposed on it.

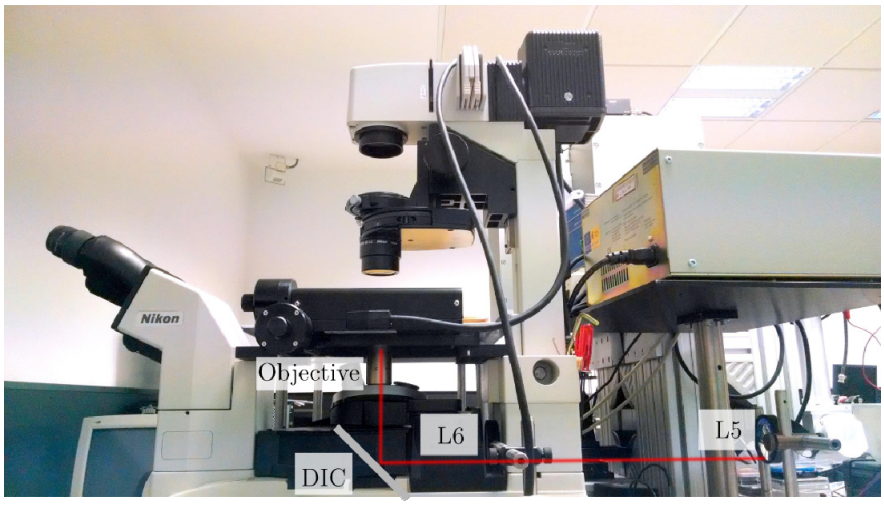

Figure 2.7: Inverted microscope and incoming light pathway. L5 and L6, lenses; DIC, dichroic mirror.

The sample is mounted on a XY stage (Biopoint2 Stage, Ludl Electronic Products, Hawthorne, NY, USA) for accurate positioning. Moreover, a Z-axis step motor (PI C-136, Karlsruhe, Germany) moves the microscope objective to focus the laser light into the required sample plane. The combination of the XY scanning and the Z-motor provides sets of XY images along the Z axis to get volume stacks (3D images).

2.1.4. Detection path

The focused light leads to non-linear effects in the sample, detected in the backscattered direction (Figure 2.8.). The emitted photons go back through the same microscope objective, pass the dichroic mirror and a spectral filter before reaching the detection unit. The filter placed in the detection channel allows the registration of either TPEF (broadband fluorescence filter, FGL 435, 435-700nm, Thorlabs Inc., Newton, NJ) or SHG (narrowband spectral filter FB380-10, 380nm±10nm, Thorlabs Inc., Newton, NJ) signals.

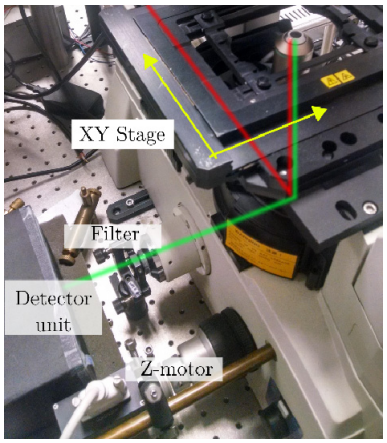

Figure 2.8: The red line represents the incoming laser beam and the green line shows the pathway of the non-linear signal in the detection channel. Yellow arrows indicate the movement of the XY stage. The Z-axis motor, the spectral filter and detection unit can also be seen.

The detection unit consists on a photomultiplier tube (PMT, R7205-01, Hamamatsu, Bridgewater, NJ, USA) with a high voltage power supply (C3830, Hamamatsu, Bridgewater, NJ, USA) and a photon-counting unit (C6465, Hamamatsu, Bridgewater, NJ, USA). The photons arriving at the PMT produce an electrical signal, in particular, each arrival is converted into a pulse of current. The photon-counting unit converts these pulses from the PMT into a signal equivalent to the collected photons. The value of the intensity for each scanned sample point and the position of the excitation laser beam are stored in a matrix. Figure 2.9 shows the different elements of the detection unit.

Figure 2.9: Elements of the detection unit: photon-counting unit (a), high voltage supply power (b) and PMT (c).

A data acquisition card (PCI-6259, National instruments, Austin, TX, USA) hosted by a standard desktop PC was used for data acquisition combined with a shielded I/O block (SCB-68, National Instruments Austin, TX, USA) to communicate with external hardware (scanning mirrors, XY stage and the photon-counting unit).

2.2. Procedure and imaging modalities

A custom LabView™ (National Instruments, Austin, TX, USA) software was used to control the MP microscope. This was written to provide different imaging modalities of the sample under study. Figure 2.10 shows the user's main interface.

Figure 2.10: Screen shot of the user's main interface.

The "regular" way of acquiring images in microscopy is scanning the sample in the XY direction, covering the area of interest (see Figure 2.11). These images are usually recorded using a raster scan with a fast X scan and a slow Y scan. If an XY image is done for different depths locations within the sample (controlled by using the Z-motor), 3D images of samples can be reconstructed.

Taking into account the optical properties of the microscope objective, four different XY image sizes can be recorded. The areas, named as S1, S2, S3 and S4 correspond to image

sizes of 90x90, 180x180, 270x270 and 360x360 µm^2. The number of pixels per image can also be chosen (usually 256x256 or 512x512).

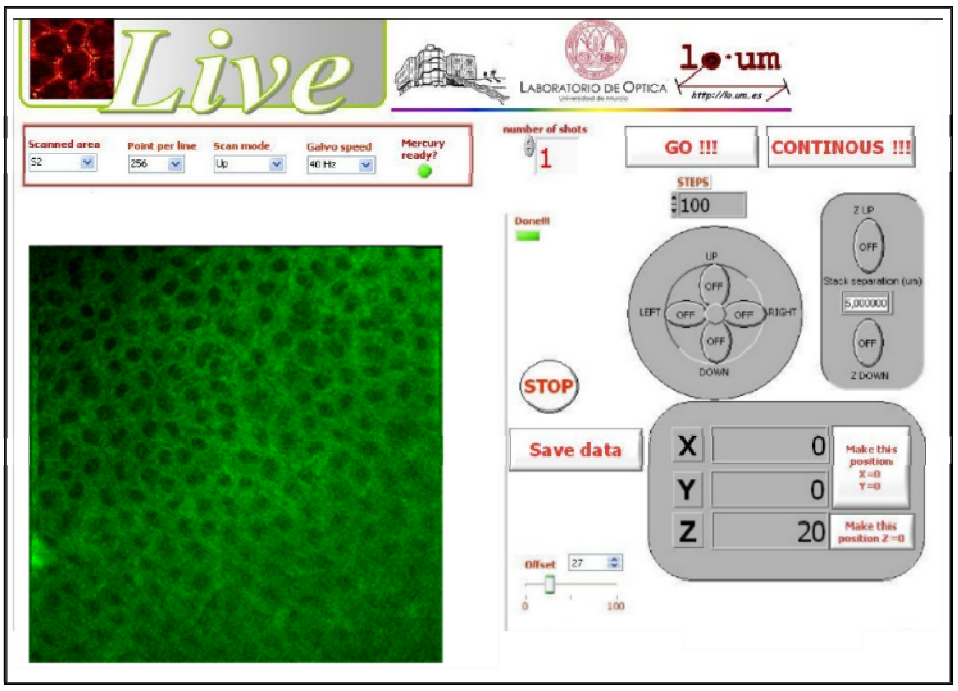

Figure 2.11: Example of a XY image as shown in the user's interface.

Another imaging modality is the XZ or YZ tomographic mode (similar to a B-scan used in optical coherent tomography instruments). This is a cross-sectional imaging where an X (Y) line is scanned along the Z direction of the sample to obtain images of the XZ (YZ) plane. Figure 2.12 shows an example of this imaging modality.

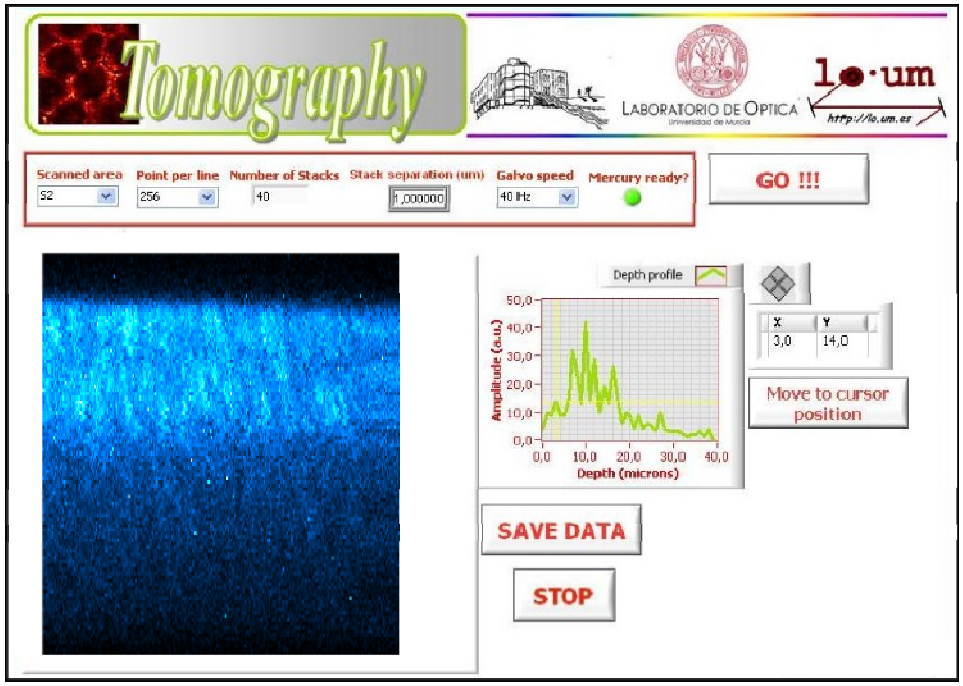

Figure 2.12: Example of a tomographic image as shown in the user's interface.

Both imaging modalities are schematically depicted in Figure 2.13.

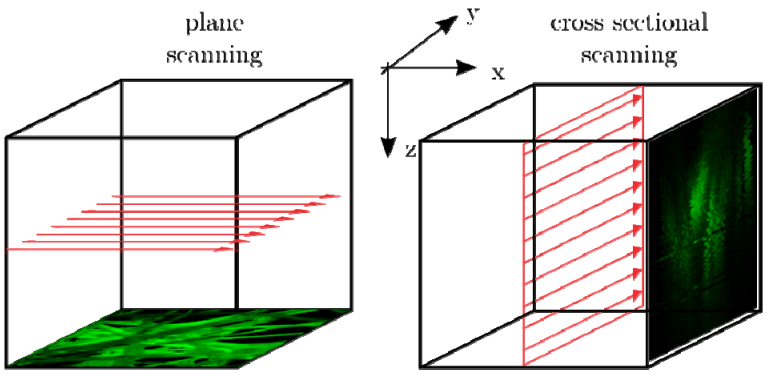

Figure 2.13: Imaging modalities used for the purpose of this work: Regular XY (a) and cross-sectional or tomographic (b).

2.3. Samples

Non-biological and biological samples are used in the experiments reported here (some of them are presented in Figure 2.14). The former includes pieces of cellulose and silk mesh stained with fluorescence marker (providing TPEF signal), and grains of starch (providing SHG signal). As biological specimens, both fresh (ex-vivo) and fixed non-stained ocular tissues were used. Fixed samples were flat-mounted on a microscope slide after overnight fixation with paraformaldehyde solution or embedded in paraffin wax (see Table 2.1 for details). Ex-vivo specimens (corneas) were placed up-side-down on a glass bottom dish (thickness: 170 µm) for imaging.

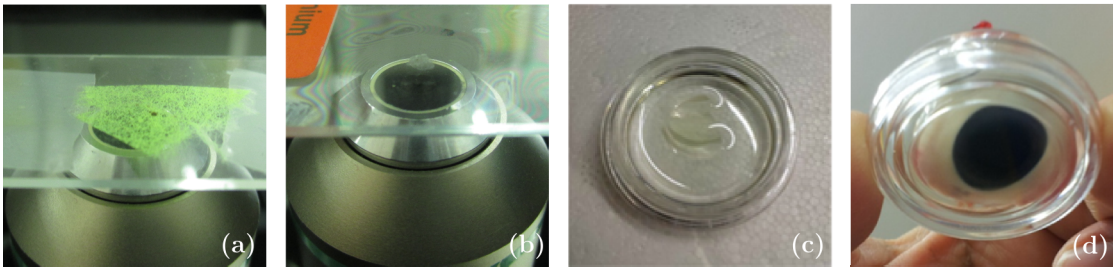

Figure 2.14: Examples of samples used in this Thesis. (a) Cellulose; (b) human epiretinal membrane (ERM); (c) chicken cornea and (d) porcine ocular globe used for corneal imaging.

Tissue	***Ocular tissue***	***Signal***	***Fixation***
Cellulose	No	TPEF	No (stained)
Silk mesh	No	SHG	No (stained)
Starch	No	SHG	No
Rabbit cornea	Yes	SHG	Yes (paraffin wax)
Bovine cornea	Yes	SHG	Yes (paraffin wax)
Porcine cornea	Yes	SHG	No (ex-vivo)
Bovine sclera	Yes	SHG	Yes (paraffin wax)
Chicken cornea	Yes	SHG	No (ex-vivo)
Chicken retina	Yes	TPEF	No (ex-vivo)
Human ERM	Yes	TPEF	Yes (paraformaldehyde)
Rat retina	Yes	TPEF	Yes (paraformaldehyde)
Mouse retina	Yes	TPEF	Yes (paraformaldehyde)

Table 2.1: Overview of the samples used in this Thesis.

CHAPTER 3

Sensor-less adaptive optics multiphoton microscopy: influence of depth location, imaged area and Zernike mode sequence

This chapter deals with a WFSL AO technique based on a hill-climbing algorithm to enhance the quality of images acquired with the custom-made MP microscope described in Chapter 2 (although slightly modified). A liquid-crystal-on-silicon (LCoS) SLM was used as adaptive element to systematically generate Zernike modes during image recording. For all tested samples the procedure provided improved images independently of the type of non-linear signal. The optimum aberration pattern was stable with time and the amount of aberrations presented a linear dependence with depth. For a particular depth location within the sample, the pre-compensated wavefront was independent on the size of the imaged area. The combination of Zernike modes optimizing the image depended on the correction control sequence; however, the final images hardly differed. At deeper locations, a noticeable dominance of the SA was also found.

MP microscopy is an imaging modality that allows large penetration depths and intrinsic optical sectioning of thick samples (Denk *et al.*, 1990; Campagnola *et al.*, 2001). However, as the light propagates inside the specimen it passes through regions with different refractive indices before reaching the plane to be imaged. This induces aberrations that enlarge, both laterally and axially, the focal spot within the specimen and reduce the MP excitation efficiency, which leads to a reduction in the quality of the images (signal level, contrast and resolution) (Booth and Wilson, 2001; Sherman *et al.*, 2002).

AO has been used to correct for aberrations, restoring MP image quality (Albert *et al.*, 2000; Neil *et al.*, 2000; Booth and Wilson, 2001; Sherman *et al.*, 2002; Marsh *et al.*, 2003; Rueckel *et al.*, 2006; Leray and Mertz, 2006; Leray *et al.*, 2008; Débarre *et al.*, 2009; Fernández *et al.*, 2009; Bueno *et al.*, 2010; Cha *et al.*, 2010; Aviles-Espinosa *et al.*, 2011; Zhou *et al.*, 2011; Tao *et al.*, 2013). Conventional AO implementations consist of a wavefront sensor to measure aberrations and an adaptive element for correction. In MP microscopy, this combination has been reported to correct for the aberrations of the laser beam and the microscope optics (Bueno *et al.*, 2010), as well as those of the specimen (Rueckel *et al.*, 2006; Cha *et al.*, 2010). However the latter are not straightforward and require the use of guide-beacons (Aviles-Espinosa *et al.*, 2011; Tao *et al.*, 2013), what makes the procedure more complicated.

Due to this difficulty, the most extended scheme for AO-MP microscopy has been the so-called WFSL technique (Albert *et al.*, 2000; Neil *et al.*, 2000; Sherman *et al.*, 2002; Marsh *et al.*, 2003; Wright *et al.*, 2005; Débarre *et al.*, 2009; Zhou *et al.*, 2011). In WFSL approaches, the adaptive element pre-compensates for the unknown sample's aberration without measuring them. They use iterative algorithms such as genetic learning (Albert *et al.*, 2000; Sherman *et al.*, 2002; Wright *et al.*, 2005), hill-climbing/sequential (Neil *et al.*, 2000; Marsh *et al.*, 2003; Wright *et al.*, 2005; Débarre *et al.*, 2009), stochastic (Zhou *et al.*, 2011) or random search (Wright *et al.*, 2005; Tang *et al.*, 2012), to find the best image according to a predefined image quality metric.

DMs have been the main adaptive element used in MP microscopy. They are usually reconfigured to generate individual Zernike aberration modes, during MP imaging acquisition. Up to now, the use of SLMs in AO-MP microscopy devices has been less common (Neil *et al.*, 2000; Shao *et al.*, 2012), probably due to the fact that their reflectance is ~50% and they require incident linear polarized light. Although this low reflectance and polarization dependence might limit the imaging of deeper planes within the specimen, the use of LCoS devices has overcome these drawbacks. In particular, LCoS modulators have been reported to be suitable for MP imaging at deep locations within the mouse cortex (Ji *et al.*, 2010, 2012).

Different AO-MP experiments have reported image improvement in a number of biological samples providing TPEF (Marsh *et al.*, 2003; Leray and Mertz, 2006; Rueckel *et al.*, 2006; Leray *et al.*, 2008; Débarre *et al.*, 2009; Bueno *et al.*, 2010; Cha *et al.*, 2010; Ji *et al.*,

2010, 2012; Aviles-Espinosa *et al.*, 2011; Zhou *et al.*, 2011; Tao *et al.*, 2013) and SHG (Jesacher *et al.*, 2009; Olivier *et al.*, 2009). Those samples included brain, intestine, pulmonary, heart and arterial tissues, mouse and Drosphila embryos, and C. elegans samples, among others. Although SHG is another form of non-linear microscopy, AO image improvement in specimens providing SHG signals are scarce (Jesacher *et al.*, 2009; Bueno *et al.*, 2010, 2014).

WFSL procedures compute the "optimum" WA for each imaged plane within the sample. However, they do not take into account the variations of the aberrations across the visual field. In this sense the technique would be appropriate if aberrations are approximately constant across a microscope's field of view. This occurs when the imaged field is small, but not for larger imaged areas where aberrations can significantly vary across the image (Schwertner *et al.*, 2004; Hovhannisyan *et al.*, 2008; Simmonds and Booth, 2013; Zheng *et al.*, 2013).

Moreover, WFSL algorithms often use Zernike polynomials to express the WA. The individual Zernike modes are generated by the active element, starting with lower order modes and sequentially increasing the aberration order. However, since Zernike polynomials are orthogonal, different number or combinations of them could be used in the optimization procedure.

We extend here the WFSL concept for MP applications by means of an LCoS-SLM device used as adaptive element. Images corresponding to different depth locations of samples providing both TPEF and SHG signal are optimized by using a hill-climbing algorithm. The performance of the instrument for different experimental and operational conditions is evaluated. The relationship between the order of the Zernike mode sequence correction and the final WA map which optimizes the image is also investigated. Variations of the WA with depth and the influence of different Zernike modes are also analyzed. Furthermore, the temporal stability in the correction as well as the dependence between the imaged area size and the corresponding optimum WA is also studied.

3.1. Experimental setup

The customized MP microscope previously described was modified by including an LCoS-SLM in the incoming pathway (Figure 3.1). The collimated laser beam was spatially modulated by an LCoS-SLM (Pluto IR2, Holoeye, Berlin, Germany; see Figure 3.2) optically conjugated with the entrance pupil of the microscope objective. Since the SLM can only modulate phase under a certain polarization state, the beam was linearly polarized (through LP) along the active axis of the LCoS. Details on calibration and phase mask wrapping operation can be found elsewhere (Fernández *et al.*, 2009).

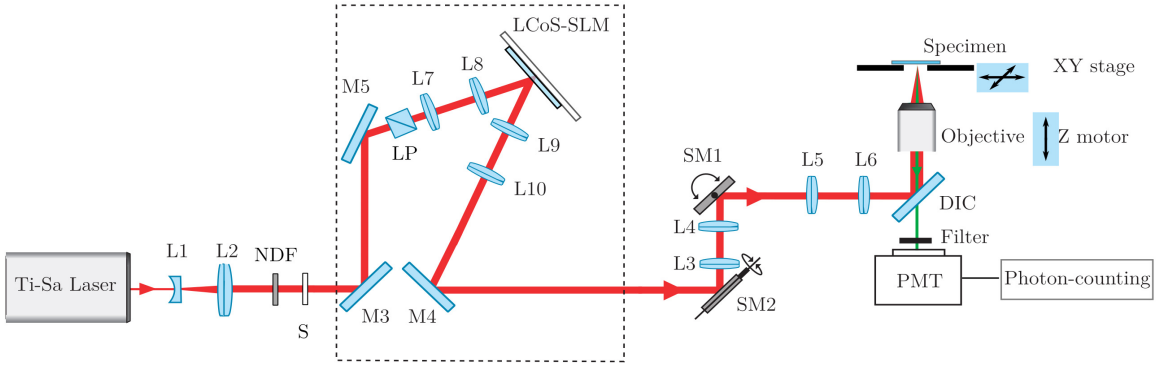

Figure 3.1: Schematic of the MP microscope incorporating the LCoS-SLM. L1-L10, lenses; NFD, neutral density filter; SM1-SM2, scanning mirrors; M3-M5, mirrors; LP, linear polarizer; DIC, dichroic mirror; PMT, photomultiplier tube.

The LCoS operates in reflection mode and it has a resolution of 1920x1080 pixels (8.0-µm pixel pitch) in a dimension of 15.36x8.64 mm^2. It was specifically designed to provide a phase shift above 2π for the wavelength used (i.e. optimized for infrared light). The display consists of twisted nematic crystals applied on a silicon chip. In the experiments the SLM is driven as an external monitor via a digital visual interface. The threshold damage of the LCoS device was 2 W/cm^2 (as indicated by the manufacturer for a continuous wave laser beam).

Figure 3.2: Picture of the LCoS-SLM.

The LCoS was used to produce pre-defined WAs with the adequate pupil size and position using MatLab™ (The MathWorks, Inc, Natick, MA, USA). WAs were presented as combinations of Zernike polynomials in a common phase wrapped mode (Figure 3.3). For a WA of 5-mm in diameter 307788 pixels were used.

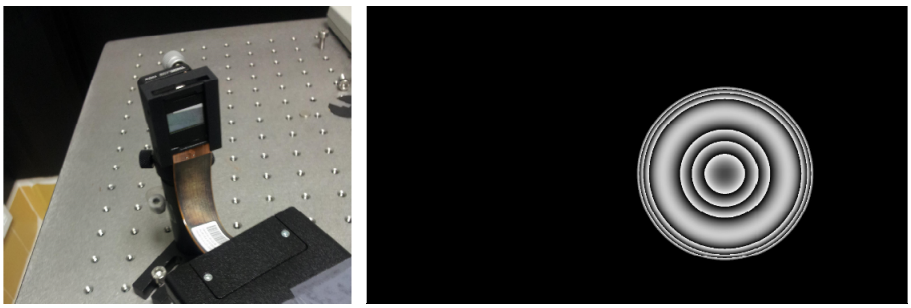

Figure 3.3: (a) LCoS-SLM as mounted in the experimental system. (b) Phase-wrapped WA projected on the LCoS-SLM.

3.2. Hill-climbing algorithm

The AO optimization procedure consisted of a WFSL technique based on a hill-climbing algorithm (Marsh *et al.*, 2003). This is an iterative searching technique looking for the WA map producing an image with the highest metric value. The WA was expressed as an expansion in Zernike polynomials. The individual Zernike modes are sequentially generated by the LCoS, ranging from 2nd (except defocus) to 4th order. The algorithm was run over 11 Zernike terms in total. The usual hill-climbing procedure corrects for Zernike modes in the "increasing-mode direction", that is, it starts with 2nd order terms and goes through 3rd and 4th order ones. However, for comparisons, the procedure was also performed in the "decreasing-mode direction"; i.e. starting with 4th order terms in reverse order. As stated in the Introduction, the Zernike modes are described using the Optical Society of America double-index convention (sub-index and super-index indicate the order and the frequency respectively).

For every Zernike term, its amplitude (both positive and negative) was changed in predefined steps until the recorded image provided the maximum metric value. An example of this is shown in Figure 3.4. Once this value was set, the procedure was repeated again for the next Zernike mode. If the Zernike mode control sequence was run in the increasing order, the final WA was estimated when the optimum amplitude of the term Z_4^4 was obtained. In the decreasing-order direction, the term Z_4^0 (SA term) was the first one (see section 3.3 for details on this).

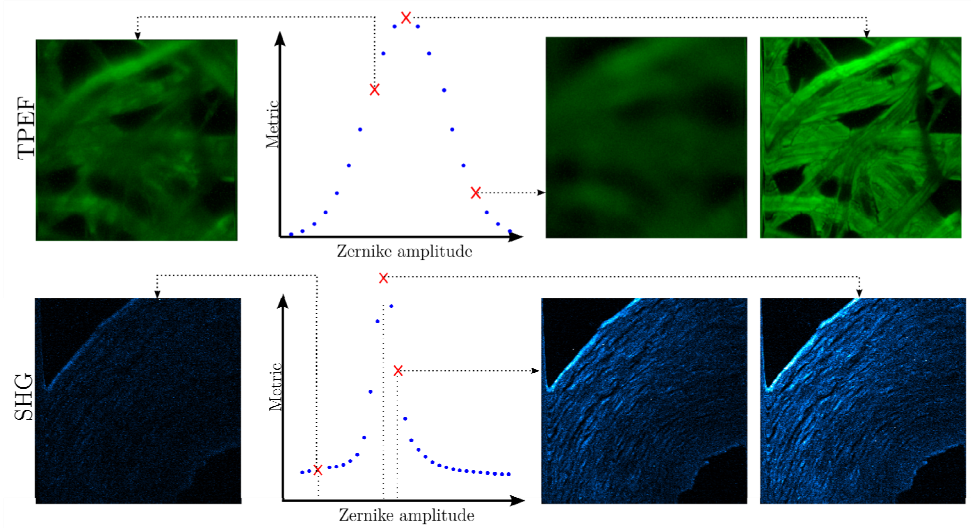

Figure 3.4: Illustrative example of image improvement (both TPEF and SHG signals) using the hill-climbing modal optimization algorithm for an individual Zernike term. Images correspond to the metric value and Zernike amplitude marked on red.

For a better understanding, a schematic diagram of the algorithm is depicted in Figure 3.5. Image acquisition, AO correction and image processing were done through custom software written in LabView™ and MatLab™. The total time for the entire procedure was about 3 min.

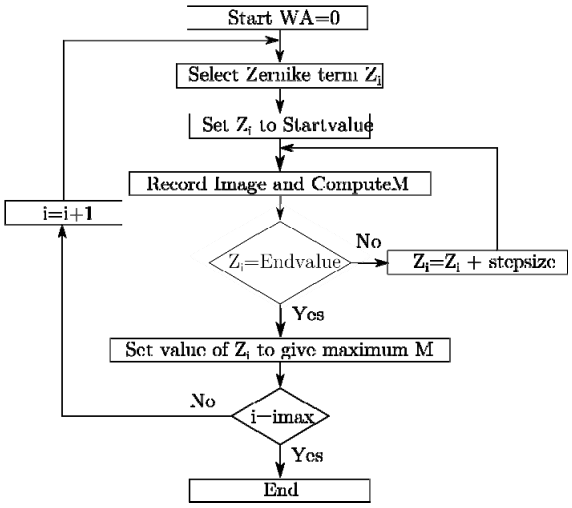

Figure 3.5: Flowchart of the algorithm used to optimize the images recorded with the WFSL procedure here described.

The chosen image quality metric to be maximized was the image sharpness (Muller and Buffington, 1974), defined as:

$$M = \iint I(x,y)^2 \, dx \cdot dy \tag{3.1}$$

This metric has been reported to take a maximum value only when the WA produced by the LCoS cancels out the combined WA of the optical system and the sample.

3.3. Image improvement of a single plane

In order to evaluate the robustness of the LCoS functioning and the performance of the proposed algorithm, this was firstly used to improve MP images of different samples at a single plane randomly chosen by the operator. Figure 3.6 shows an example of the step-by-step image improvement when using the hill-climbing algorithm for the different individual Zernike terms. It can be observed how the "optimum" amplitude is particular for each Zernike term.

Figure 3.7 displays TPEF and SHG images for four different samples before and after AO correction. The insets represent the pre-compensated WAs. The procedure improved all images independently of the nature of the non-linear signal. However, as expected, the WA producing the optimum image according to the chosen metric differed among images. For these particular samples the WA RMS values were respectively 1.13, 0.36, 0.22 and 0.17 µm. The increase in signal ranged between ~50 % and 2-fold depending on the sample.

Small features not present in original images appeared in the image when using AO. This means an increase in both contrast and resolution as shown in Figure 3.8. The corresponding RMS values of the WAs were respectively 1.05, 0.46 and 0.40 µm. The increase in signal was higher than 2-fold for these specimens.

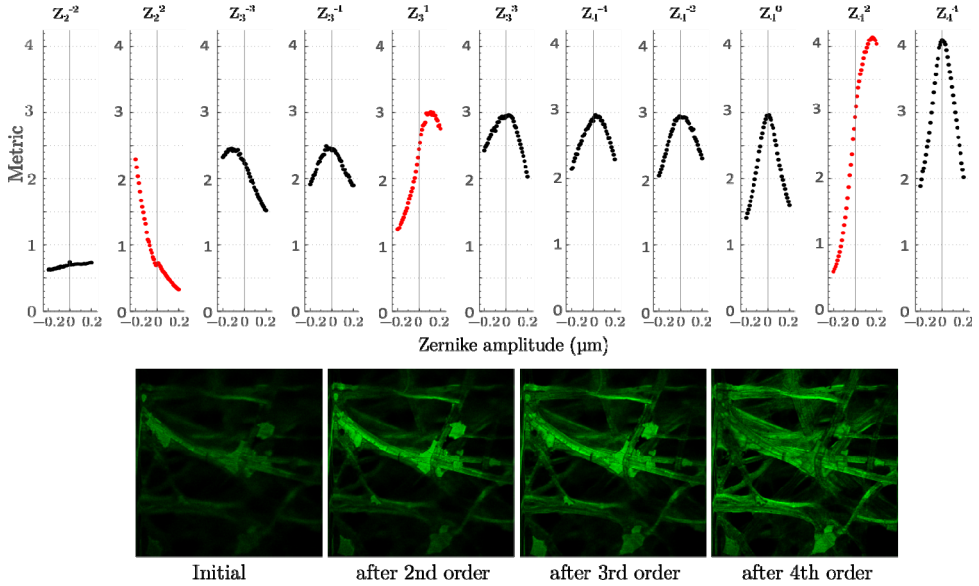

Figure 3.6: Example of image improvement using the hill-climbing algorithm described in this chapter. Top panels: Metric improvement for 11 Zernike terms. Red and black dots indicate those terms with and without influence respectively. Bottom panels: Image improvement for a piece of cellulose (depth location: 50 µm).

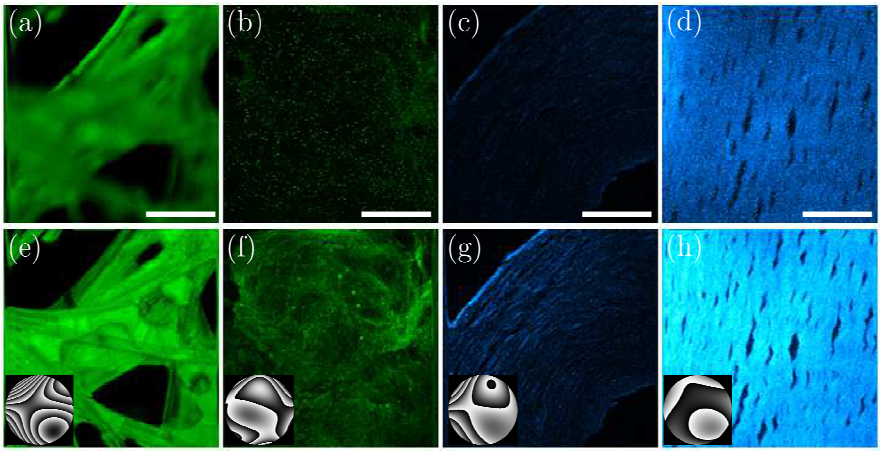

Figure 3.7: Image improvement for different specimens providing TPEF (a, b) and SHG (c,d) signals. Upper and lower panels correspond to images before and after WA correction respectively. (a, e) Cellulose, 40-µm depth; (b, f) non-stained human epiretinal membrane, 20-µm depth; (c, g) rabbit cornea, 20-µm depth; (d, h) bovine cornea, 15-µm depth. Insets at bottom row images are the WAs used for optimization. Scale bar: 50 µm.

As an additional example, the increase in contrast and resolution at a particular depth is shown in Figure 3.9 when visualizing "SHG natural beads" within a rabbit cornea. At 0 µm position, the beads are easily observed and the AO operation has no effect (i.e. the images before and after WA compensation are the same). However, these beads are hardly seen when imaging a plane at 50-µm depth. When the WFSL algorithm is used, the increase in image quality (and associated parameters) is noticeable (see differences in color bars of bottom images). It can also be observed that before using AO, a "large" and "defocused" spot appears at the top right side of the image acquired at 50-µm depth. When AO is in operation, this spot turns into "two beads" due to the increase in resolution.

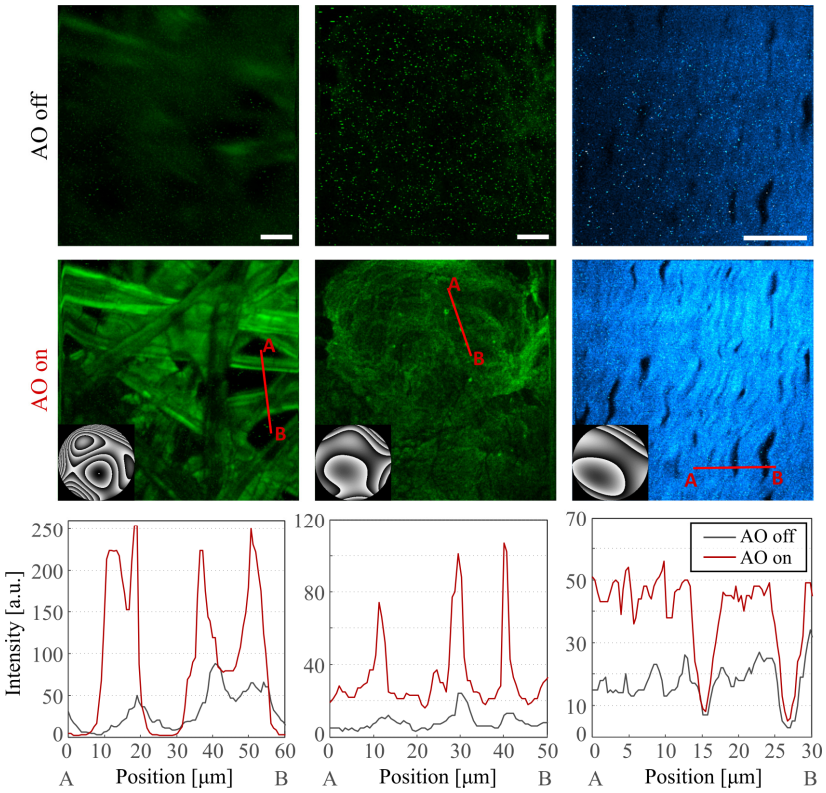

Figure 3.8: TPEF and SHG images recorded before and after WA correction. Samples correspond to a piece of cellulose (140-µm depth, left panels), a non-stained human ERM (50-µm depth, central panels) and a non-stained paraffin-embedded bovine cornea (40-µm depth, right panels). Intensity profiles (bottom plots) correspond to the red solid lines in the images. Insets are the WAs used for optimization. Bar length: 50 µm.

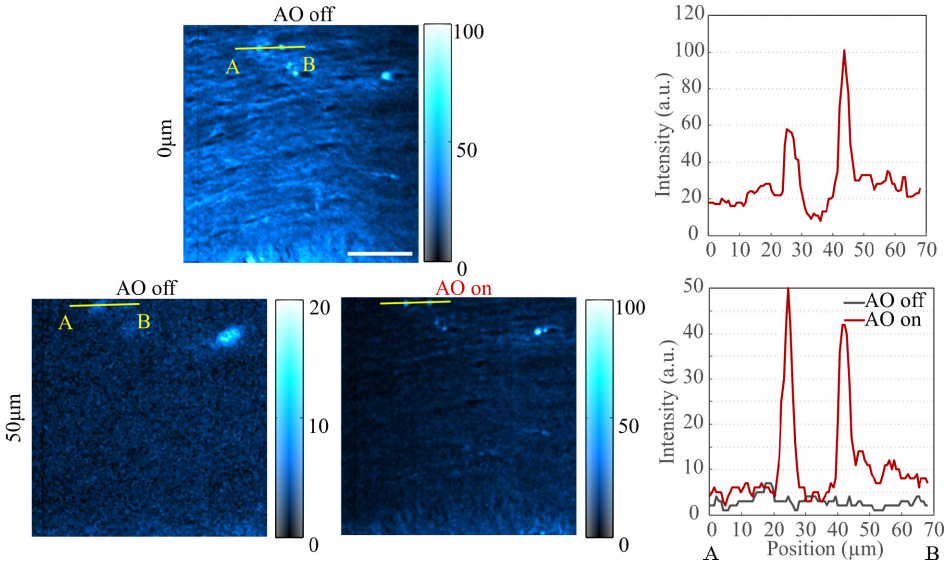

Figure 3.9: Example of AO-MPM images showing the increase in contrast and resolution. Plots represent the intensity profiles of yellow lines in left panels. The sample corresponds to a rabbit cornea. Bar length: 50 µm.

Although all the specimens here used are static samples, experimental conditions may vary due to uncontrolled changes (laser stability, thermal effects, photo-damage). The temporal stability of the procedure has been tested in two samples. Figure 3.10 shows pairs of images

before and after AO operation recorded some hours apart (24 and 8 hours for TPEF and SHG images respectively). Final improved images are similar and the corresponding WAs hardly changed with time. Differences between RMS values were smaller than 5% and the Zernike terms were similar (see plot at the bottom of Figure 3.10).

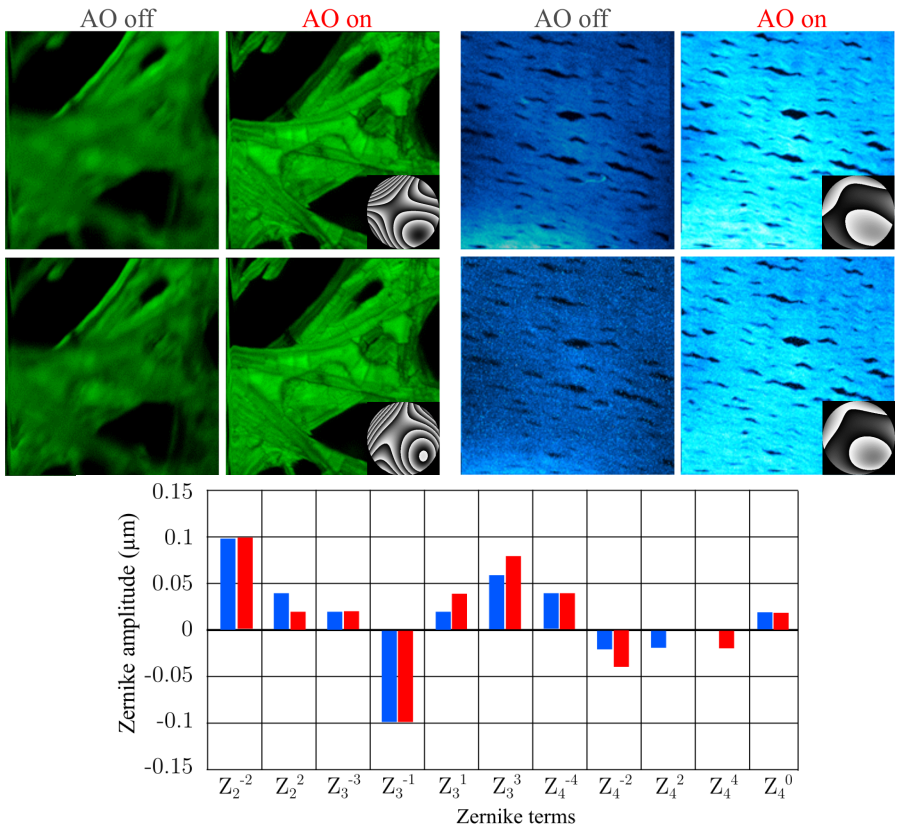

Figure 3.10: Temporal stability and robustness of the AO procedure here proposed. Images were recorded 24 (TPEF, left panels, cellulose) and 8 (SHG, right panels, bovine cornea) hours apart. Image size: 180x180 µm^2. Depth locations: 100 and 30 µm respectively. Right panel shows the corresponding 8-hour apart Zernike terms for the improvement of SHG images.

3.4. Image improvement as a function of depth

Although MP imaging provides inherent confocality, as already said, the effects of specimen-induced aberrations vary with depth location and limit 3D imaging performance. The reduction of signal and contrast depends on both the sample and the type of non-linear signal. An example of how the images are compromised due to aberrations is shown in Figure 3.11.

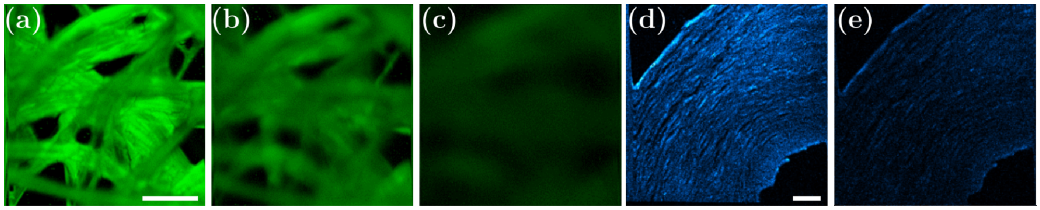

Figure 3.11: Effect of depth location on TPEF (a-c) and SHG (d, e) microscopy imaging. Depth locations were 0, 40 and 100 µm for TPEF images, and 5 and 15 µm for SHG images.

To improve the images at each depth location, the AO procedure was sequentially (plane-by-plane) applied. Figure 3.12 depicts TPEF images of a piece of cellulose acquired at different depth locations before (upper panels) and after WA correction (bottom panels), together with the WAs (insets). Since WA maps are presented in a wrapping mode, a qualitative comparison can be made. The improvement of images from deeper layers required larger amounts of aberration.

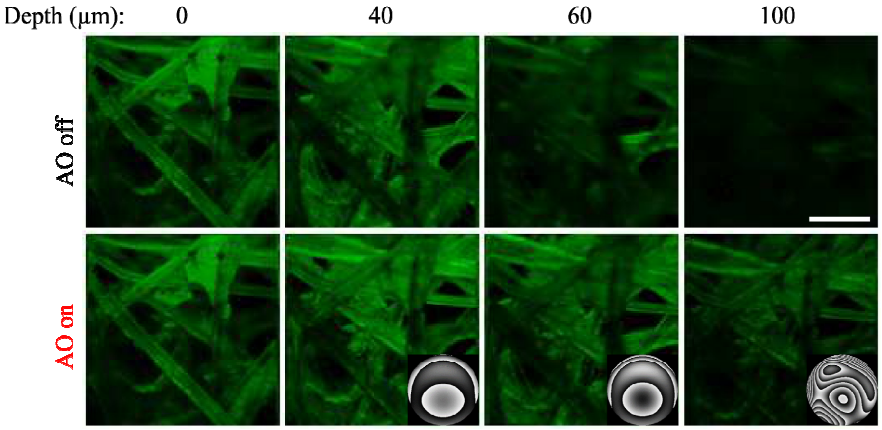

Figure 3.12: Benefit of using AO for TPEF images acquired at different depth locations within the sample (the signal decrease was 20% at 40 µm and 40% at 100 µm before WA correction). The insets are the corresponding WAs used for the image improvement of bottom row panels. Bar length: 50 µm.

The enhancement of TPEF images with depth is quantitatively showed in Figure 3.13. For a number of depth locations within the sample, Figure 3.13(a) presents the metric values without (blue symbols) and with (red symbols) AO correction. For shallow planes the improvement was hardly noticeable since the specimen-induced aberrations at those depth locations were small. However, this behavior clearly changed when going deeper into the sample and TPEF signal was clearly improved. The values of total RMS corresponding to the WA maps used are depicted in Figure 3.13(b) (blue symbols). As a comparison, the corresponding values of the optimum SA for each depth location are also presented (red symbols). A linear increase with depth was found for both total RMS and SA values.

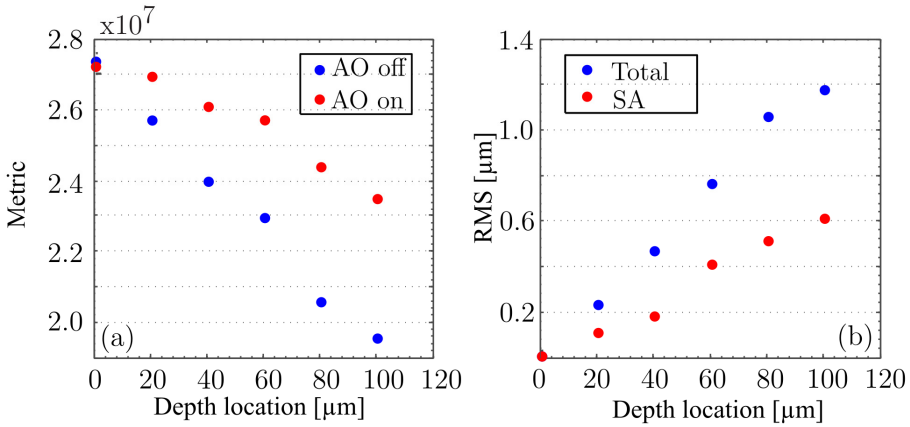

Figure 3.13: (a) Comparison of metric values as a function of depth before and after WA correction in sample of Figure 3.12. (b) Corresponding values of total RMS and SA itself.

The dominant Zernike modes are high order terms, basically Z_4^0 (SA), and to a less extent Z_3^{-1} (coma) and Z_3^3 (trefoil). All these terms increased in amplitude with depth. Although the values of aberrations are particular for each sample and depth location, a similar behavior was found in specimens providing SHG signal. However, for SHG images both the drop in signal and the increase in the amount of aberration are much more pronounced. This is shown in Figure 3.14 for the histological section of a rabbit cornea in paraffin wax. A visual inspection reveals how at 15 µm the structure is hardly seen before using AO.

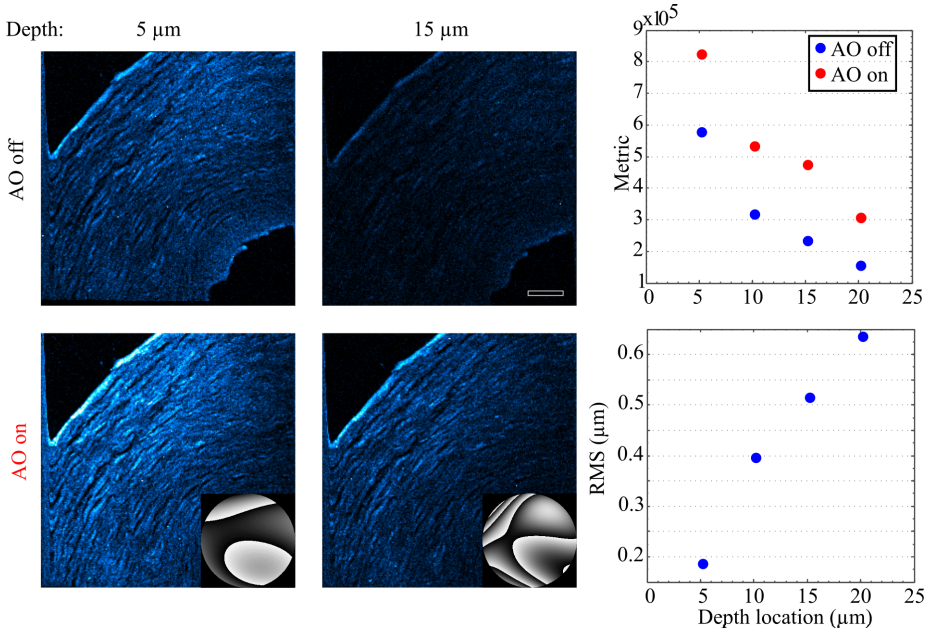

Figure 3.14: Improvement of SHG images (rabbit cornea) for different depth locations using the reported hill-climbing procedure. Values of the metric without and with AO in operation (upper plot) and the corresponding RMS values (bottom plot) are also shown. Bar length: 50 µm.

3.5. Influence of the imaged area

As spatial features within the sample might be very different across the imaged area, the WA able to optimize the image might depend on the visual field. Now the question would be: To what extent can a WA correction for a particular area be applied to a larger one? In the following, the dependence of the WA map with the size of the imaged area will be explored.

The modal hill-climbing algorithm was run for different imaged areas in a specific sample providing TPEF signal. The areas were S1, S2, S3 and S4, corresponding to image sizes of 90x90, 180x180, 270x270 and 360x360 μm^2 (as previously stated in Chapter 2). Figure 3.15 presents the results. A visual inspection reveals that the WA maps optimizing the images are similar and there is no dependence with the imaged area size. For a better understanding, Figure 3.16 shows the values of 3rd and 4th order Zernike terms for all imaged areas.

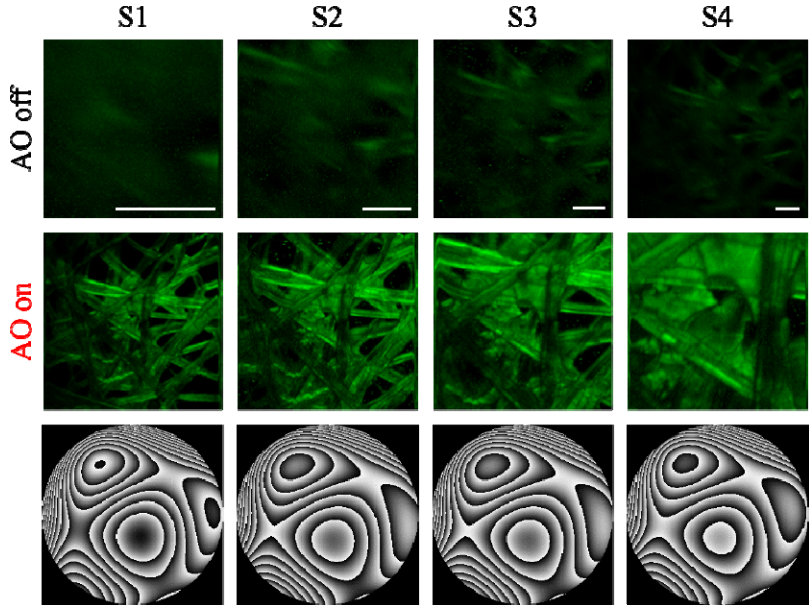

Figure 3.15: Relationship between the imaged area size and the optimum WA for a cellulose sample. The imaged plane corresponds to a depth location of 100 µm. Bar length 50 µm.

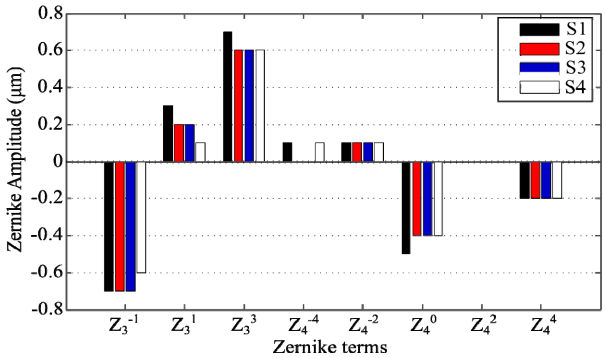

Figure 3.16: Zernike distribution for the different imaged areas.

To corroborate this founding, the algorithm was also used to improve different imaged areas in a number of samples. Figure 3.17 presents the improved images for two different imaged areas (S2 and S4) together with the corresponding WA maps in samples providing

TPEF and SHG signal. As it can be seen once again, these WA maps (and the corresponding Zernike terms, Figure 3.18) hardly changed between the two imaged areas, i.e. the improved images are nearly independent of the size of the imaged area. This behavior was similar for all samples and depth locations involved in the study.

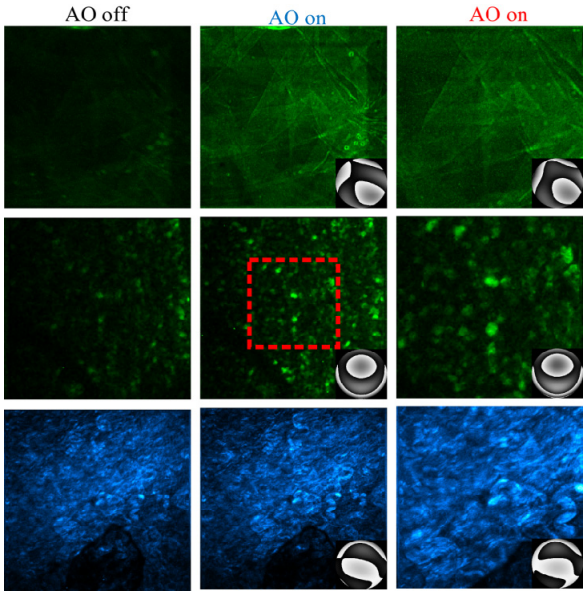

Figure 3.17: Influence of the imaged area on the optimum WA maps for TPEF (human ERM -top-, rat retina ganglion cells –middle-) and SHG (bovine sclera -bottom-) images. Left and middle panels: S4; right panels: S2.

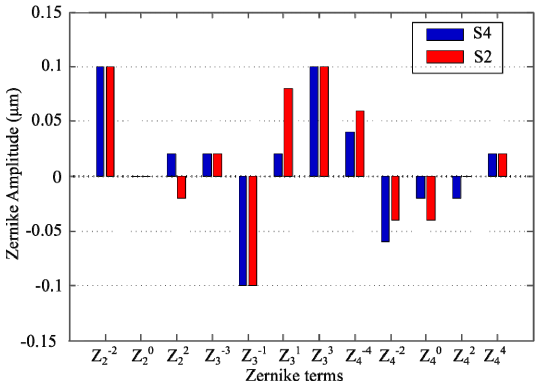

Figure 3.18: WA Zernike terms corresponding to the image improvement of the sample of the top row in Figure 3.17.

3.6. Influence of the Zernike control sequence

The MP microscopy images of previous sections were obtained using the hill-climbing algorithm in the increasing-mode direction. For this condition, the AO optimization started by correcting the term Z_2^{-2} (45°-astigmatism). The effects of using the algorithm in the decreasing-mode direction are investigated in this section. Figure 3.19 shows the results in a piece of cellulose. For the decreasing-mode direction, the algorithm started with term Z_4^0 (SA) and the Zernike terms were included in the order indicated in the horizontal axis of the bottom plot.

For both correction directions the final images were similar. Despite this, the WAs are different, although their RMS values did not differ much (1.05 and 0.94 µm, respectively).

For the increasing-mode direction, 2nd order terms (astigmatism) hardly had effect on the image improvement. There is a ~4-fold increase in the metric when adding 3rd order terms (especially Z_3^{-1} and Z_3^{3}), and an additional ~2-fold increase when including 4th order ones (mainly SA). In the decreasing-mode direction, most of the improvement was obtained when adding just the SA term (i.e. Z_4^{0}). The metric did not change until the term Z_3^{-1} (vertical coma) was included, leading to an additional 20% improvement. When adding the last term (Z_2^{-2}) a final improvement of about 7-fold compared to the original image was reached.

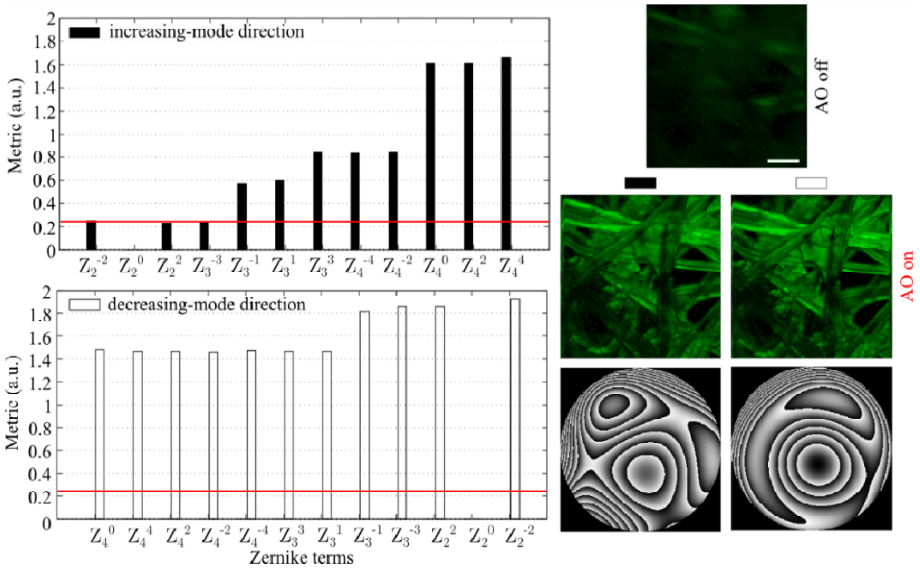

Figure 3.19: Metric values for the Zernike-mode optimization algorithm in the increasing (black bars) and decreasing (white bars) direction. The red line is the metric value for the original image before using AO. The WA maps are shown for direct comparison. Images correspond to a 180 µm depth layer within a piece of cellulose. Bar length: 50 µm.

The comparison between the Zernike-mode sequences was also carried in other samples. Figure 3.20 shows the results for an additional set of specimens. Similar to the results in Figure 3.19, although the WA maps differed, RMS values were similar. For a better understanding the Zernike distribution and the corresponding improvement are shown in Figure 3.21.

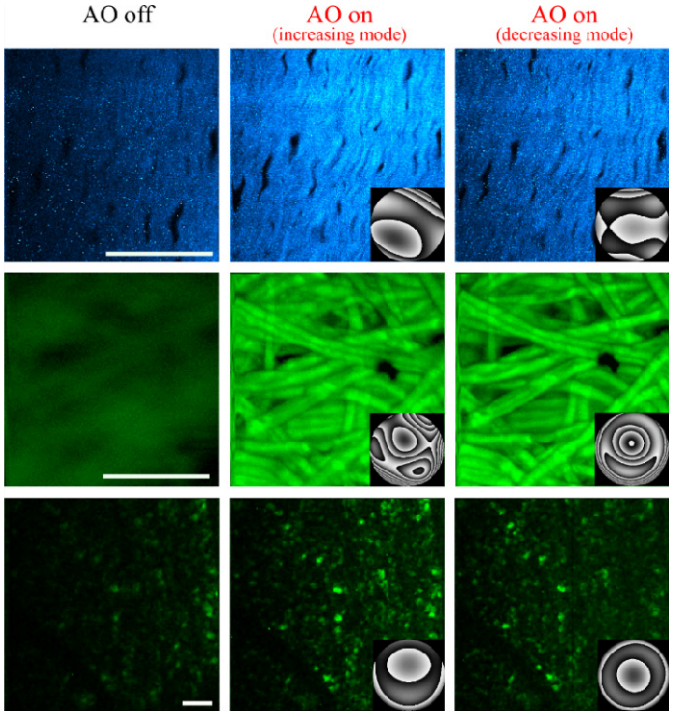

Figure 3.20: Examples of image improvement using the hill-climbing algorithm in the increasing and decreasing directions. Samples correspond to a paraffin-embedded bovine cornea (40-µm depth, upper panels), a piece of silk mesh (180-µm depth, middle panels), and the ganglion cell layer of a rat retina (30-µm depth, bottom panels). Bar length: 50 µm.

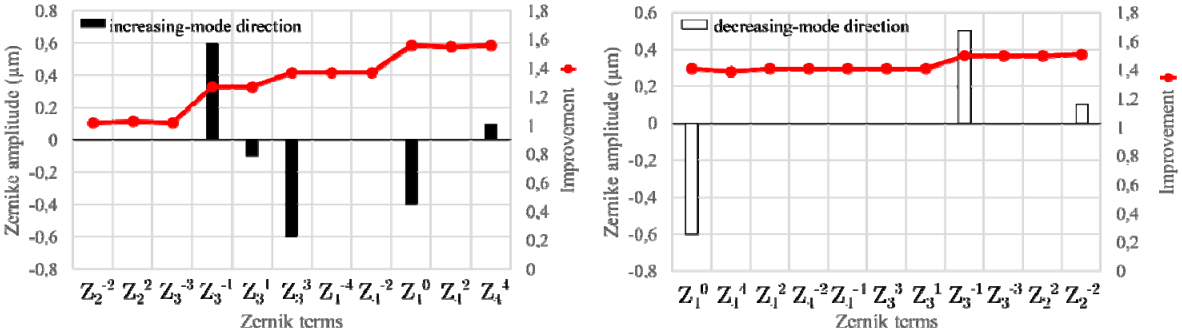

Figure 3.21: Zernike distribution (bars) and improvement (red symbols) corresponding to the silk mesh sample shown in Figure 3.20.

For a number of samples involved in the study and providing both TPEF and SHG signals, Figure 3.22 compares the RMS values of the WA maps in both correction directions. The data fit a significant linear relationship ($R=0.92$, $p<0.0001$).

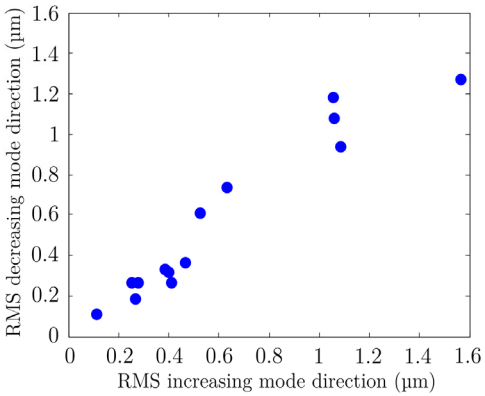

Figure 3.22: Comparison of RMS values of the WAs obtained when the AO procedure was used in the increasing and decreasing Zernike-mode directions for different samples used in this work.

3.7. Dominance of spherical aberration

Independent of the sample, the comparison between both Zernike-mode correction directions of the previous section has confirmed the dominance of the SA term (Hell *et al.*, 1993; Neil *et al.*, 2000; Sherman *et al.*, 2002; Lo *et al.*, 2005), especially when imaging layers placed at deeper locations. To better show this effect, this section will presents examples of improved images in different specimens when correcting just the term Z_4^0 compared to those when terms such as Z_3^3, Z_3^{-1} and Z_2^{-2} were also included. These results confirm the benefit of correcting just the SA term, when it is dominant at certain depth position within thick samples. This has been analyzed in detail in a recent paper by these authors (Bueno *et al.*, 2014). Although the contribution of the spherical aberration term varies among samples and depth location, this was more than 60% (to the total RMS) in most samples analyzed here.

Figure 3.23 shows the results for three different samples. Firstly, the samples were imaged without applying any correction (first column). Secondly, only SA was corrected (second column). The third column shows the improved images when adding other aberration terms (see caption for further details). To quantify the improvement, the total intensity across the image (i.e. the summation of all pixel values) was calculated and compared to the uncorrected initial image (Figure 3.24). For the images in the top row (human ERM) the increase in total intensity when correcting just for SA was 1.75. This went up to 1.82 when adding other terms. For the second sample (silk mesh) an improvement of 1.45 and 1.54 were respectively obtained. For the bottom sample (ganglion cell layer of a rat retina) the improvement values were 1.74 and 1.80. These results clearly show the dominance of the SA.

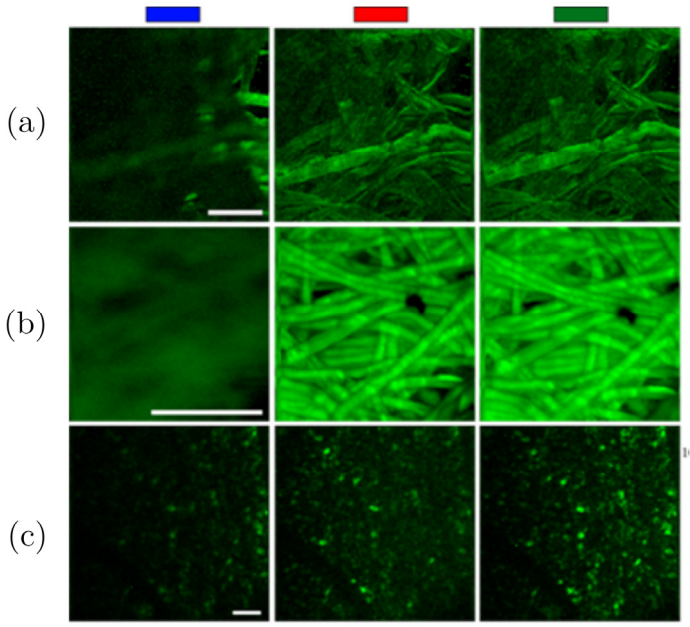

Figure 3.23: Example of MP images showing the benefit of correcting the SA term. Samples correspond to (a) a human ERM (50-µm depth), (b) a piece of silk mesh (80-µm depth) and (c) the ganglion cell layer of a rat retina (30-µm depth). Original image (first column); only SA corrected (second column); SA, astigmatism, trefoil and coma corrected (third column). Bar length: 50 µm.

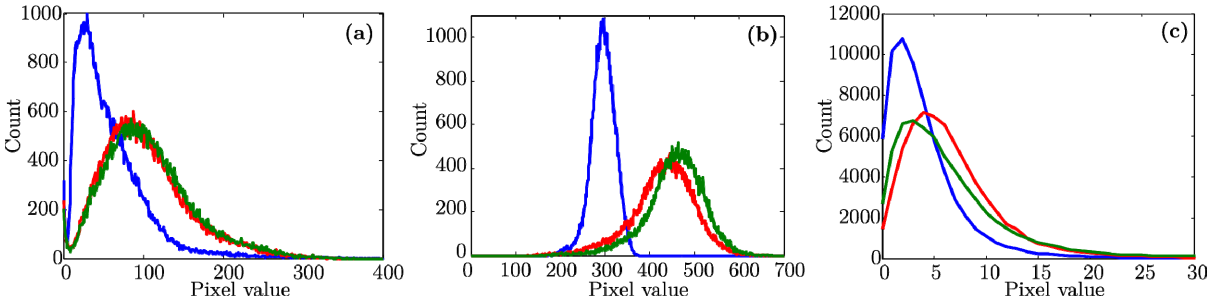

Figure 3.24: Histograms showing the image improvement in total intensity of the images in the previous figure. Labels are the same as in Figure 3.23.

3.8. Discussion

The major advantage of MP imaging is its capability of optical sectioning within non-stained biological samples. Typically, this employs a scanning system to raster scan the beam across the sample in order to get an image. By taking a series of images at successive depth locations, a 3D view of the sample can be constructed. Unfortunately, as deeper planes are imaged, degradation increases due to aberrations (Girkin *et al.*, 2009). To overcome this limitation WFSL techniques offer a fairly good solution. By selecting a specific image property as a metric and an optimization algorithm, the image at a particular depth location can be optimized by computing the WA that maximizes the selected metric.

In this chapter, the MP microscope described in Chapter 2 has been modified to include an LCoS-SLM, optimized for infrared light, as an AO element. The capabilities of the LCoS

modulator for WA manipulation have been explored in order to improve MP imaging, especially at deep locations within the specimens. The dependence of the final improved image on the Zernike correction control sequence has been investigated, as well as the influence of the imaged area size and the effect of depth.

Deformable mirrors and liquid-crystal SLMs have often been implemented into AO MP microscopes (Albert *et al.*, 2000; Neil *et al.*, 2000; Sherman *et al.*, 2002; Marsh *et al.*, 2003; Leray and Mertz, 2006; Rueckel *et al.*, 2006; Leray *et al.*, 2008; Débarre *et al.*, 2009; Bueno *et al.*, 2010; Cha *et al.*, 2010; Aviles-Espinosa *et al.*, 2011; Zhou *et al.*, 2011; Tao *et al.*, 2013). Recently, LCoS modulators have successfully been used to improve MP imaging at deeper locations within the specimens (Ji *et al.*, 2010, 2012). Unlike deformable mirrors (with continuity constrains), these devices are able to reproduce discontinuous profiles and increase the effective stroke by means of phase wrapping. Whereas the number of independent elements in a deformable mirror is about 100, in an LCoS device this is 4 orders of magnitude higher. LCoS devices also provide much higher resolution than regular SLMs, what leads to enhanced accuracy for WA correction. WFSL approaches might also benefit from the use of LCoS-SLMs since their inherent fidelity also permits open-loop operation with no need of feedback for achieving the intended final WA.

One of the main drawbacks when using LCoS devices is the requirement of linearly polarized light. In MP microscopy this would be important when analyzing the effects of polarization on SHG imaging, however that is irrelevant here due to the independence between aberrations and polarization (Bueno and Artal, 2001; Bueno *et al.*, 2006). Another important issue is the absorption coefficient. Depending on the angle of incidence, this might be higher than 50%. Its minimization is important to maximize the optical efficiency of the device and to minimize local heating (especially when using high-power mode-locked lasers). When highly transparent samples providing TPEF signal are imaged, this is not important, however in high-scattered samples providing SHG signal this absorption might be an additional factor limiting the optical penetration depth (see Chapter 4).

Since static samples are used in this work, the response velocity is not an issue. However, LCoS technology allows up to 60 Hz (Fernández *et al.*, 2009), values higher than those provided by regular liquid-crystal SLMs previously used in MP microscopy. This increase in the response speed is due to a direct control of the local refractive index by a CMOS (Complementary Metal Oxide Semiconductor) sheet placed below the liquid-crystal layer (Wang *et al.*, 2004). This may open new applications and possibilities in MP imaging of dynamic samples where the recording time must be reduced and optimized (Olivier *et al.*, 2009; Wang *et al.*, 2014).

In WFSL techniques, three elements are important: the metric or merit function, the algorithm and the correction control sequence. AO-MPM experiments have used different

metrics, such as mean image intensity (Débarre *et al.*, 2009), total image intensity (brightness) (Albert *et al.*, 2000; Sherman *et al.*, 2002; Jesacher *et al.*, 2009) or contrast (Marsh *et al.*, 2003). However, the choice of the metric does not limit the optimization speed. In our case image sharpness (i.e., the sum of squared pixel values) was chosen (Muller and Buffington, 1974; Marsh *et al.*, 2003; Olivier *et al.*, 2009a).

Several algorithms to perform image optimization in AO-MP instruments involving WFSL procedures can also be found in the literature (Albert *et al.*, 2000; Neil *et al.*, 2000; Sherman *et al.*, 2002; Marsh *et al.*, 2003; Wright *et al.*, 2005; Débarre *et al.*, 2009; Zhou *et al.*, 2011; Tang *et al.*, 2012). Comparison among different procedures are out of the scope of this Thesis and can be found elsewhere (Wright *et al.*, 2005; Skorsetz *et al.*, 2014). The choice of an algorithm depends on the requirements and goals of the investigation. In general, it mainly depends on the "best fit" to the sample being imaged. Algorithms such as genetic (Man *et al.*, 1999) or simulated annealing (Kirkpatrick *et al.*, 1983) are inherently more complex and require many iterations and resources. If time is an issue, random search algorithms have been reported to be a good compromise between speed and image enhancement (Wright *et al.*, 2005; Lubeigt *et al.*, 2010). Alternatively hill-climbing procedures offer less complexity and are appropriate for samples not prone to photo-bleaching of photo-toxicity (Marsh *et al.*, 2003) as the ones used here.

Moreover, iterative algorithms and correction strategies of WFSL systems have to be optimized to work efficiently. Nowadays, orthogonal functions such as Zernike polynomials are commonly used to effectively reduce the search space (Booth, 2006). This modal-based scheme in sequential use combined with hill-climbing algorithms has successfully been used in AO-MP microscopy. More recently, the principle of the imaged-based modal aberration sensing method and its adaption for 3D-resolved aberration measurements have been studied in detail (Zeng *et al.*, 2012).

A modal-based hill-climbing algorithm has been used here to improve images acquired with MP techniques. Although a number of samples was successfully tested, our interest was mainly focused on ocular tissues. Results were shown to be reproducible with time. Since samples were static, this shows the temporal stability of the laser beam as previously reported (Bueno *et al.*, 2009).

The use of Zernike polynomials have been reported to be efficient when using both deformable mirrors and liquid-crystal SLMs. Early MP imaging enhancement was based on the compensation of the SA term specially at deeper layers (Booth and Wilson, 2001; Sherman *et al.*, 2002). However, the influence of other terms might also be of importance not only in MP microscopy but also in other imaging techniques using WFSL procedures such as confocal microscopy (Booth *et al.*, 2002), retinal imaging (Hofer *et al.*, 2011) and optical coherence tomography (Bonora and Zawadzki, 2013).

The regular way of compensating aberration terms is starting with 2nd order terms (astigmatism) and running them in the increasing-mode direction. Here the final WAs in both increasing and decreasing control sequences have been compared. Results for different samples show that the optimum WA depends on the chosen control sequence direction although the final improved images did not differ much. Despite WAs differ, for each particular specimen the total RMS values for both WAs were similar. This indicates that different combinations of Zernike polynomials led to comparable improved images.

Since Zernike polynomials are orthogonal, this result might be contradictory at this point. Obviously, a particular WA is described by a unique combination of Zernike terms. However, the idea here reported differs from this. At a certain depth location the specimen-induced aberrations (generally understood as a total RMS value) reduce MP efficiency. Our goal has been to test if the image improvement can be reached by using different combinations of Zernike terms. It has been shown that different combinations led to similar improved images attending to a particular metric. This fact is not directly related to the mathematical properties of the Zernike terms but with the image improvement itself. In fact, it was found that the different compensations providing similar RMS values led to similar final images. This means that the plane-to-plane WA correction is not based on an exclusive WA map but in the compensation of a total RMS representing a "certain amount of aberration".

For most samples, the decreasing-mode direction provided the SA as the dominant term, especially at deeper locations, being the influence of the rest of terms minor. On the contrary, in the increasing-mode direction different terms contribute to get the best quality image. These results corroborate the fact that the spherical aberration itself might significantly contribute to enhance the images (mainly at deeper locations). A compensation of this aberration term using AO non-linear tomography would help to improve MP images in an easy and "fast" way, as recently reported (Bueno *et al.*, 2014).

Previously experiments combining LCoS devices and MP imaging used immersion objectives (Ji *et al.*, 2010, 2012). These compensated for part of the aberrations (mainly SA) and enhanced depth imaging due to refractive-index mismatch between the samples and the objective itself. Here we used an in-air objective and a backscattered configuration. Despite this and independently of the depth location of the imaged plane, the actual LCoS-SLM was able to generate the corresponding WAs to produce improved TPEF and SHG images. The procedure reported here provided images with improved contrast and enhanced lateral resolution not only at shallow planes, but also at different depth locations within the sample. Independently of the type of nonlinear signal, at every depth location the improvement of the image was noticeable. Although at shallow planes the effect was small (due to the low amount of aberration), results show that the RMS values increased linearly with depth. The optimum WA depended on both the specimen and the depth location. This general behavior was found in all the specimens.

In AO-MP microscopy it is also important to consider the variations of the aberrations across the field of view. If for a given depth location, a larger (or smaller) area is imaged, the required WA to optimize the image might be different (Schwertner *et al.*, 2004). Lateral scan aberrations can also become significant in microscopy and generally increase with the scan angle (Marsh *et al.*, 2003). Simmonds and Booth have reported a model of spatially variant aberration correction through multi-conjugate AO (Simmonds and Booth, 2013). They claimed that those aberrations can be partially compensated by correcting for the entire field of view. Moreover, Zheng and co-authors (Zheng *et al.*, 2013) have reported a phase retrieval-based procedure to experimentally recover the spatially varying WAs in wide-field imaging systems. In this Chapter 3 different fields of view were imaged and optimized in a number of samples (largest imaged area: 360x360 μm2). It was found that for a certain depth location within a sample, the WAs were similar for imaged areas. This is consistent with previous results (Aviles-Espinosa *et al.*, 2011).

The reason for this "homogeneity" in the WA might be that the samples here used do not present so much variation across the field of view (especially ocular tissues). Since slower scan rates are expected when imaging a bigger area, the current results lead to the fact that an improved MP image of a bigger area can be achieved, by correcting only over a particular smaller region (imaged in a shorter time). This is of interest for future applications of the reported procedure to living eyes, where the recording time might be an issue.

The SA itself might significantly contribute to enhance the images (mainly at deeper locations). It is well known that the use of a high NA objective induced SA due to the refractive-index mismatch at the interface between materials (Booth & Wilson, 2001, Booth et al., 2002). The refractive index mismatch between the objective and the specimen resulted in the significant aberration, in particular SA (Hell, 1993). Here we use small NA objective (0.5x). Lower NA are less susceptible to aberrations, but we did not use any immersion medium to compensate for refractive index mismatches. Despite this can be seen as the worst scenario of index mismatch, the procedure succeeded.

An LCoS-SLM device has been implemented into a MP microscope to enhance the contrast and resolution of images without noticeable photo-damage. The microscope was set to use an in-air objective and a backscattered configuration. A modal hill-climbing algorithm has been developed to successfully correct for the aberrations in samples providing both TPEF and SHG signal.

A comparison of optimum images given by two different Zernike-mode control sequences has also been reported. This image improvement might allow a better visualization of ocular tissues, in particular those suffering from some pathology with features located at deeper locations. The main drawback of the reported method is the number of iterations used (although these can be reduced (Débarre *et al.*, 2007)). This would limit its use with dynamic

samples or living specimens. The present experimental system is not optimized for speed but this will be improved when moved to in-vivo imaging in the near feature. As already reported (Bonora and Zawadzki, 2013), the combination of modal correction of low-order aberrations with a stochastic parallel gradient descent algorithm for high-order aberrations (Hofer *et al.*, 2011) might improve the performance when dynamic measurements are involved.

CHAPTER 4

Multiphoton imaging at deeper layers with adaptive optics control of spherical aberration

In this chapter, an alternative approach to increase penetration depth in 3D MP microscopy imaging is reported. It is based on the manipulation of the SA pattern of the incident beam with an AO device while performing fast tomographic MP imaging. When inducing SA the image quality at best focus is reduced, however better quality images are obtained from deeper planes within the sample. This is a compromise that enables registration of improved 3D MP images using non-immersion objectives. Examples on samples providing different types of non-linear signal are presented. The implementation of this technique in a future clinical instrument might provide a better visualization of corneal structures in living eyes.

TPEF (Denk *et al.*, 1990) and SHG (Campagnola *et al.*, 2001) imaging techniques are being used in different areas of biomedical research mainly due to their inherent optical sectioning and their noninvasive 3D capabilities. As demonstrated in Chapter 3, aberrations caused by the alignment and the quality of the optical elements, the objective-sample refractive-index mismatch and the inhomogeneous structure of the sample (Neil *et al.*, 2000; Sherman *et al.*, 2002; Marsh *et al.*, 2003; Bueno *et al.*, 2009; Débarre *et al.*, 2009) limit MPM imaging performance (Sherman *et al.*, 2002).

AO yielded substantial improvements in the images obtained with MPM (Neil *et al.*, 2000; Sherman *et al.*, 2002; Marsh *et al.*, 2003; Rueckel *et al.*, 2006; Débarre *et al.*, 2009; Bueno *et al.*, 2010; Cha *et al.*, 2010; Aviles-Espinosa *et al.*, 2011). In an ideal situation, for each location within the sample, the corresponding wavefront should be accurately measured and corrected. However, since the plane-by-plane wavefront assessment may be complex in thick samples, most of the authors used WFSL techniques for aberration corrections (Neil *et al.*, 2000; Sherman *et al.*, 2002; Marsh *et al.*, 2003; Débarre *et al.*, 2009). As previously reported in Chapter 3, strategies were based on different algorithms, modifying the incoming wavefront to improve the recorded image according to different quality metrics, such as intensity, contrast, or sharpness (Wright *et al.*, 2005; Débarre *et al.*, 2009). These experiments provided image quality improvements by means of an indirect measurement of the actual aberrations within the sample. Only a few studies combines Hartmann-Shack wavefront sensors and correction in MPM (Rueckel *et al.*, 2006; Azucena *et al.*, 2010; Cha *et al.*, 2010; Aviles-Espinosa *et al.*, 2011). Another approach based on pupil segmentation has also been shown (Milkie *et al.*, 2011; Ji *et al.*, 2012).

It is well known that the use of a high numerical aperture (NA) objective induced SA due to the refractive-index mismatch at the interface between materials (Booth and Wilson, 2001; Booth *et al.*, 2002). When a microscope is focused into a specimen, SA is induced, leading to a degradation of the images of deeper layers. Then, SA plays an important role when imaging thick samples with a MP microscope. Moreover, it has been reported, that SA is often the dominant term (Neil *et al.*, 2000; Sherman *et al.*, 2002; Lo *et al.*, 2005; Muriello and Dunn, 2008; Débarre *et al.*, 2009), and its correction leads to image enhancement. This was also analyzed in detail in section 3.3.5.

Methods to correct for (or minimize) this unwanted SA in MP microscopy were mainly based on the use of an objective correction collar (Lo *et al.*, 2005; Muriello and Dunn, 2008) or a WFSL-AO device (Neil *et al.*, 2000; Sherman *et al.*, 2002; Marsh *et al.*, 2003; Olivier, Débarre, *et al.*, 2009). For these experiments high-NA immersion objectives and previously chosen cover glasses (to minimize the refractive-index mismatch and the SA produced at the corresponding interface) are often used. The correction collar is a manual method only valid for a well-defined set of cover glass. An optical performance depends on the relationship between the refractive indices of the immersion medium and the sample, and how uniform the refractive index within the specimen is (Lo *et al.*, 2005).

Alternatively, WFSL schemes offer a different strategy to compensate for different aberration terms by indirect assessment (Neil *et al.*, 2000; Sherman *et al.*, 2002; Marsh *et al.*, 2003; Débarre *et al.*, 2009). AO multiphoton microscopes based on modal Zernike correction (Wright *et al.*, 2005) have reported interesting results.

Although optical sectioning is the big advantage for MPM, very short DOF is not always desirable (Master, 2008). To image an entire stack in 3D, thin slices of different depth locations are necessary and this is time consuming. One approach is the multifocal MPM (Bewersdorf *et al.*, 1998). As

an alternative approach, wavefront coding was developed for increasing DOF for imaging systems. Wavefront coding introduces a known, strong optical aberration that is inherent to defocus and image post-processing is required (Quirin *et al.*, 2013).

Another approach in MPM is to extend the DOF by using Bessel-like beams. This can be done by using, for instance, a tunable acoustic gradient index lens (Olivier *et al.*, 2009b), axicon lenses (Dufour *et al.*, 2006; Thériault *et al.*, 2013), annular illumination with phase plates (Botcherby *et al.*, 2006), and phase-axicon or annular illumination pattern generated with a SLM (Planchon *et al.*, 2011; Fahrbach *et al.*, 2013).

Extend the DOF of an optical system can also achieved by introducing an amount of SA (Mouroulis, 2008). For instance, (Sasaki *et al.*, 2012) demonstrated an extended DOF by introducing AO controlled SA in spectral domain optical coherence tomography. SA also may help to optimize MP signals from deeper layers. In this sense, the aim of this chapter is to further analyze the influence of the SA on 3D multiphoton imaging and in particular the effect in deeper sample layers. We will examine the possibility of using a non-immersion objective and an AO module to optimize both TPEF and SHG imaging in non-biological samples and ocular tissues.

Despite all these previous experiments, the effects of partial correction or induction of pure aberration terms have not been studied in detail (this Thesis presents some results on this in Section 3.6). In particular, SA increases imaging depth (i.e. induced a larger DOF) a feature that can be used in 3D microscopy. Therefore, it is conceivable that the manipulation of the wavefront aberrations of the incident laser beam (via AO) to induce pre-defined values of SA may help to optimize MP signals from deeper layers. In this sense, the aim of this chapter is to further analyze the influence of the SA on 3D MPM imaging and in particular the effect in imaging deeper sample layers. The possibility of using a non-immersion objective and an AO module to optimize both TPEF and SHG imaging in non-biological samples and ocular tissues is also explored.

4.1. Experimental system with an LCoS-SLM and procedure

The system is the same as that described in the previous chapter. The fs laser beam passes through the LCoS-SLM used for wavefront manipulation before entering the microscope (Figure 4.1).

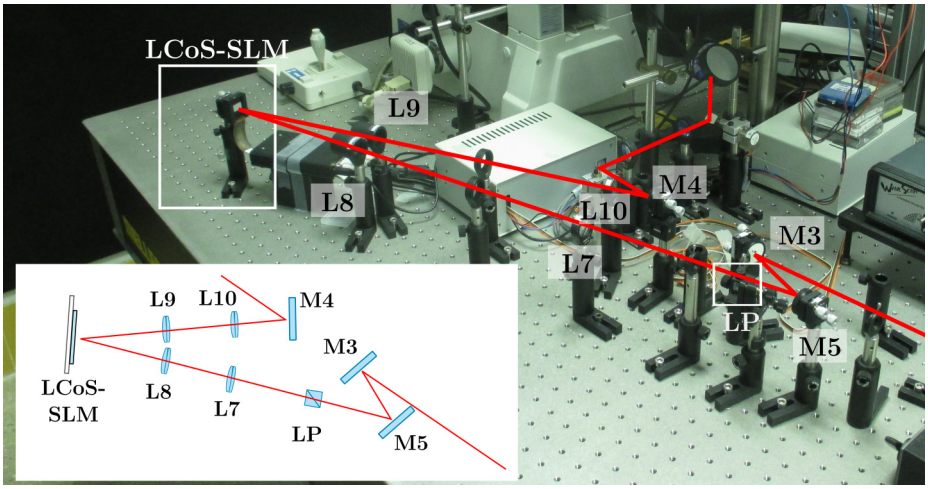

Figure 4.1: Details of the LCoS-SLM used for the purpose in this chapter. L7-L10, lenses; M3-M5, mirrors; LP, linear polarizer.

The experimental procedure consisted on generating different and controlled amounts of SA to enhance the quality of MP images at different planes within thick samples. Different amounts of SA were applied to the LCoS-SLM to maximize a pre-defined metric of the acquired images as already indicated in Figure 3.4 (hill-climbing algorithm). When the metric value reached a maximum, the corresponding SA value was set to be the optimum SA correction. For the sense of completeness Figure 4.2 shows a schematic of the procedure. This approach was used to determine the optimum SA for different ocular tissues (cornea, retina and ERM) at different depth locations.

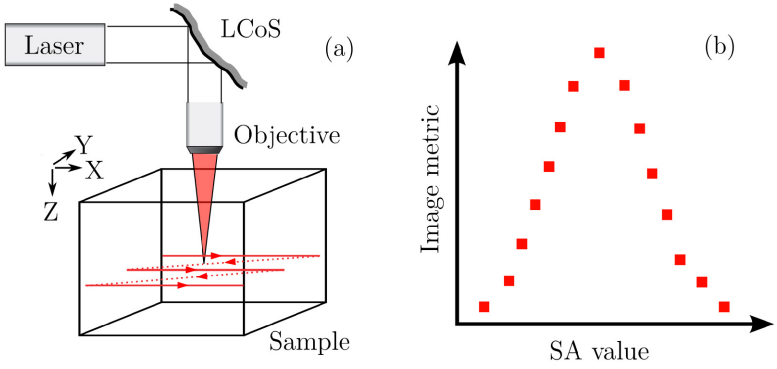

Figure 4.2: (a) The WA of the illumination laser beam is manipulated by the LCoS-SLM before imaging a plane located at a particular depth location. (b) Different SA values are induced by the LCoS-SLM in order to maximize the chosen metric.

4.2. Experimental system with a deformable mirror and procedure

Since LCoS-SLMs provide a high number of actuators (pixels), they are efficient devices to accurately shape the wavefront of a laser beam. However, one of the main obstacles is their low reflectivity that might reduce the effectiveness of MP processes and limit the contrast of the acquired images.

The LCoS-SLM has a reflectivity of 60-75% (given by the manufacturer). This is a very critical issue when dealing with biomedical applications, due to their quadratic dependence with the absorption process with the incident intensity. In particular, SHG imaging needs higher intensities than TPEF and the use of an LCoS device might limit the performance of the MP microscope, especially at deeper layers within the specimens.

The reduction in signal when the laser passes the LCoS was measured by comparing the power measured at the microscope entrance when the laser beam passes or over-passes the LCoS (Figure 4.3). The slope of the best linear fit is 0.66 what corroborates the absorption effects of the device indicated by the manufacturer.

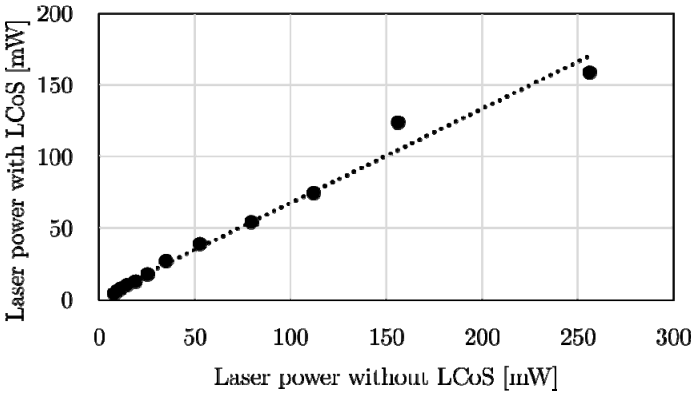

Figure 4.3: Laser power reduction due to the absorption effects of the LCoS-SLM. The best liner fit corresponds to y=0.66x+2.26 (R^2=0.98).

To overcome this limitation the experimental setup was modified to include an AO module composed of a DM (Boston Micromachines, Cambridge, MA, USA) and a HS wavefront sensor (WFS150-5C, Thorlabs Inc., Newton, NJ, USA). The sensor has a pitch of 0.15-mm and a focal length of 3.7-mm. The DM was a gold-coated MEMS-type with 140 actuators and a typical high reflective factor of 99 %. The actuators provide 3.5 µm of stroke. Figure 4.4 shows a picture of the AO module used to control and manipulate the laser beam WA while MP image recording. The AO module was calibrated in a previous operation using the software provided.

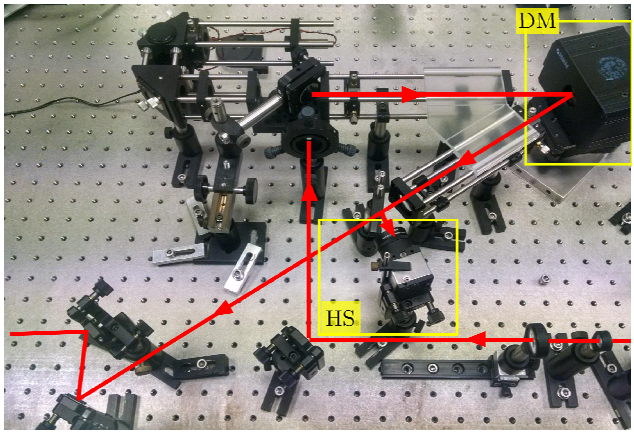

Figure 4.4: AO module composed of a DM and a HS sensor.

Figure 4.5 depicts a schematic setup of the entire system. The high-power laser beam passes through the AO module before entering the MP microscope. The HS sensor measures the laser beam WAs and those induced by the DM. They are expressed as a Zernike polynomial expansion up to 5^{th} order across a 4-mm pupil. The appropriate DM shape to compensate for the measured WAs was determined in a closed loop.

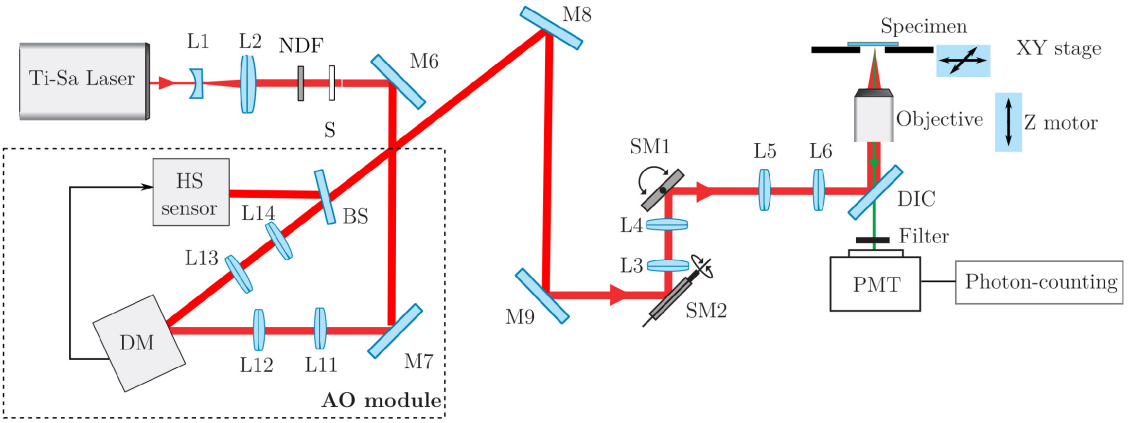

Figure 4.5: Schematic of the AO MP microscope including a HS sensor and a DM (not to scale). L1-L6 and L11-L14, lenses; NFD, neutral density filter; S, shutter; SM1-SM2, scanning mirrors; M6-M9, mirrors; DIC, dichroic mirror; PMT, photomultiplier tube.

By setting the appropriate DM shape, the system was also able to reach a final WA composed of any possible combination of Zernike modes (the limit is imposed by the DM stroke). The AO module has been used to produce pre-defined values for SA (Z_4^0) correcting for the rest of the aberration modes. To achieve this, initially the AO system measured the beam's WA and set these values to the target aberration, except for the SA whose value was previously stated as desired.

Figure 4.6 presents the idea of this approach. An aberrated laser beam leads to a blurred focal spot what compromises the quality of the acquired images (Figure 4.6(a)). After correcting the laser beam aberrations and those of the microscope optics, the focal spot is much sharper, especially when imaging shallow planes (Figure 4.6(b)). Then, a certain amount of SA is set as a target. The focal spot changes according to this aberration presenting an elongated shape, closely related to an extension of the DOF as explained in Section 4.1 (Figure 4.6(c)).

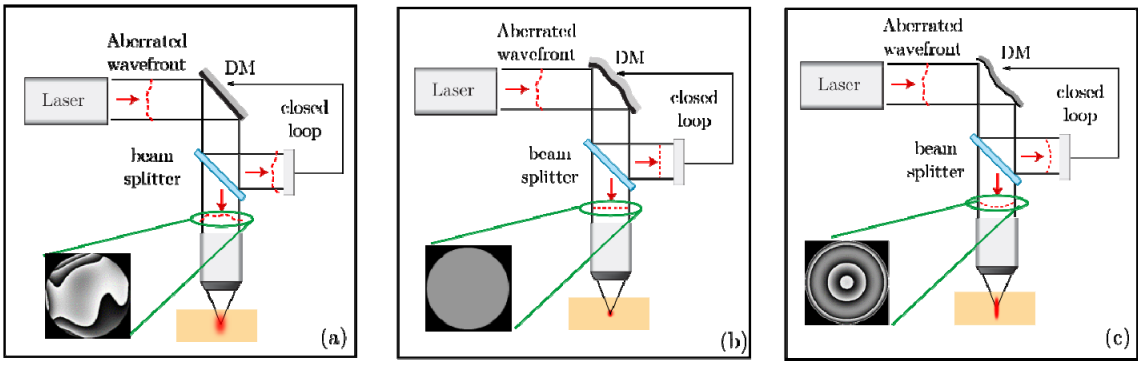

Figure 4.6: Schematic AO procedure here used. (a) AO module OFF; (b) AO module ON for laser beam and microscope optics WA correction; (c) AO control to generate of a certain amount of SA.

To better show on how the SA can expand the DOF Figure 4.7 depicts the simulation of a focal spot and the axial intensity distribution of light for different amounts of SA. With higher SA the maximum intensity is reduced, since the intensity is spread along the axial direction. The effect of

intensity spreading along the Z direction of the light propagation is used to produce nonlinear excitation at different depth locations.

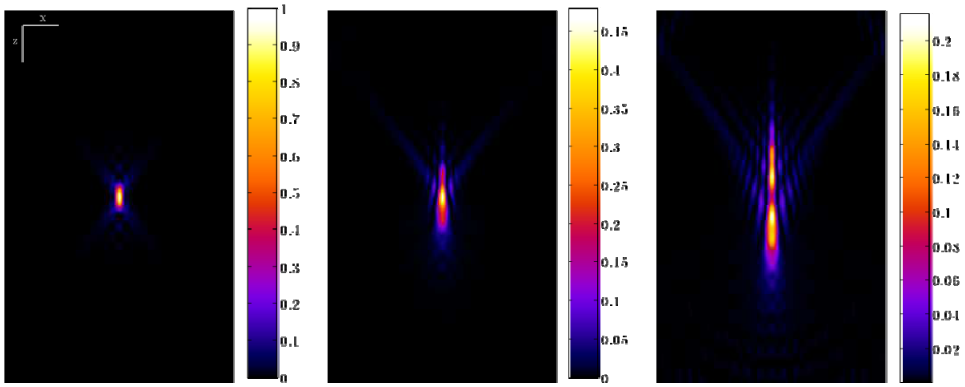

Figure 4.7: Intensity distribution of the focal spot along the Z direction for different amounts of SA (increasing from left to right).

As a first experimental test, the focal spot on an empty microscope slide was recorded for three different experimental conditions (Figure 4.8). The improvement of the laser spot can be observed when the AO was in operation. This can be compared with the shape obtained when an SA pattern was introduced.

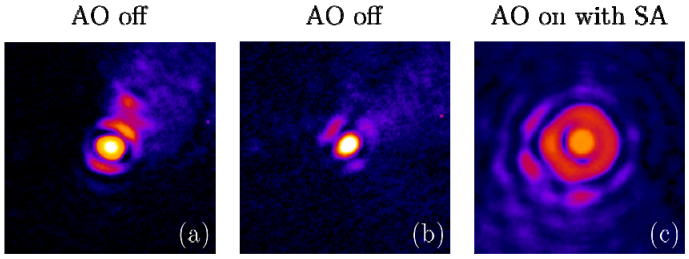

Figure 4.8: Focal spot without AO correction (a), with closed loop correction (b) and with a certain amount of induced SA (c).

The procedure used with this experimental configuration is schematically described in Figure 4.9. The system was first set to sequentially record MP tomographic images (cross-sectional) for different amounts of SA induced by the AO module (Figures 4.9(a) and 4.9(b)). SA values were produced in steps of 0.05 µm. This imaging modality permits a fast transversal visualization of the sample. From each tomography the averaged intensity profile as a function of depth was automatically computed (Figure 4.9(c)). The image with the highest area under the intensity profile was considered to provide the most appropriate SA value for the sample under study (Figure 4.9(d)). Once this optimum SA value was determined, regular stacks of XY MP images at different depth locations were recorded, without and with inducing this optimum SA value (Figures 4.9(e) and 4.9(f)).

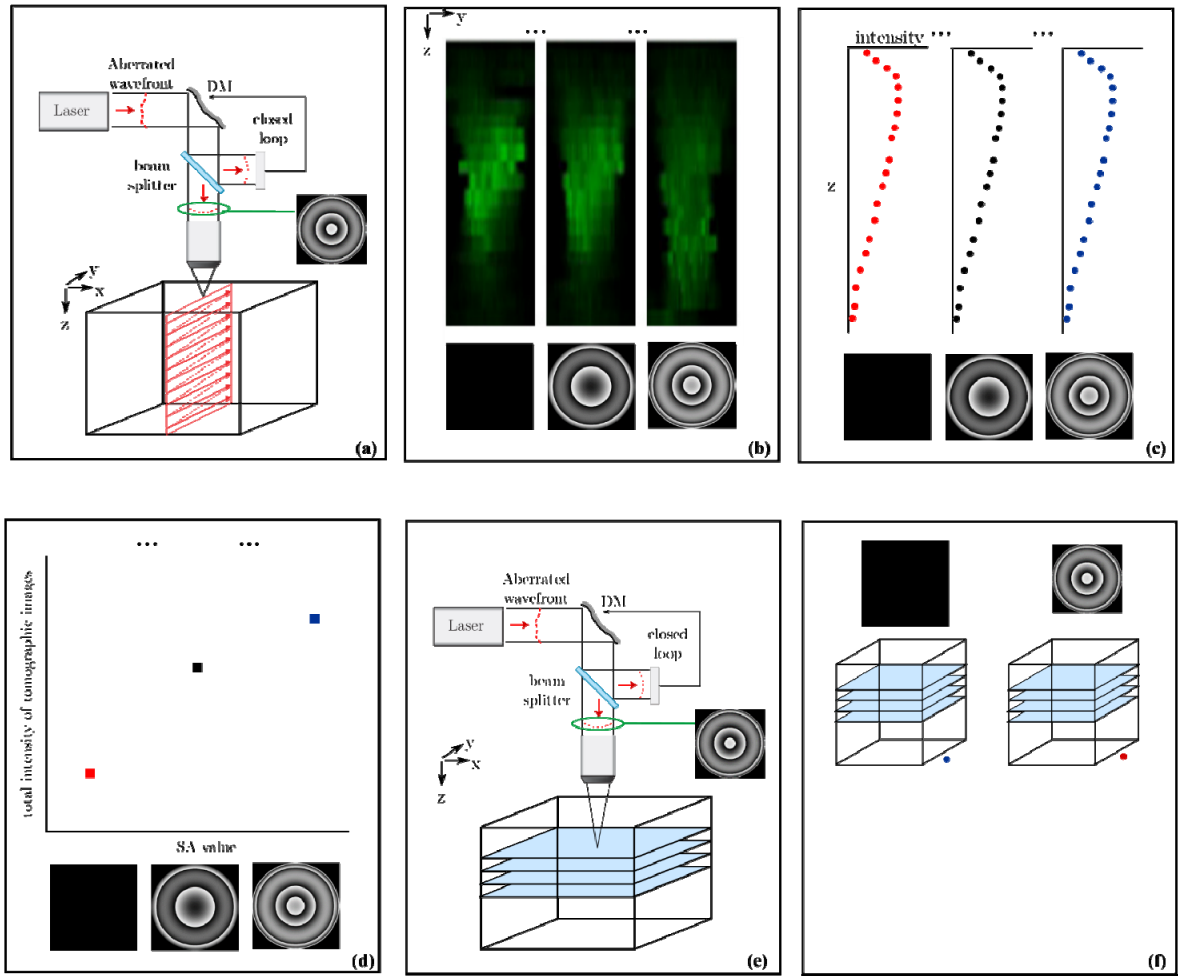

Figure 4.9: Experimental procedure for SA control with a DM (see text for details).

4.3. Effect of spherical aberration correction on a single plane

The influence of correcting for SA was first tested at individual planes of different samples. In a first and preliminary experiment we tested the influence of SA on the best imaged plane (this plane is our 0-µm depth location). Figure 4.10 shows this for a piece of cellulose. As expected, for shallow layers, the addition of both negative (Figure 4.10(b)) or positive (Figure 4.10(c)) values of SA only leads to a reduction in the image quality.

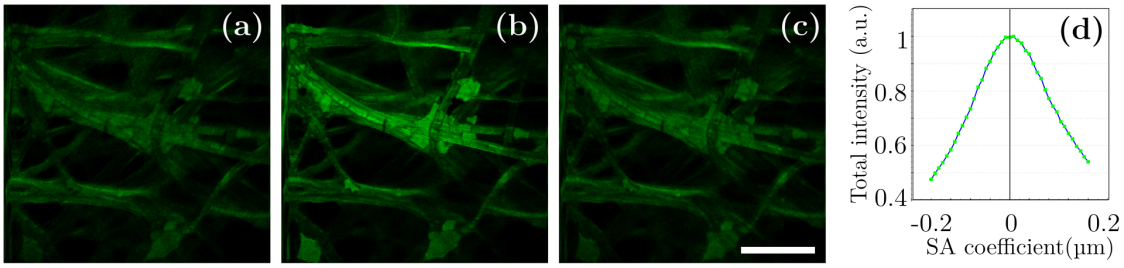

Figure 4.10: Effects of SA on MP images at a shallow depth location. (a) -0.2 µm of SA; (b) without SA; (c) +0.2 µm of SA. (d) Total intensity of the images as a function of the amount of SA. The sample corresponds to a piece of cellulose. Bar length: 50 µm.

In the second part of the experiment, different samples were tested at different depth locations. Since image acquisition is compromised by aberrations deep inside the sample (see Chapter 3), the images appear blurred as shown in left column of Figure 4.11. Given a particular plane within the sample, the addition of a particular amount of SA aberration restores the image quality. Figure 4.11 shows this effect for two samples providing TPEF and SHG signals at a depth location of 20 µm. For these particular samples the optimum SA were -0.3 µm (TPEF) and -0.1 µm (SHG), providing a total intensity signal increase of 1.71x and 1.27x, respectively.

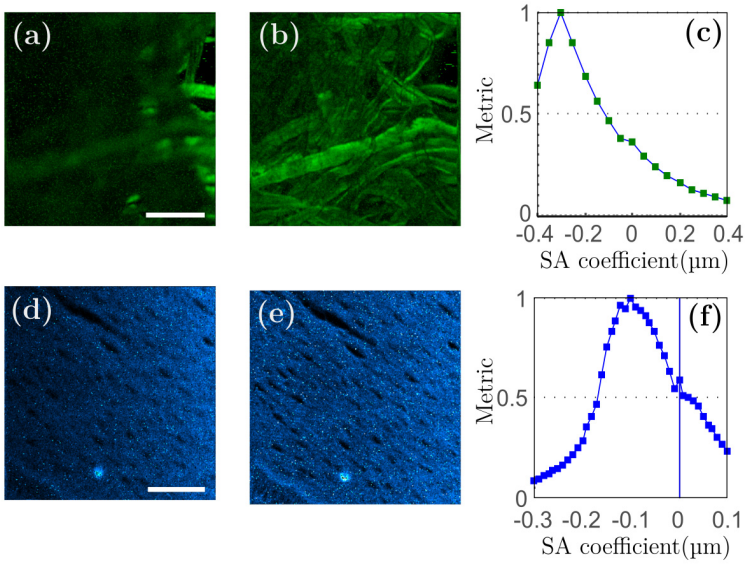

Figure 4.11: Effects of correcting for SA for TPEF (top row, human ERM) and SHG (bottom row, bovine cornea) images. (a, d) Without SA correction; (b, e) with SA correction; (c, f) total intensity of the images as a function of the amount of SA. Depth location within the sample: 20 µm. Bar length: 50 µm.

Figure 4.12 presents an example of TPEF images at different depth locations with and without SA correction. The signal level, contrast and resolution are affected by the aberration at deeper locations (top row). The improvement due to SA correction can be qualitatively observed in the bottom row. Each plane can be optimized individually. The total signal improvement in this example was 1x, 1.26x, 1.79x and 2.29x for the different depth locations shown in Figure 4.12. The introduced SA coefficients were respectively 0, -0.3, -0.45 and -0.85 µm.

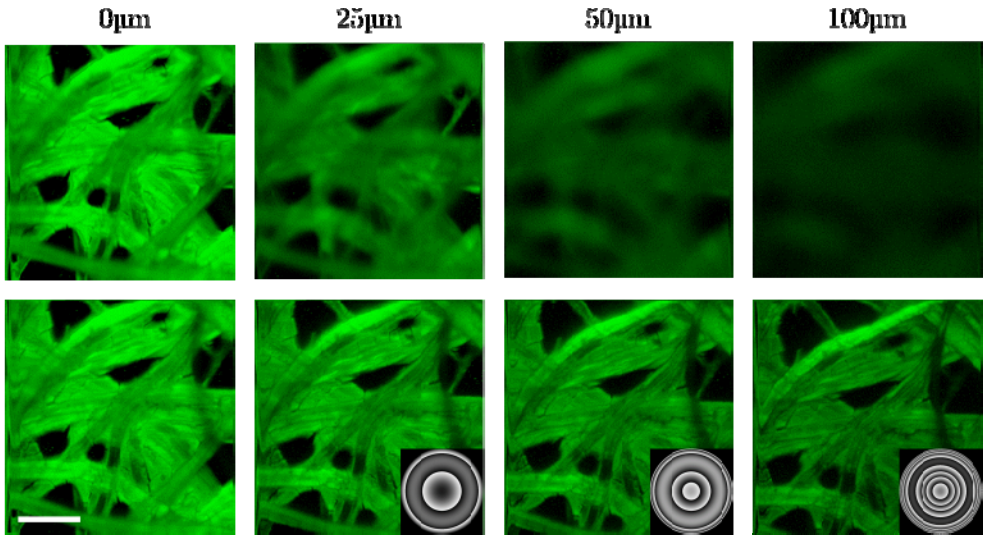

Figure 4.12: TPEF images for different depth positions acquired without using the LCoS-SLM (upper panels). Bottom panels correspond to the improved images when inducing SA with the amount determined by the hill-.climbing algorithm. The sample is a piece of cellulose. Insets are the 2pi-phase-wrapped WAs displayed by the LCoS device. Bar length: 50 µm.

An entire 3D stack (180x180x100 µm) in a sample of cellulose is shown in Figure 4.13(a). XY-images were acquired every 5 µm along the Z-direction. For each depth location, 21 images were acquired to determine the optimum SA value.

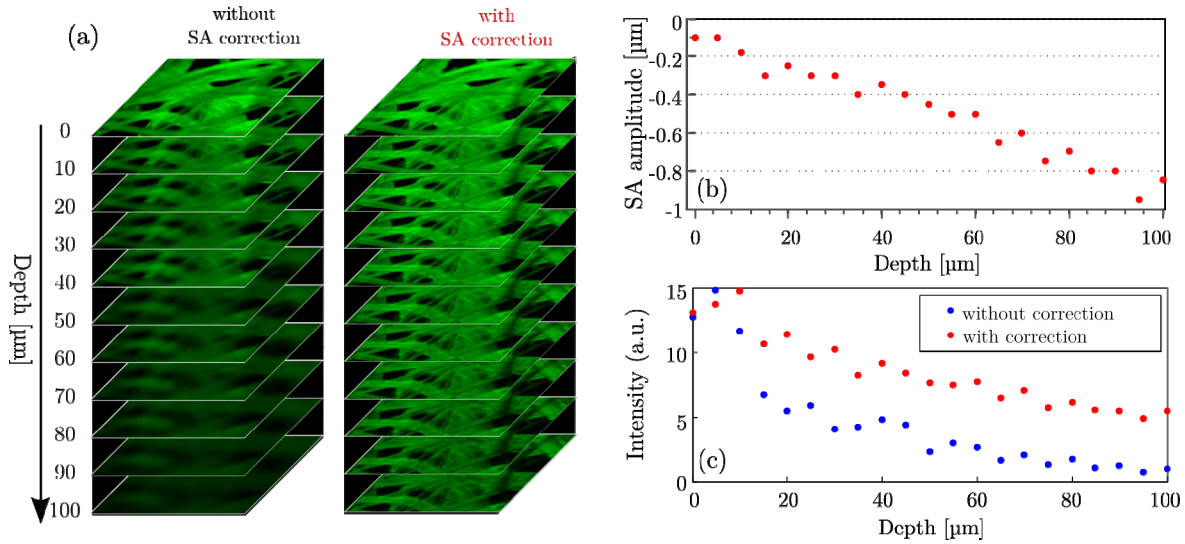

Figure 4.13: (a) Comparison of a stack of TPEF images without (left) and with SA correction (right); (b) optimum amounts of SA as a function of depth; (c) total intensity of the images as a function of depth without and with SA correction.

Once the set of optimum SA values was known, this was used to acquire the entire 3D stack through plane-by-plane correction. Figure 4.13(b) shows the optimum SA values for each depth location. The plot presents a linear increase in the SA absolute value. In Figure 4.13(c) the total intensity values of the acquired images without and with SA correction are depicted for the different depth locations. As already stated, without AO correction the intensity signal decreased at deeper locations (blue dots in Figure 4.13(c)). With AO correction the intensity along the different depth locations also decreases (red

dots in Figure 4.13(c)), however at each position the TPEF signal is higher when compared to the conditions without using AO.

The decrease in image quality at deeper locations is due to the reduction of effectiveness of the MP processes. At each single pixel of the image the photon collection reduces and images appear noisier. This effect is more noticeable if the MP phenomenon for a particular depth within a sample requires higher levels of laser power, and these are limited by the optical components of the experimental system (for instance, the LCoS-SLM).

In this sense, the differences in intensity reduction for a 3D image stack have been measured when using the two devices described in section 4.2.1: the LCoS-SLM and the DM mirror. This has been plotted in Figure 4.14 for the SHG signal provided by a chicken cornea. Unlike the LCoS-SLM (blue dots), the DM (red dots) enables imaging deeper layers (posterior stroma in this case) with enough signal levels to be processed. This means that for thick samples the use of a DM as an AO device is more appropriate. In this sense, the results included in the following sections have been obtained with the experimental configuration including the DM and described in section 4.2.2.

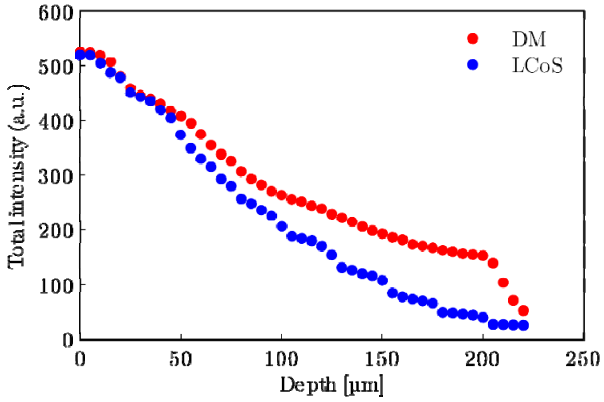

Figure 4.14: SHG intensity (chicken cornea) as a function of depth using AO imaging with an LCoS-SLM (blue dots) and a DM (red dots).

4.4. Spherical aberration and tomographic imaging

As explained in the procedure described in Figure 4.9, an optimum value of SA was computed using tomographic images of the samples acquired for different amounts of SA (see an example of these images in Figure 4.15(a)). For each tomographic image (and SA value) the averaged intensity profile was computed. Figure 4.15(b) shows the impact of inducing different controlled amounts of SA (-0.1, -0.2, and -0.3 µm) as a function of the sample's depth compared to the case of complete aberration correction (0 µm).

When SA was not included, the TPEF signal decreases with depth because of the influence of the specimen aberrations themselves (red dots in Figure 4.15(a)). The intensity values reduced at the best imaged plane when SA was induced: the higher the SA the more reduction. For SA=-0.1 µm (blue dots) the intensity was below the optimal one and provided similar values for deeper locations, as seen by comparing blue and red dots. However, this behavior clearly changed when adding larger values of SA. For this sample, this occurred when SA was larger than -0.15 µm (green and black dots). The arrow in the plot indicates where the behavior was reserved, i.e., a better TPEF signal was obtained when

imaging deeper into the sample. This implies an extended imaging depth (or alternatively an increase in the DOF) from deeper positions within the sample.

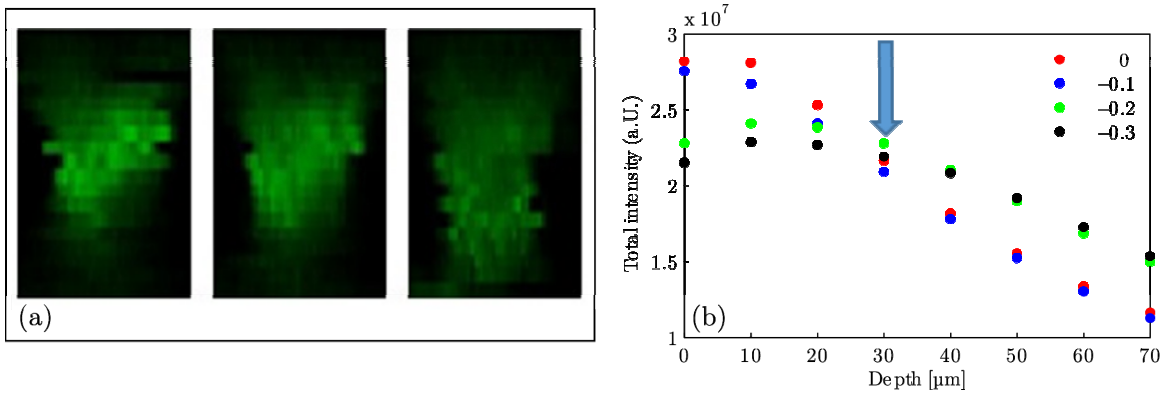

Figure 4.15: (a) Comparison of tomographic TPEF images of a single cellulose fiber for different values of induced SA (0 µm, left; -0.1 µm, center; -0.2 µm, right). (b) Intensity profiles as a function of depth, when inducing different controlled amounts of SA compared to the case of complete aberration correction (red dots).

4.5. 3D imaging with a unique predefined spherical aberration value

From the intensity profiles shown in Figure 4.15(b) the optimum SA value was determined and 3D MP imaging immediately performed. (i.e., XZ images along the Z direction). For comparison purposes these stacks of images for different depth positions were recorded for two experimental conditions: with and without the optimum SA value. This 3D imaging gives us information on the interaction between SA and the quality of images from deeper planes.

Figure 4.16 presents an example of TPEF images at different depth locations for two experimental conditions: SA=0 µm (top row) and SA=-0.2 µm. The improvement of images at planes located at 50 µm and 75 µm within the sample can be qualitatively observed.

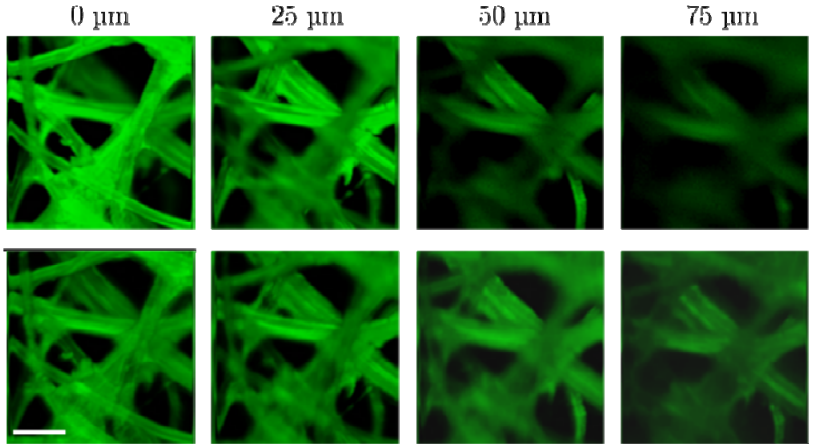

Figure 4.16: TPEF images for different depth locations acquired with all laser beam aberration corrected (top row) and -0.2 µm of induced SA (optimum value for this sample, bottom row). The sample corresponds to a piece of cellulose. Bar length: 50 µm.

Figure 4.17(a) presents the corresponding total intensity values (across the entire images) as a function of depth. The tendency for the rest of the quality metrics (not shown here) was also similar.

Moreover, although different image quality metrics are expected to measure different image properties (Hunter *et al.*, 2007), the reversal point positions (see the arrow) hardly differ among the different metrics (not more than 3 µm for the samples here used). Figure 4.17(b) presents the improvement in total TPEF signal versus depth position. This becomes positive when the effect of the SA is reversed. Similar results are obtained for a human ERM (also providing TPEF signal) shown in Figure 4.18. The corresponding improvements are shown in Figure 4.19.

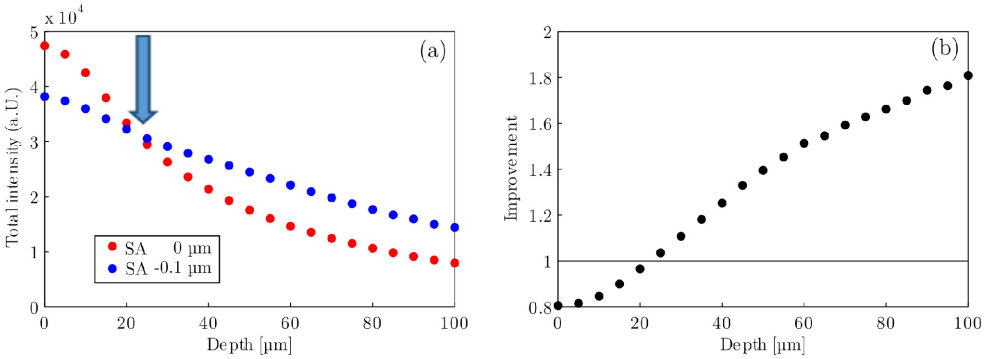

Figure 4.17: Effect of inducing -0.2 µm SA (red line) compared to the case of null SA (blue line). (b) Corresponding improvement in the total TPEF intensity of the images as a function of depth. The sample is that of Figure 4.16.

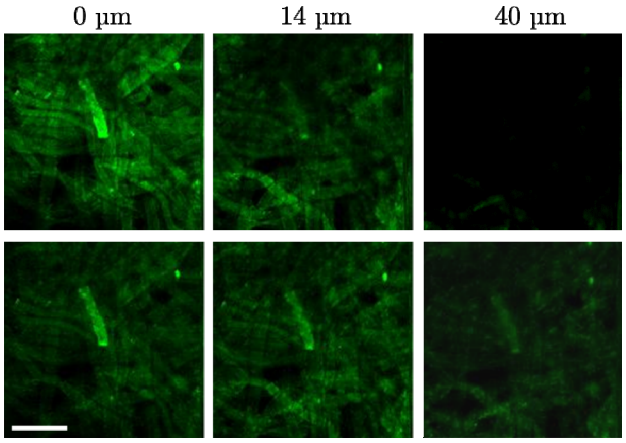

Figure 4.18: TPEF images of different depth locations acquired without (top row) and with induced SA (-0.2 µm, optimum value for this sample). The sample is a human ERM. Scale bar 50 µm.

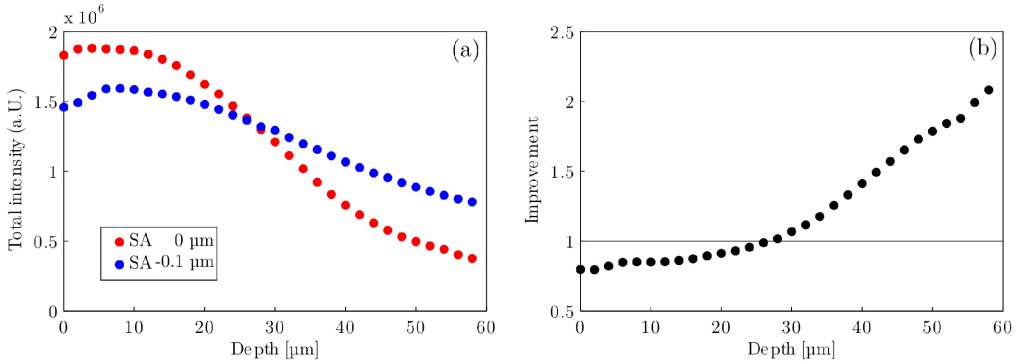

Figure 4.19: (a) Total intensity of the images as a function of depth for two different experimental conditions (red dots: without SA correction; blue dots: with SA correction). (b) Improvement in the total TPEF intensity of the images as a function of depth. Data correspond to the sample in Figure 4.18.

For completeness, the procedure was also applied to samples providing SHG signal (starch grains). For the sample shown in Figure 4.20 a value of -0.1 µm was the SA optimum value. The corresponding total intensity values of the images and the improvement as a function of depth are depicted in Figure 4.21.

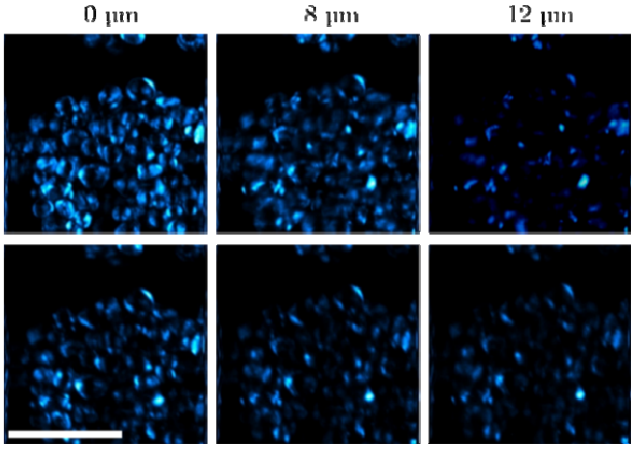

Figure 4.20: SHG images for different depth positions acquired before (top row) and after inducing -0.1 µm of SA (bottom row), which was the optimum value for this sample. The sample is a set of starch grains. Bar length 50 µm.

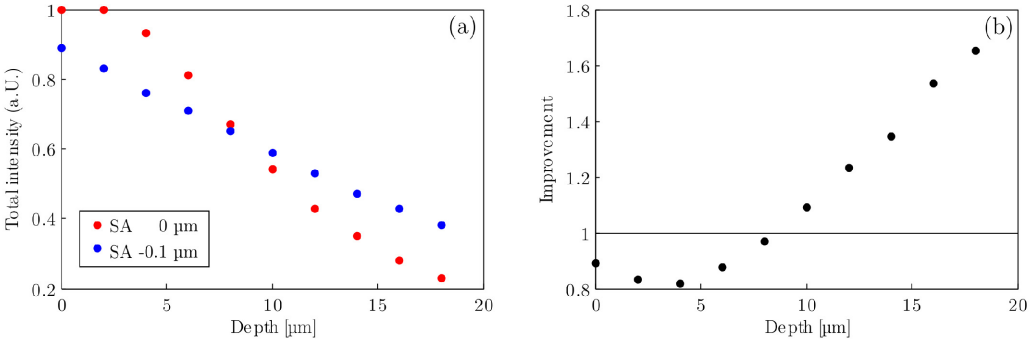

Figure 4.21: (a) Total intensity of the images as a function of depth for two different experimental conditions (red dots: without SA correction; blue dots, with SA correction). (b) Improvement in the total SHG intensity. Sample is that of Figure 4.20.

Finally, the procedure was also applied to another biological sample providing SHG signal (porcine corneal tissue). It is known that within the cornea, the deeper the image plane is located, the lower the SHG signal recorded, as images of the upper panels in Figure 4.22 show. However, when the illumination laser beam contains a certain amount of SA (bottom panels), beyond a particular depth location the intensity levels do not follow that behavior. For this particular sample, -0.1 µm SA was the optimal value to observe the effect analyzed in this work. In Figure 4.23, this improvement in SHG signal as a function of depth is depicted.

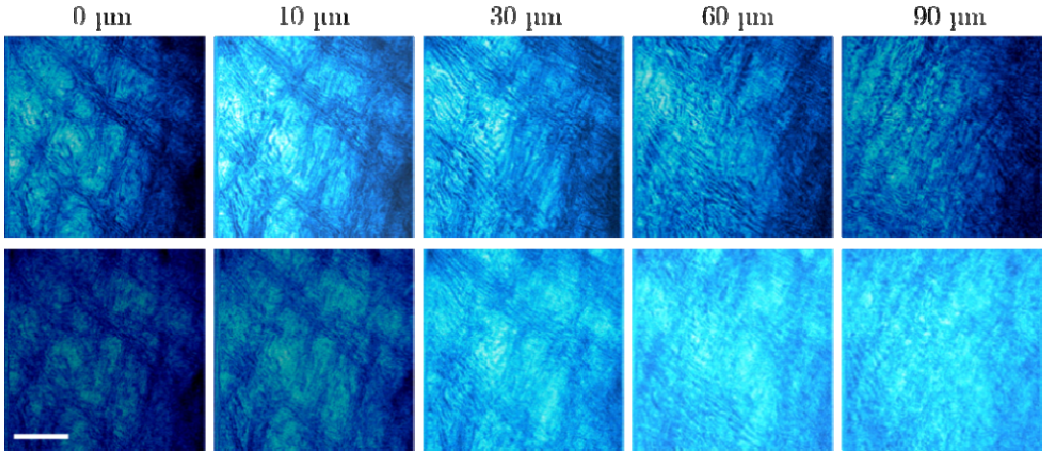

Figure 4.22: SHG imaging of corneal stroma at different depth locations illustrating the effects of adding -0.1 µm SA to the illumination laser beam (bottom panels). Upper panels correspond to the case when all laser beam aberrations were corrected (i.e. no SA added). The sample is an ex-vivo porcine cornea. Bar length: 50 µm.

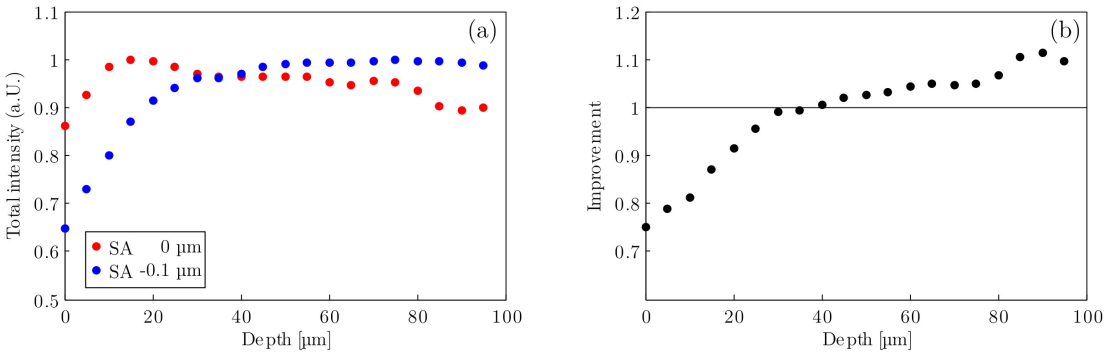

Figure 4.23: (a) Total intensity of the images as a function of depth for two different experimental conditions (red dots: without SA correction; blue dots: with SA correction). (b) Improvement in the SHG intensity of corneal stroma images as a function of depth when inducing -0.1 µm SA with respect to the original images.

4.6. Discussion

During the last decade, there has been a remarkable interest in the development of novel AO capabilities for improved 3D high-resolution MP microscopy imaging. Most reported techniques are sensor-less and improved the focal spot within the sample by pre-shaping the wavefront of the input beam to compensate for the specimen-induced aberration according to a sequential adjust of individual Zernike modes.

In this sense, this study has reported that an accurate manipulation of the aberrations in the illuminating beam provides improved 3D multiphoton imaging. The AO module combining the DM and the HS sensor has not been used for a modal plane-to-plane correction, but to induce controlled amounts of SA, working in closed loop. This manipulation of the incident laser beam aberrations leads to an improvement in the nonlinear signal from images acquired at deeper locations within the sample. This effect might be understood as increased imaging depth or extended DOF and has been demonstrated in samples providing both TPEF and SHG signals.

For each specimen the appropriate SA value was computed from fast tomographic nonlinear imaging (for the experiment the highest induced SA value was -0.3 µm, in steps of 0.05 µm). This value corresponds to the image with the highest area under the intensity profile. With this optimum induced SA, each sample was imaged with depth in a regular manner (XY+Z scanning). Although the required SA values were particular for each sample, they were never larger than -0.2 µm here. The percent of improvement at a certain depth location depended also on the used sample. The shallowest plane at which this improvement takes place was ~7 µm for starch. For the rest of the samples it was placed between 25 and 30 µm.

The effects of SA in both linear (bright-field and confocal) and nonlinear microscopy have been a topic of interest (Sheppard and Wilson, 1979; Hell *et al.*, 1993; Török *et al.*, 1997; Neil *et al.*, 2000; Lo *et al.*, 2005; Muriello and Dunn, 2008). Implementations to eliminate or minimize the effect of SA in the former include an objective correction ring (Booth *et al.*, 2002; Lo *et al.*, 2005; Muriello and Dunn, 2008), changes in the effective tube length of the microscope objective (Sheppard, 1988; Hell *et al.*, 1993), structure illumination techniques (Neil *et al.*, 1997; Arigovindan *et al.*, 2012), point-spread function engineering (Yuan and Preza, 2011) and AO devices (Tsai *et al.*, 2007; Débarre *et al.*, 2009; Shaw *et al.*, 2010; Iwaniuk *et al.*, 2011), among others.

Although to minimize SA some objectives have a correction ring to adjust for the thickness of the microscope slide, additional SA is also present when focusing deeper within the specimen. Moreover, when imaging specimens in a backscattered configuration, the main drawback is the noticeable reduction of the signal at deeper planes. The anterior layers will produce aberrations that might interfere with the measurement from deeper layers as the light travels through. Lo and coworkers analyzed the effect of a collar in MP microscopy of tendon and skin (maximum depth: 28 µm) (Lo *et al.*, 2005). Although their results showed some improvements, they ignored the nominal SA values required for each sample and depth. They also claimed that the collar's ability to compensate for the SA decreased with depth and that the required correction collar settings were particular for each sample and distribution of refraction indices. Muriello and Dunn reported a similar experiment (Muriello and Dunn, 2008). The combination of a water immersion objective lens and a correction collar and a DM to pre-compensate for different aberration terms (SA included) in a mouse embryo (Débarre *et al.*, 2009). This procedure is robust but highly time consuming (minutes).

Despite that aberrations are specimen-dependent, these tend to be dominated by a small number of low-order Zernike aberration modes (see Chapter 3). The magnitude of the aberrations increases with NA (Booth *et al.*, 1998; Schwertner *et al.*, 2004). Although the ideal compensation would require a plane-by-plane SA correction, in the present work, we have demonstrated that this is not always necessary. We report that an appropriate value of SA can experimentally be measured for each sample in

order to improve the image quality of deeper planes because the DOF is extended. This procedure, although with some limitations, represents a more elegant and accurate method than an objective collar, where the effect is limited by the discrete values provided by the collar itself.

Unlike most experiments reported in the literature (using immersion high-NA objectives), the objective here used is a low-NA air long-working distance objective. These "air-immersion" objectives would be more suitable for future in vivo experiments. In this sense, the SA value produced in the illumination beam has a double function: (1) a basal correction compensating for the refractive-index mismatch air-microscope cover and (2) an additional correction to partially compensate for the specimen-induced SA. The reduction of the image quality is affected by SA to a large extent (Booth *et al.*, 1998). Despite that the rest of aberration terms are not corrected and a unique value (experimentally computed) of SA is used, the image quality is improved.

Compared to the experimental conditions using total laser beam aberration correction (Bueno *et al.*, 2010), the "side-effect" of the proposed technique is that the signal at the best imaged plane of the sample is reduced. However, for deeper planes the behavior is reversed, the signal is improved, and more details are visible. Although the enhancement depends on each particular sample, the extended imaging depth has been demonstrated for both TPEF and SHG signals. Moreover, the procedure reported here overpasses (to some extent) the limitation of a single aberration correction per depth (since a unique customized aberration is used) which significantly decreases scan times and enables more rapid imaging. The present approach provides a fine balance on the effect of SA aberrations in stacks of MP images. While SA reduces the image quality at best focus, it provides a better set of images at deeper layers. If the amount of incoming light can be easily selected, this can be a better compromise providing a range of improved images.

The present procedure is much faster than a possible plane-by-plane correction. The typical acquisition time for tomography imaging modality is about 5 s for a 100-µm-thick sample (at 3 µm Z-step). The sequential use of six SA values with the computation of the intensity profiles took approximately 40 s. Once the SA value has been determined, the regular XY imaging (planes taken 5 µm apart) will take ~1 min. The images for a plane-by-plane correction provide better quality, but the time required for this is excessively, what might limit the performance of the procedure when imaging dynamic and/or living samples. In particular, with our experimental configuration, more than 5 minutes would necessary to complete the entire operation.

Probably one of the most interesting consequences is provided by results shown in Figure 4.22. The imaging of corneal tissue in living animals (human included) is a challenging application. Fast recording procedures are of special interest for in vivo applications. The use of the present technique with a non-immersion objective when imaging the living cornea would produce improved images while decreasing acquisition times, minimizing photo bleaching effects, reducing tissue damage, and keeping safety limits (strongly necessary in ophthalmology).

In this chapter we have used an AO MP microscope in a backscattered configuration and a non-immersion low-NA objective to improve 3D nonlinear imaging. The technique was based on an accurate aberration control of the illuminating beam. In particular, controlled amounts of SA led to an increase in imaging depth independently of the specimen-induced aberration, which is essential in MP microscopy. The benefits of this AO procedure have been tested in both non-biological and biological samples, with

particular interest in ex vivo ocular tissues. In this type of tissue, an extended imaging depth might be of huge interest to better visualize deep retinal and corneal layers through volume rendering reconstructions. The procedure here described partially overpasses the limits imposed by the aberrations, improves the MP microscopy sectioning capabilities, and represents a further step to procedure 3D imaging with overall increased quality. This technique might be of great interest in future studies of living samples, especially including corneal tissues.

CHAPTER 5

Effects of pulse compression on multiphoton imaging

Pulse length broadening due to optical dispersion reduces the effectiveness of MP processes. This chapter deals with the effects of a pre-compensation technique by means of a prism-pair pulse compressor device to reduce optical dispersion and to improve MP imaging with special interest in thick ocular tissues. A fast tomographic imaging technique is shown to estimate the optimum compression configuration. Furthermore, a simple method based on laser power reduction is presented to avoid photo-damage in biological samples.

Despite its inherent optical sectioning capabilities, MP imaging at deeper layers within a sample is affected by aberrations and scattering that leads to blurred images with reduced contrast and resolution (as shown in Chapters 3 and 4). Over the last two decades AO has been used to improve MP imaging through the correction of the aberrations of the laser beam, the microscope optics and the specimen aberrations. These implementations only optimize the spatial properties of the beam to get a narrow focal spot. However, temporal properties of the fs laser beam are also of importance since they might also limit the performance of MP processes.

As described in the Introduction of this Thesis, the pulses emitted by a mode-locked laser system present a "broad spectrum", often between 10 and 100 nm. Due to this, different frequency components travel at different speed through the optics of the microscope (lenses, prisms, glass plates, objective,…) and the sample itself (i.e. pulses are affected by dispersion phenomena). Then, the pulses are broadening in time, caused by a phase delay of the frequency components.

When a fs pulse broadens, the peak power is reduced and consequently the non-linear effects. Then, higher average laser power is needed to improve the effectiveness of MP processes. This fact increases the risk of non-controlled thermal side effects and photo-damage that should be avoided especially when imaging biological samples. Instead of increasing the laser power, pulse compression techniques are often used to restore "short laser pulses" and maintain high peak power. Most strategies are based on measuring or estimating the dispersion and apply the opposite so that the total dispersion is zero at the focal plane. This is called pre-compensation (Müller *et al.*, 1998).

The simplest and cheapest way for pulse compression is a set of prisms (Fork *et al.*, 1984), gratings (Treacy, 1969) or chirped mirrors (Szipöcs *et al.*, 1994). Experimental configurations for pre-compensation are usually composed of either four prisms, or two prisms and a mirror. See also Chapter 1 for more information on advantages and disadvantages when using prisms, gratings and mirrors.

Autocorrelation is the most popular method to measure pulse duration (Guild *et al.*, 1997; Müller *et al.*, 1995; 1998). In MP microscopy, another approach of dispersion control includes pulse shapers. A detailed overview was given by (Weiner, 2000; 2011). Normally in a 4-f setup in the Fourier-space a transmission phase modulator is used to introduce phase correcting profiles in the illuminating path of the system. Both SLMs and acusto-optics modulators (Lechleiter *et al.*, 2002) have also been included in pulse shapers when combined with MP microscopy. These devices do not measure dispersion, but they are only able to correct for it.

In this chapter we report on the use of a two-prism pulse compressor introduced in the illumination pathway of our custom MP microscope. Since the fs pulses are broadening between the laser system exit and the microscope entrance, the device will be used for a pre-

compensation operation in order to improve MP imaging. Non-biological and biological thick samples providing both TPEF and SHG signal are involved in the experiment. Special attention was paid to ocular tissue imaging. The combination of pulse compression and MP microscopy might have a big potential for biomedical imaging and may further improve the performance of the MP ophthalmic-oriented instruments.

5.1. Experimental setup

The experimental setup combines a custom-built MP microscope and a two-prism-based pulse compressor. A schematic diagram of the modified experimental setup is shown in Figure 5.1.

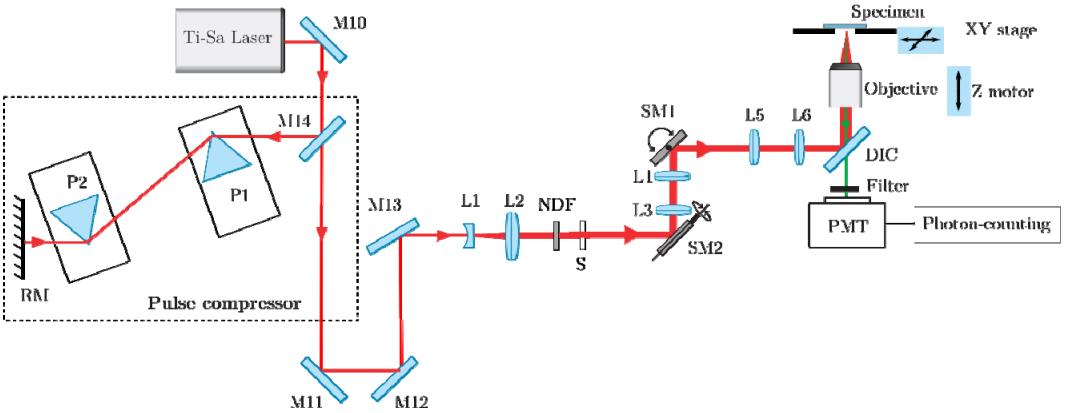

Figure 5.1: Experimental setup combining the MP microscope and the pulse compressor. For simplicity the latter is shown in a simple schematic consisting of a double-pass prism pair (P1 and P2) and a retro-reflector mirror (RM). M10-M14, mirrors; L1-L6, lenses; SM1-SM2, scanning unit; DIC, dichroic mirror; PMT, photomultiplier tube.

The pulse compressor used here (FemtoControl, APE, Berlin, Germany) was introduced in the MP illumination pathway (Figure 5.1). It was used to pre-compensate for the pulse dispersion induced by the microscope optics. The device can be controlled with a simple user interface to adjust the prism positions (for the wavelength used). It is optimized for fs lasers with a spectral range of 680-780 nm. The input polarization has to be horizontal and the additional internal beam path might be up to 1.67 m.

The pulse compressor is composed of two prisms mounted on micro-driven motorized translation stages (Figure 5.2). The prism separation provides an angular dispersion to obtain negative dispersion. The motorized translation of each prism along it symmetry axis allows changing the amount of glass and therefore the amount of induced dispersion. The incident light is reflected by the input mirrors M14 and M15 before passing through the two prisms (P1 and P2). Then it is reflected and vertically displaced down by a retro-reflector mirror (RM). It passes the prisms again and reaches the pick-off mirror M17, situated above M15. Finally, the light beam is reflected by the output mirror M18 and goes to the exit of the pulse compressor. Figure 5.3 shows a picture of the components of the pulse compressor used here.

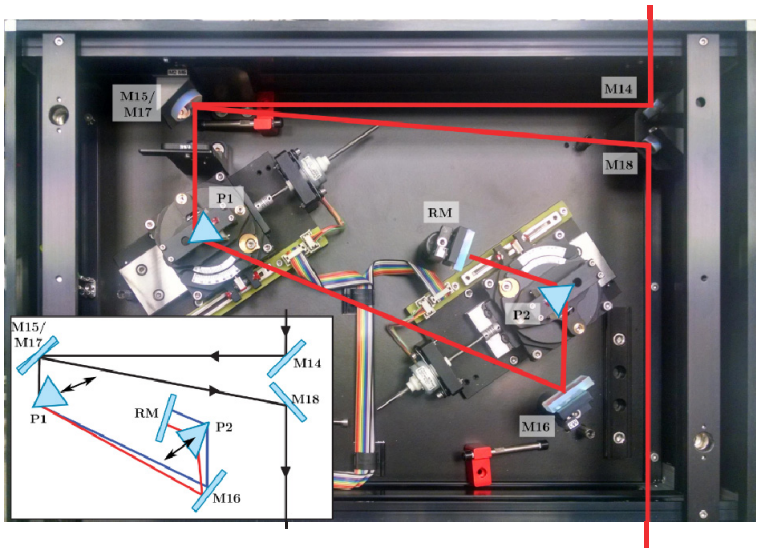

Figure 5.2: Picture and schematic diagram showing the different components of the pulse compressor used in this work. P1 and P2, prisms; M14-M18, mirrors; RM, retro-reflector mirror.

The control panel of the pulse compressor device permits to set the working wavelength and the positions of the two prisms. Four basic pre-programmed settings are available, which are called zero, low, middle and high compression states (PCSs). The basic PCSs were respectively renamed PSC0, PCS4, PCS8 and PCS12. For each wavelength these basic PCSs correlate with the prism positions and the amount of glass the beam has to pass through. However, for a fixed wavelength the position of the prism can be manually set.

First, the pulse compressor was calibrated for the wavelength used (760 nm). Once the wavelength was introduced in the control panel, the positions of the prisms (internal units of the device) for the four basic settings are automatically set by the device. These are plotted in Figure 5.3. A decrease in the prism position is associated with a reduction in the amount of prism glass introduced in the optical path way. Thus, for the PCS0 the light beam passes through the maximum amount of prism glass.

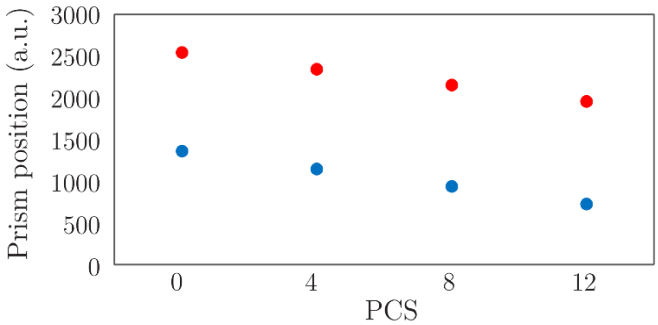

Figure 5.3: Prism positions for the basic PCSs and 760 nm. These are automatically displayed on the control panel of the pulse compressor.

Then, the prism positions corresponding to the basic PCSs were linearly interpolated to get 12 different PCSs, as shown in Figure 5.4.

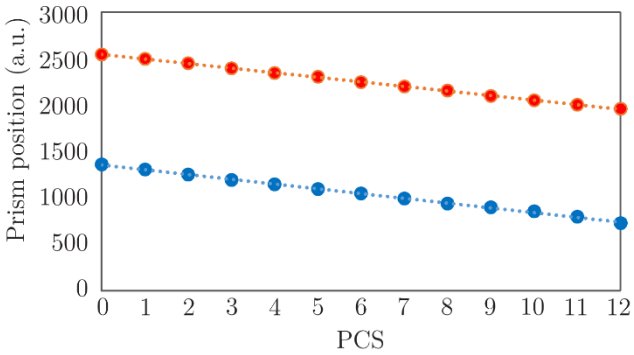

Figure 5.4: Linear interpolation to get 12 different PCSs as a function of the corresponding position of prisms P1 and P2. The prism positions for the PCS0, PCS4, PCS8 and PCS12 correspond to these of the basic settings provided by the manufacturer.

The next step was to measure the actual temporal duration of the laser pulses for each PCS produced by above described device. For this goal a commercially available autocorrelator (Mini, APE, Berlin, Germany) was used. This instrument measures the full-width half maximum (FWHM) of the autocorrelation of the fs-pulses. Along this work this FWHM will be treated as the actual pulse duration.

For the sense of completeness, Figure 5.5 shows the inside of the autocorrelator: a typical interferometric setup in a non-collinear fashion to measure background-free intensity autocorrelation. For calculating the pulse duration from the FWHM of the autocorrelation function a Gaussian shape of the laser pulse was assumed.

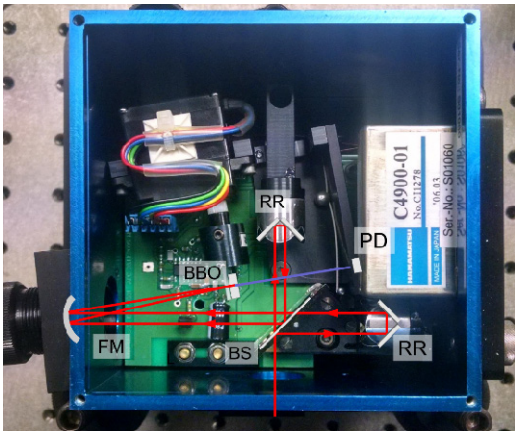

Figure 5.5: Top view of the autocorrelator used in this Thesis. A beam splitter (BS) divides the fs laser beam into two optical arms, directed to a retro-reflector (RR). A focusing mirror (FM) focuses those beams onto a non-linear crystal (BBO). The signal is measured by a photo-detector (PD).

The pulse duration was measured at two different locations in the MP microscope: (A) at the exit of the laser source (pulse state PCS0, used as a reference) and (B) at the entrance of the microscope for all PCSs (from PCS0 to PCS12). This operation permits to investigate the broadening of the pulse duration due to the microscope optics, as well as to estimate the prism configuration providing the minimum pulse duration at the microscope entrance. A schematic of these locations is shown in Figure 5.6.

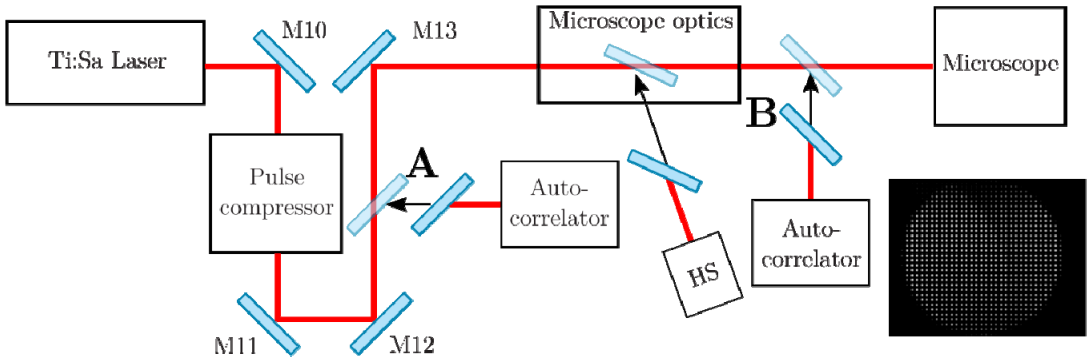

Figure 5.6: Schematic of the locations (A and B) along the optical pathway of the MP microscope where the pulse duration measurements were carried out setup. The location of the HS is also shown.

Additionally, the stability of the laser beam in terms of aberrations was also measured to analyze possible changes induced by the different PCSs. For this, the HS sensor described in Chapter 4 was used. The HS sensor was placed in the experimental system as indicated in Figure 5.6. From each HS image the WA was calculated and expressed in Zernike polynomials up to 5th order for a diameter of 5 mm.

5.2. Imaging acquisition and procedure

The effectiveness of the pre-compensation technique using the pulse compressor was tested in randomly chosen planes within different samples and also for entire thick samples. For the former, a regular XY MP image was acquired for each PCS. The total intensity of each image was calculated and the PCS corresponding to the maximum intensity was chosen as the optimum PCS.

To analyze the effect of sample's depth in the optimum PCS, stacks of different samples were acquired for the entire set of PCSs. Since the action requires high acquisition times, an approach involving tomographic imaging was used. For each sample, a tomographic image was acquired for the each PCSs. From each image the averaged intensity profile as a function of depth was computed. The PCS corresponding to the highest area under this intensity profile was considered as the optimum PCS. Once this optimum PCS was determined, two stacks of regular XY MP images at defined depth locations were recorded, one without pulse compression (i.e. PCS0) and another with the optimum PCS.

5.3. Measurement of the pulse duration: Effect of the pulse compressor

According to the manufacturer the laser pulses emitted by the Ti-Sapphire laser used in this work should have a pulse duration of 200 fs or less. In this sense, this pulse duration was first measured with the autocorrelator placed at the exit of the pulse compressor (point A in Figure 5.6) with the device set to zero (i.e. PCS0). The measured time was 230 fs (red point in Figure 5.7). The autocorrelator was then moved to the microscope entrance (point B in Figure 5.6). As expected, due to the travel of the light beam through the optics of the experimental

setup, the laser pulses were broadened in time up to 400 fs (blue point at PCS0 of Figure 5.6). The PCS was then sequentially changed from PCS0 to PCS12 and, as shown in Figure 5.7, a minimum in the pulse duration of ~150 fs was found for PCS7.

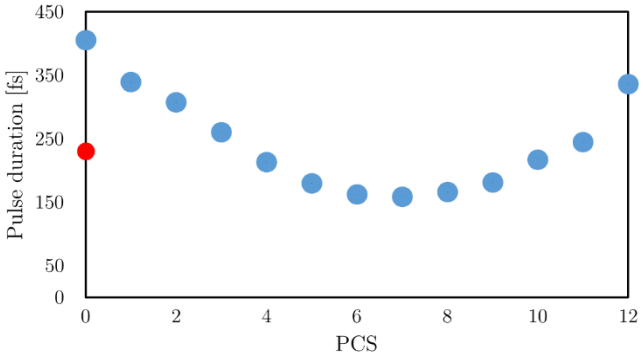

Figure 5.7: Values of pulse duration as a function of the PCSs (see text for details).

5.4. Wavefront aberrations vs. pulse compression

In order to check if changes in the PCSs affect the aberrations of the laser beam, HS images were recorded for all PCS between PCS0 and PCS12. Several WA maps are depicted in Figure 5.8. A visual inspection reveals that the maps are similar for all PCSs. The total RMS ranged between 0.233 and 0.261 µm.

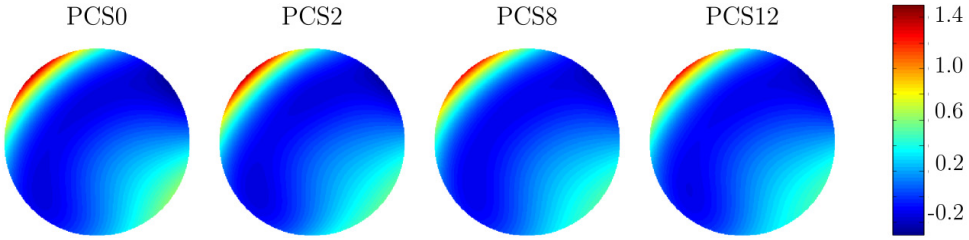

Figure 5.8: WAs corresponding to different PCSs.

The contribution of the individual Zernike terms as a function of the PCS is presented in Figure 5.9 (from 2nd up to 4th order, excluding defocus). It can be seen that the terms hardly change when modifying the PCS. Moreover, astigmatism Z_2^{-2} was found to be the dominant term.

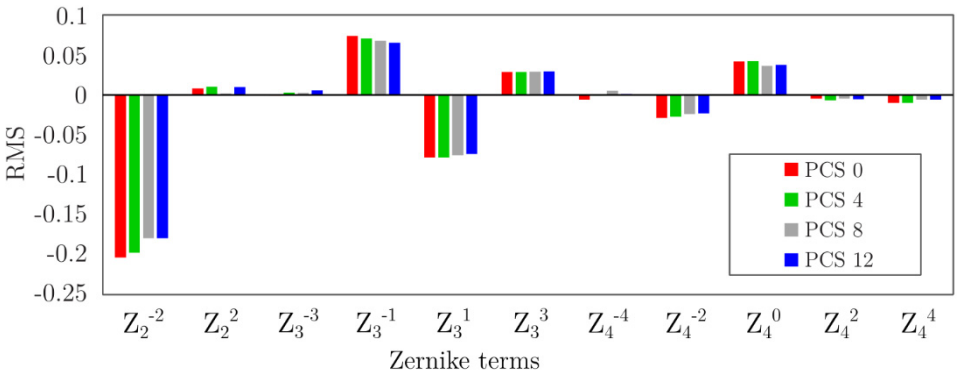

Figure 5.9: Zernike coefficient values of the laser beam WA for different PCSs.

For the sense of completeness Figure 5.10 depicts the WAs for higher order terms (from 3rd to 5th). As expected from Figure 5.8, WAs were also similar across the PCSs, with a mean RMS value of 0.118±0.004 µm.

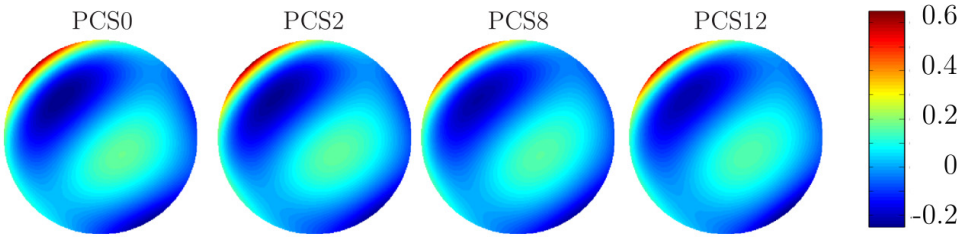

Figure 5.10: High order WAs for the same PCSs as in Figure 5.11.

Figure 5.11 shows the WA RMS values for high order terms as a function of the PCSs. Despite the effects of the pulse compression operation, the RMS values kept stable.

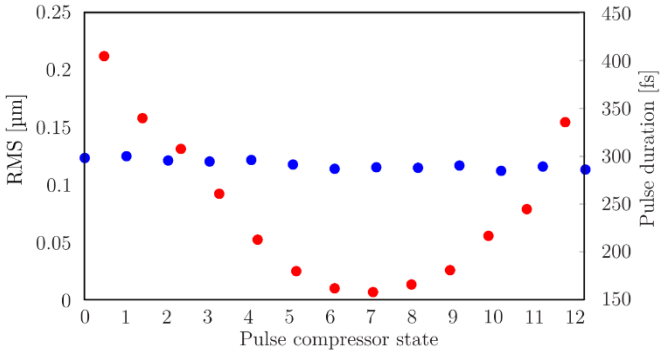

Figure 5.11: Pulse duration (red symbols) and values of RMS of the laser beam WA (blue dots) as a function of the PCS.

To investigate the temporal stability of the WA of the laser beam, short term changes were compared between no pulse compression (PCS0) and the experimental condition providing the shortest pulse duration at the microscope entrance (PCS7). Figure 5.12 shows the short term changes in the Zernike coefficient values. Measurements were done 10 seconds apart during 1 minute. It can be observed that there are hardly changes with time.

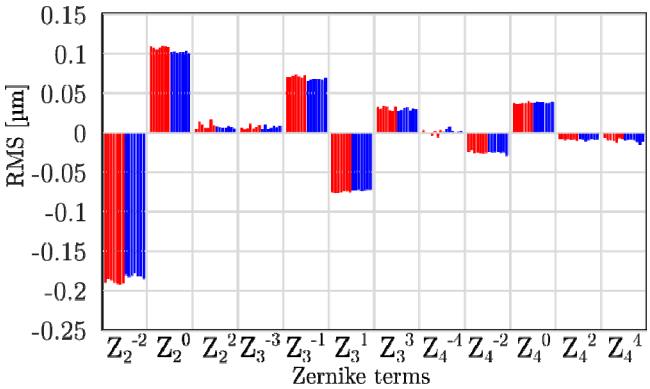

Figure 5.12: Zernike coefficient values as a function of time. Red and blue bars correspond to PCS0 and PCS7 respectively. Each bar represents a measurement done every 10 s along 1 minute.

To analyze this temporal stability more in depth the first HS image (captured at time = 0 s) was used as a reference. For the different PCSs the residual WA was computed as:

$$WA_{residual} = WA_t - WA_{t=0}, \tag{5.1}$$

Figure 5.13 shows graphically the residual WAs associated to the short term changes for PCS0 and PCS7.

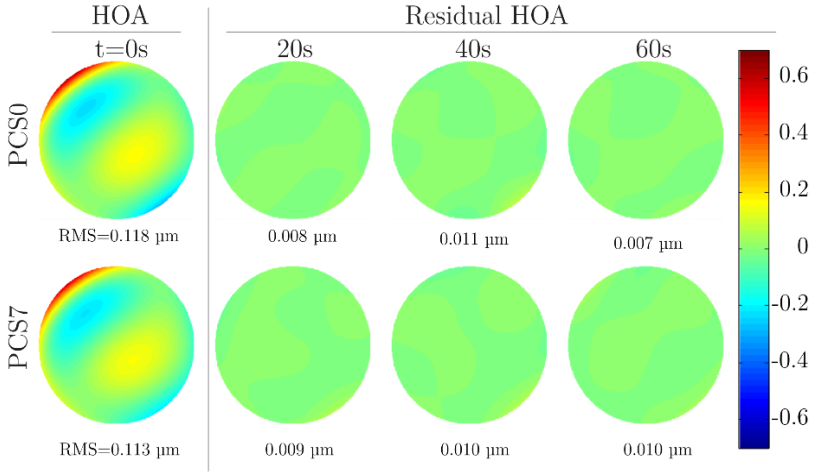

Figure 5.13: Residual WAs as a function of time for two PCSs. The WA acquired for t=0 was used as a reference. HOA, high order aberrations.

5.5. Single plane imaging and pulse compression

Figure 5.14 shows the total intensity values for different samples and non-linear signals as a function of the PCS. The imaged plane within each specimen was randomly chosen.

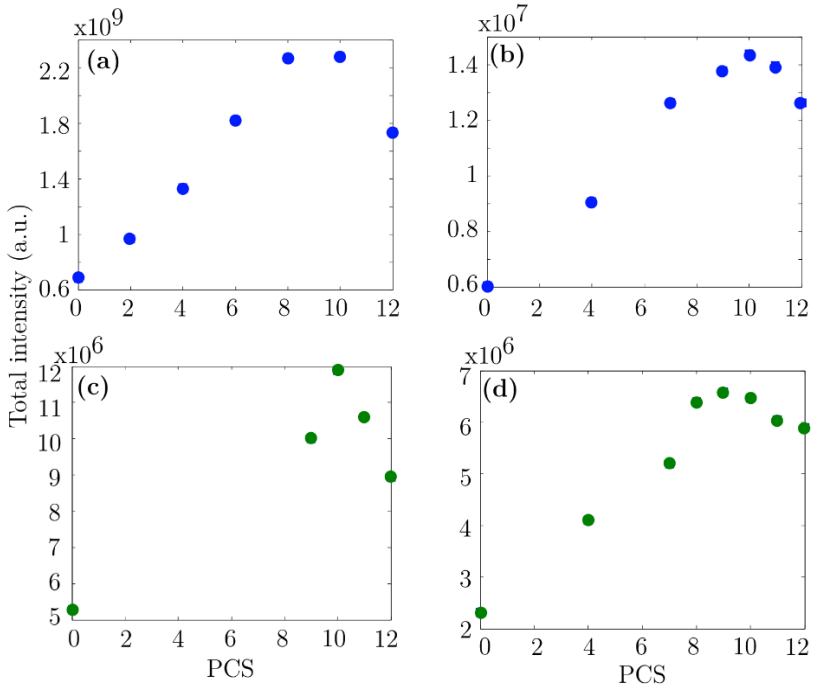

Figure 5.14: Total non-linear intensity (SHG in blue and TPEF in green) as a function of the PCS for a single plane in different samples: ex-vivo pig cornea (a), ex-vivo rabbit cornea (b), ERM (c) and stained human cornea (d).

For all samples the lowest intensity value was found for PCS0 (i.e. no compression). Furthermore, there was always a PCS giving a maximum intensity value. This optimum PCS depended on the imaged sample. These results indicate that the pulse pre-compensation operation maximizes the efficiency of the MP excitation keeping the laser power constant. The improvement ranged between 2- and 3-fold. The corresponding MP images for both PCS0 and that PCS providing the maximum intensity are presented in Figure 5.15.

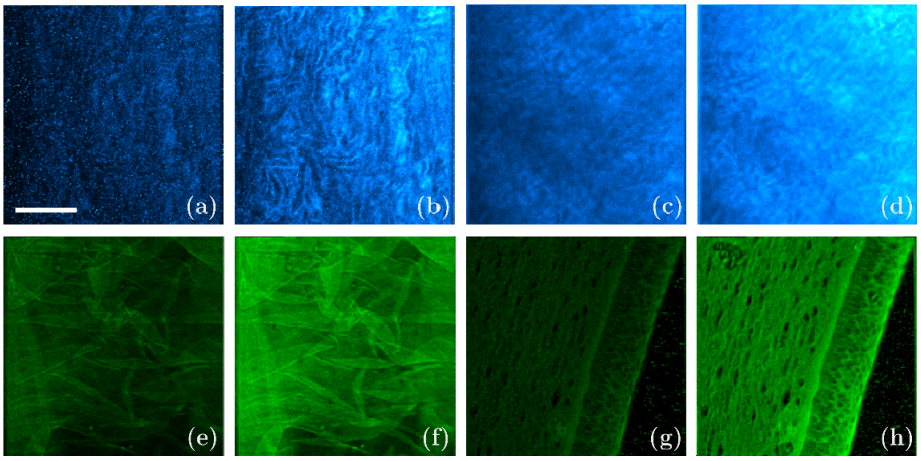

Figure 5.15: Effects of pulse compression on MP images. (a, b) pig cornea, 2.38x improvement; (c, d) rabbit cornea; 2.30x improvement; (e, f) ERM, 2.25x improvement; (g, h) human cornea, 2.83x improvement. All images share the same scale bar (50 μm).

Figure 5.16 illustrates the effectiveness of the pulse compression operation for TPEF and SHG signals in the same specimen (histological sample of a rabbit cornea). For both non-linear signals the PCS leading to the maximum total intensity was the same. The increase in signal was 2x and 1.8x for TPEF and SHG respectively. The corresponding images are shown in Figure 5.17.

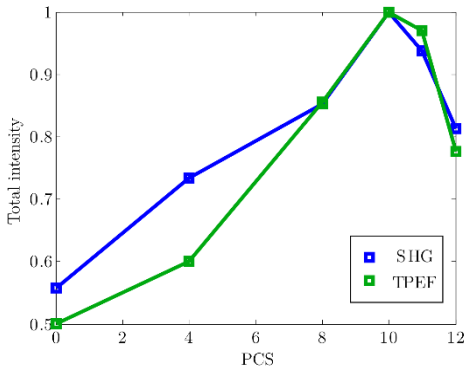

Figure 5.16: Normalized total intensity for SHG and TPEF signals in the same sample as a function of the PCS.

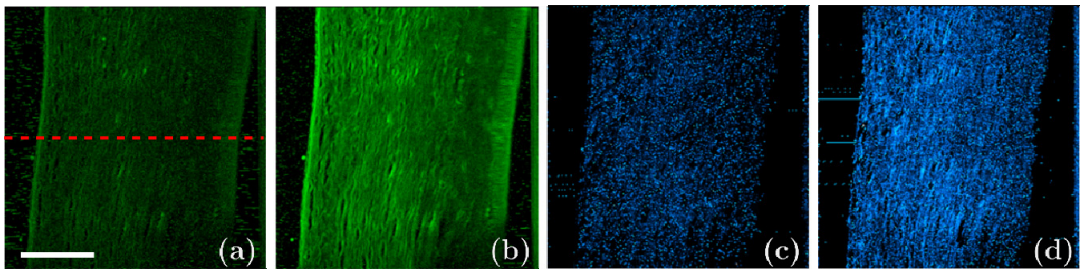

Figure 5.17: Improvement in TPEF (a, b) and SHG (c, d) images of the same specimen. PCS0 (a, c) and PCS10 (b, d). Scale bar: 50 µm. Data along the horizontal dashed line are depicted in Figure 5.20.

The intensity profiles along the horizontal line inserted in Figure 5.17 are shown in Figure 5.18. Since different parts of the cornea provide different non-linear signals, both SHG (stroma) and TPEF (keratocytes, epithelium and endothelium) intensity values are also plot together. This allows distinguishing the different corneal components.

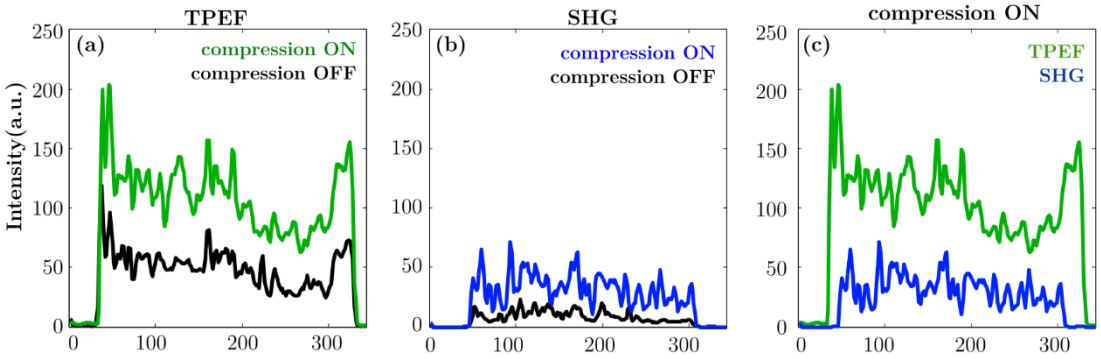

Figure 5.18: Intensity profiles corresponding to the dashed lines in Figure 5.17. (a) TPEF signal with and without pulse compression. (b) SHG signal with and without pulse compression. (c) TPEF and SHG signals with pulse compression.

5.6. Thick samples imaging and pulse compression

The results of the previous section have showed how the MP image of a single plane within a sample can be improved by choosing an optimum PCS. Here different depth locations are optimized as a function of the PCS to analyze possible specimen-induced dispersions.

For a first test an ex-vivo pig cornea was used as specimen. Stacks of images along the corneal thickness (30µm apart) were acquired for different PCS. The corresponding total SHG intensity values are shown in Figure 5.19. Due to the presence of aberrations for each PCS the SHG intensity as a function of depth follows the typical behavior. In addition it can also be observed that for all depth locations the highest total SHG intensity corresponds to the same PCS. For a better understanding Figure 5.20 shows the corresponding SHG images and some additional information.

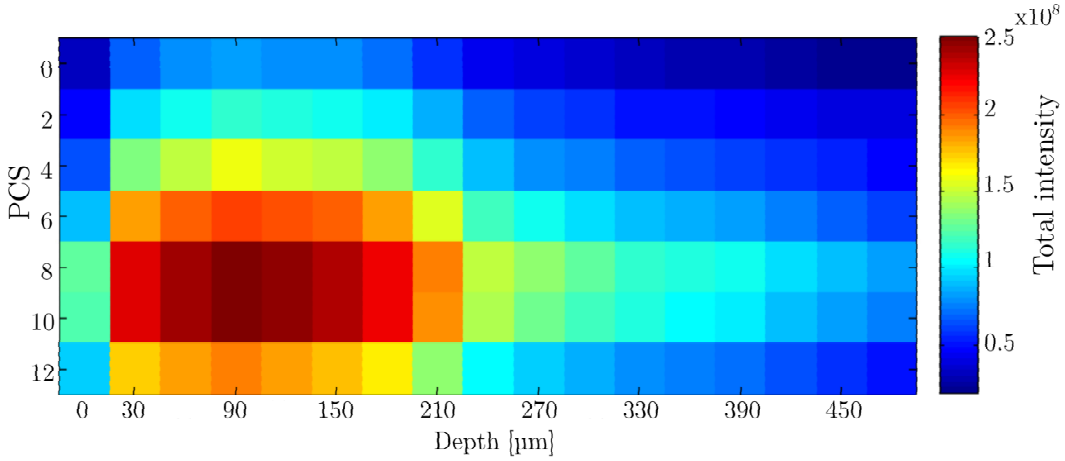

Figure 5.19: SHG intensity map for different depth locations and PCSs.

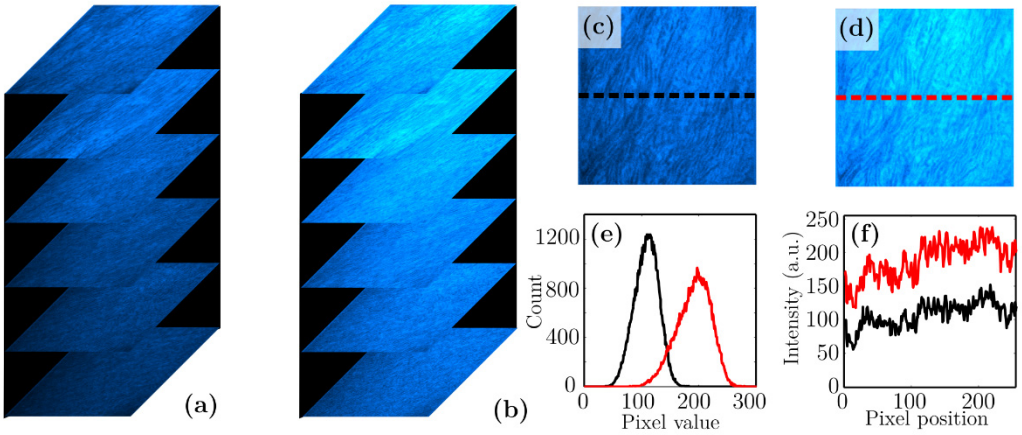

Figure 5.20: SHG image stack without (a) and with (b) pulse compression. Image acquired at 150 µm without (c) and with (d) pulse compression. (e) Histograms corresponding to image (c) and (d) in black and red respectively. (f) Intensity profiles along the horizontal lines inserted in (c) and (d).

5.7. Fast tomographic imaging and pulse compression in thick samples

Since the procedure to optimize the MP imaging of a thick sample through a pulse compression operation is highly time-consuming, another approach is presented in the following. This based on using fast tomographic imaging in a similar way to that presented in Chapter 4. In the present experiment a tomographic image was acquired for every PCS. An example is presented in Figure 5.21.

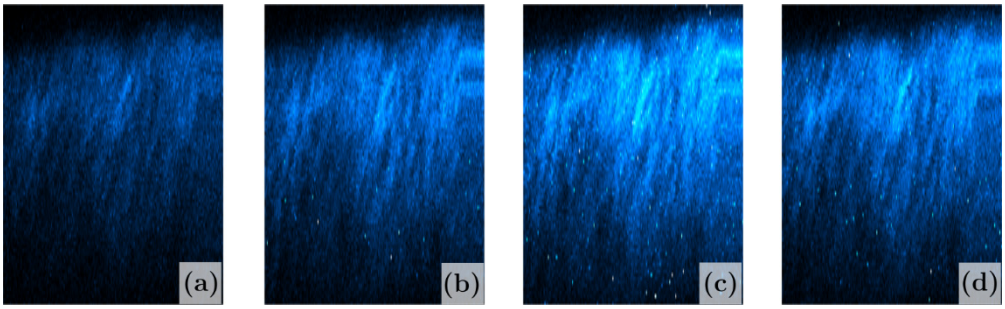

Figure 5.21: SHG tomographic images for PCS0 (a), PCS4 (b), PCS9 (c), and PCS12 (d). The sample is a rabbit cornea.

From each PCS the averaged intensity profile with depth was automatically computed. For three different samples Figure 5.22 shows some of these intensity profiles. Then, the area under the curves for each PCS was computed. The optimal PCS corresponds to the curve providing the largest area (red lines in Figure 5.22). The values of those areas for the different samples and each PCS are depicted in Figure 5.23.

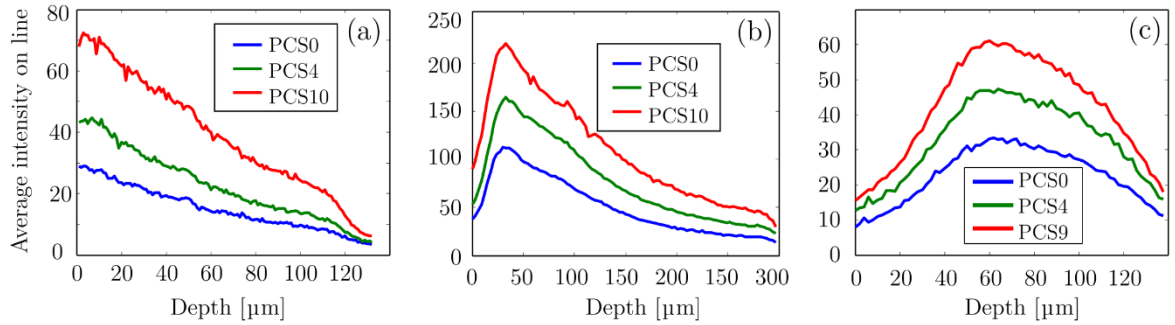

Figure 5.22: Depth intensity profiles computed from tomographic images for different PCSs and samples providing SHG (a, b) and TPEF (c) signals. Samples correspond to human cornea (a), chicken cornea (b) and rat retina (f).

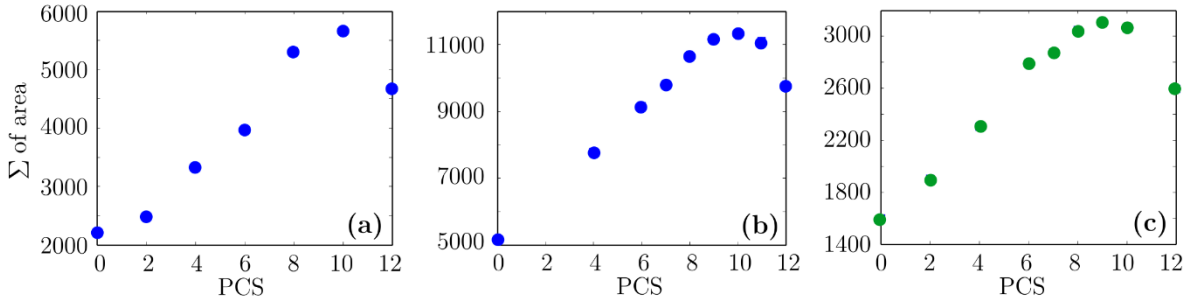

Figure 5.23: Total area under the intensity profile curves as a function of the PCS computed from the curves in Figure 5.24.

For each sample a unique PCS was required to optimize the entire sample. These usually ranged between PCS9 and PCS11. As an example Figure 5.24 compares the tomographic images without pulse compression (PCS0) and with the optimal PCS for the same samples as in previous figures. The improvement for each image is easily observed.

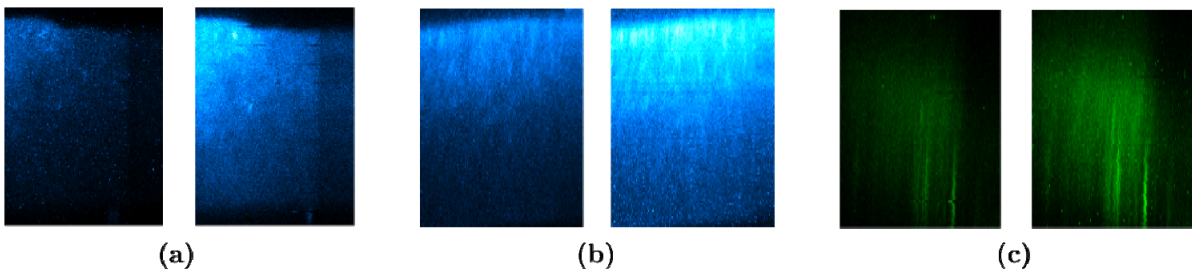

Figure 5.24: Pairs of tomographic images comparing PCS0 and the optimum PCS. Images correspond to samples of Figure 5.24. The improvements in signal were respectively 2.56x, 2.17x and 2.00x.

Once the optimum PCS was determined through this approach based on fast tomographic imaging, stacks of regular (XY+Z) MP images were acquired without pulse compression and with the optimum PCS. Figure 5.25 shows these results in a rabbit cornea. Plots at the bottom are the associated histograms. These histograms facilitate the understanding of the effects of using pulse compression to optimize MP imaging. For every imaged plane the corresponding histogram moves to the right and spreads.

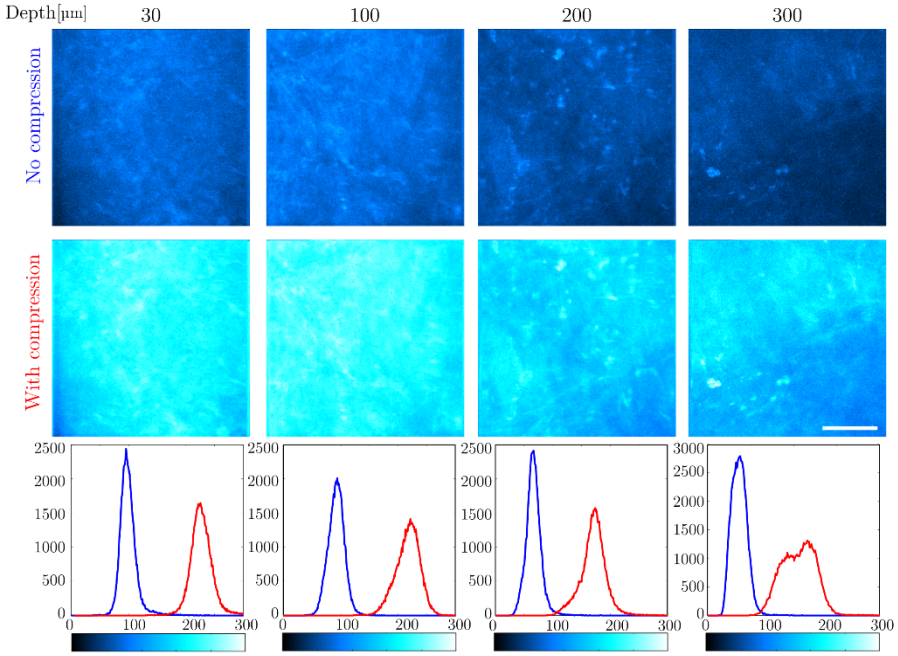

Figure 5.25: Improvement of SHG images at different depth locations in a rabbit cornea using pulse compression. Associated histograms are presented at the bottom row (PCS0, blue; optimum PCS red). Bar length: 50 µm.

For completeness Figure 5.26 shows the mean SHG intensity values for each depth location together with the corresponding plane-to-plane improvement. This enhancement (green symbols) was maintained with depth (averaged value 1.62±0.13).

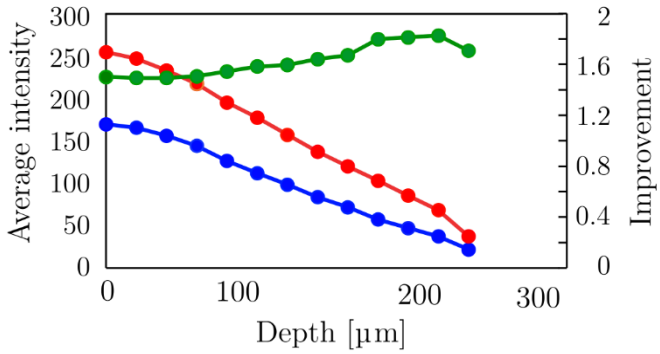

Figure 5.26: Comparison of SHG intensity values before (blue) and after (red) pulse compression as a function of depth. Green data represent the plane-by-plane improvement.

The procedure was also testes in more samples. Figure 5.27 shows the results at a layer located at 100 µm within a human cornea and a chicken cornea. For the former the average improvement when using the optimum PCS was 2.5±0.2, and the histogram increased a factor

of 1.69±0.28. For the latter there was an overall total intensity improvement of 2.0±0.1, and the histogram enhancement was 1.41±0.32.

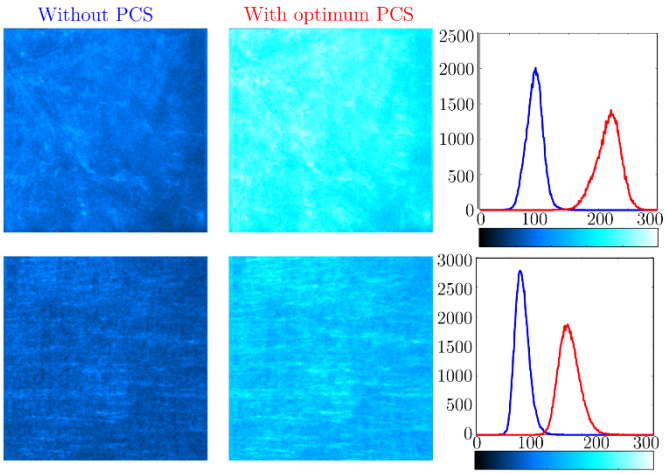

Figure 5.27: SHG imaging enhancement when using the optimum PCS. Samples correspond to a human (upper panels) and a chicken cornea (bottom panels) at depth locations of 100 μm. Image size: 180x180 μm^2.

The procedure was also applied to thick samples providing TPEF signal. Figure 5.28 shows the corresponding results in a piece of cellulose. Here the average improvement in total intensity was 1.42±0.21 (1.14±0.16 for the histograms).

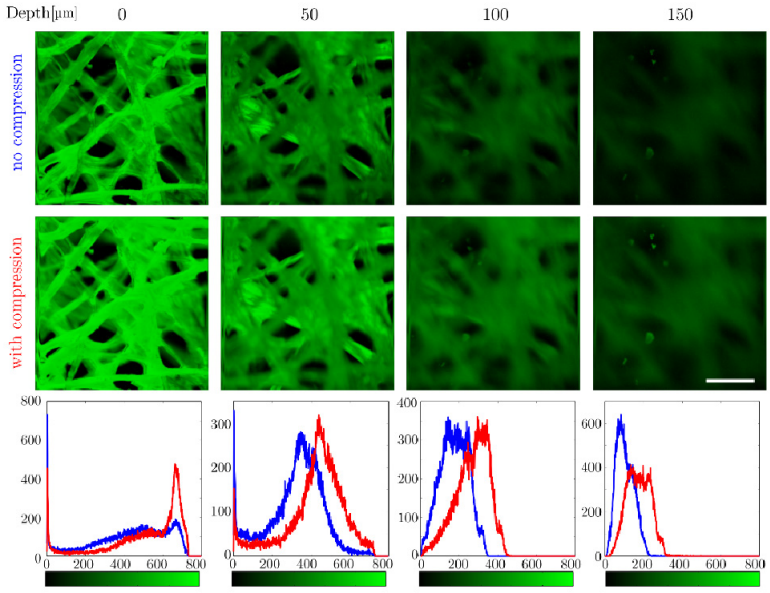

Figure 5.28: TPEF signal enhancement for different depth locations in a piece of cellulose when using pulse compression. The labels are the same as those in previous figures. Bar length: 50 μm.

For completeness, results for two additional TPEF samples are depicted in Figure 5.29 (an ERM and a rat retina). The average improvement values when using the optimum PCS were respectively 2.43±0.18 and 1.81±0.33 (2.00±0.23 and 1.51±0.15 for the histograms).

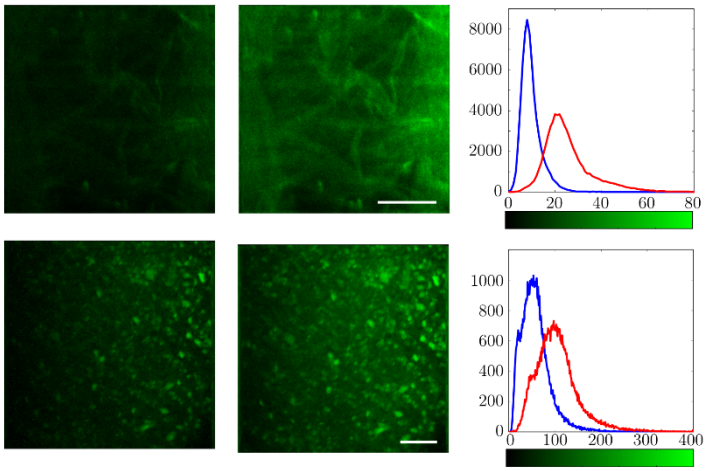

Figure 5.29: TPEF imaging enhancement when using the optimum PCS. Samples correspond to an ERM (upper panels) and a rat retina (bottom panels) at depth location of 20 μm. Bar length: 50 μm.

5.8. Reduced photo-damage using pulse compression in thick samples

The last part of the experiment was centered on analyzing the combined effects of pulse compression and the reduction of laser power. In previous sections it has been shown that the pulse compression operation optimizes MP processes and provides images with higher signal levels.

Despite the image improvement at deeper layers, sometimes higher laser power levels are required in order to get images with enough signal to visualize some details and features in the imaged area. If these power levels are maintained constant when imaging shallow layers, non-controlled (and often non-reversible) photo-damage or photo-toxicity side effects might occur in the sample. In that sense the question now would be: how much can the laser power be reduced when using pulse compression to get MP images with acceptable quality avoided possible photo-damage effects?

To answer this question MP images were recorded with the optimum PCS at different laser power levels and they were compared to the MP image acquired without pulse compression (i.e. PCS0). The results corresponding to a sample providing TPEF signal (a mouse retina) are depicted in Figure 5.30. The left plot depicts the total TPEF intensity for images acquired with the optimum PCS at different laser power values and without pulse compression. For a better understanding, some of the TPEF images labeled in the plot (A, B, C and D) are shown in Figure 5.30(b). Image A corresponds to PCS0 and the pre-defined laser power (red symbol). When the best PCS is used, the TPEF signal effectiveness noticeable increases and image D is acquired. Then, with this optimum PCS the laser power was progressively reduced (blue symbols). This leads to a reduction of TPEF intensity. The acquired images B and C are representative of this. In particular, compared to image A, image C presents similar intensity values although this latter was acquired with less laser power. The corresponding histograms of these TPEF images are presented at the right bottom for a direct

comparison. For the sense of completeness, the results for SHG images (of a porcine cornea) are presented Figure 5.31. A similar behavior can be observed.

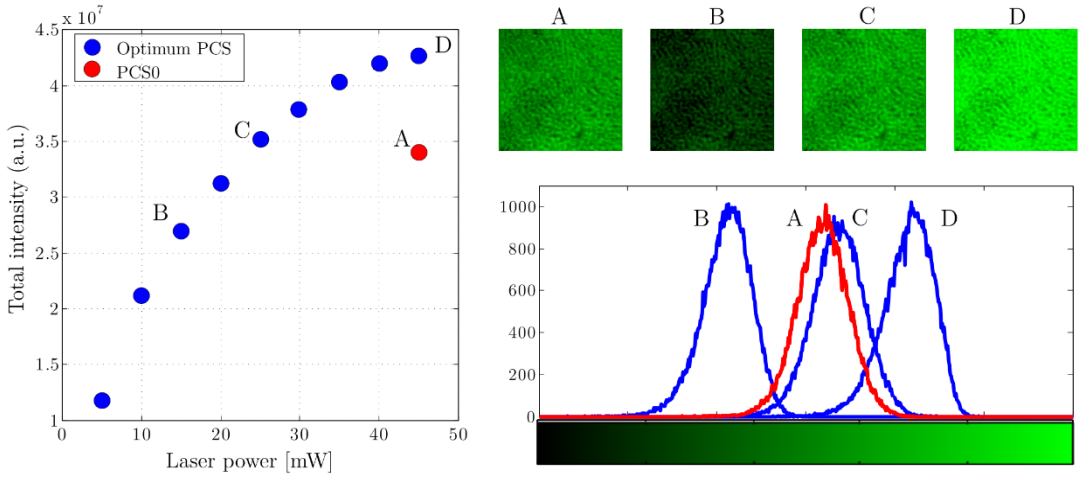

Figure 5.30: Effects in total TPEF signal when combining pulse compression effects and laser power reduction (a). As a common reference, the laser power was always measured at a location in front of the scanning unit. TPEF images (b) and corresponding histograms for different experimental conditions (c). See text for further details.

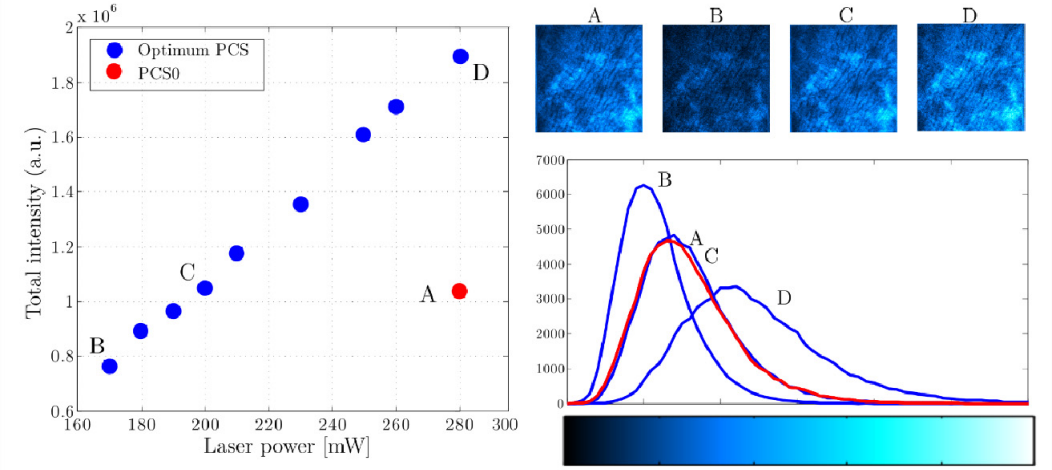

Figure 5.31: SHG total intensity with the optimum PSC as a function of laser power (blue symbols). The red symbols corresponds to the original SHG image acquired without pulse compression. (b) SHG images labeled in (a); (c) histograms of images in (b).

5.9. Discussion

Despite its well-known intrinsic properties of optical sectioning and three dimensional imaging of MP microscopy, these are limited by aberrations (see previous chapters) and dispersion effects. As already stated, system and sample-induced aberrations can be corrected by AO, what enhances MP effectiveness.

On the other hand, optical dispersion produced by the refractive elements of the microscope broadens the temporal pulse length. The peak power is then reduced and also the effectiveness of the MP processes. As a consequence, higher laser power is needed to increase the generation of non-linear signal in order to get better (brighter) images. For example, an 2-fold increase of pulse duration would require a power increase of 1.4-fold (Zipfel *et al.*, 2003).

However, this might produce unwanted side effects on the sample (photo-damage, photo-toxicity,…) that should be avoided especially when imaging biological samples.

In this Chapter 5, a research MP microscope has been modified to include a 2 prism pulse compressor (optimized for infrared light) to manipulate the duration of the incident fs-laser pulses and control the phase dispersion of its frequency components. The capabilities of the pulse compressor have been explored in order to improve MP images, especially at deeper locations within the sample. It has also been investigated how much the laser power can be reduced to get good quality images while using pulse compressor techniques.

Different pulse compression techniques have been developed over the last decades. They mainly included prisms (Fork *et al.*, 1984) and diffraction gratings (Treacy, 1969) to introduce an amount of negative dispersion to compensate for the positive dispersion induced by the microscope optics. For MP applications prisms (are those used here) are more interesting than gratings since they present lower light losses.

A MP microscope containing a grating-based pulse compressor was demonstrated by Liang and co-workers (Liang *et al.*, 2010). They were able to reduce the pulse duration at the focal plane from 190 to 38.7 fs (nominal laser value=100 fs). Raja *et al.* used a 2-prism pulse compressor to improve the SHG signal of collagen samples (liver, collagen gel, muscle) acquired with a fs-laser of 900 nm (Raja *et al.*, 2010). They optimized the pulse duration measured at the sample plane from 215 to 96 fs.

It was shown how a pulse duration of 400 fs at the microscope entrance was reduced down to 150 fs. For the present experiment it was not necessary to know the exact pulse duration at the sample's plane since the optimization of the MP image was sequentially obtained for each sample (and depth) using the experimental conditions PCS0, PSC2,... It is important to notice that the WA of the laser beam did not change with the different PCSs, what indicates that changes in MP image quality are exclusively due to the PCS configuration.

Randomly chosen single planes of different samples were firstly improved. For all of them, a PCS of >7 was necessary. For samples providing both TPEF and SHG signals, the optimum PCS was the same. With this PCS, the acquired MP images presented higher intensity levels, as well as higher contrast. These results are in good agreement with the results obtained by others (Raja *et al.*, 2010), which also show brighter and sharper SHG images as well as a marked improvement and a better visualization of certain details (collagen fibres) within the samples. In particular, total intensity improvements higher that 1.8x were found here. This fairly agrees with previous ones (in the range 2x-3x for different biological samples) from other scientists (Raja *et al.*, 2010).

Improvement values are clearly smaller than those reported by Xi and collaborators (Xi *et al.*, 2009). They claimed to reach a 6-to-11 fold improvement in TPEF signal from cells and tissues, and up to 19-fold improvement in SHG images of a rat tendon specimen. These data might be due to the fact that they worked with sub-20-fs laser pulses. Very short pulse

durations could be more efficient to generate non-linear signals, but they are also more prone to have more non-controlled dispersion effects than conventional fs-laser pulses in the range 80-100fs.

Previous publications on MP image improvement through pulse compression dealt with single plane imaging and results on thick samples have not been found. In this sense, the performance of the procedure used for individual planes was also tested in thick samples (see Figures 5.21 and 5.22). A plane-by-plane searching of the PCS giving the maximum intensity was done. Results show that optimum PCS was the same for all the planes within the sample. This means that the sample itself has little influence on pulse broadening and that most of these effects are due to the microscope optics.

In view of this and since this approach was highly time consuming, an alternative one was used. This was based on computing the appropriate PCS for the entire sample from fast tomographic images. The optimum PCS corresponds to the tomographic image with the highest area under the intensity profile. Once the best PCS was determined, each sample was imaged with depth in a regular manner (i.e. XY images along the Z direction). Although the PCS was particular for each sample, is always ranged between PCS9 and PCS11. The improvement at a certain depth location depended also on the used sample but it was never smaller than 40% for the samples here used. This demonstrates that pulse compression is also able to improve images from deeper layers what is highly interesting because of the noticeable signal reduction at those locations.

Finally, it has been shown the benefit of using pulse compression to minimize damage in biological tissues. With the pulse compression in operation, the incident laser power was reduced until an image similar to that obtained without pulse compression was obtained. Results indicate that the laser power could be reduced up to 50% for both, TPEF and SHG signals. This is extremely important when imaging living specimens, where excessive exposure to light might put the sample under risk suffering not reversible photo-damage.

Pulse compression using a 2-prism configuration has been shown to be a useful tool to increase the efficiency of MP processes and enhance the quality of both TPEF and SHG images. In particular, an accurate determination of the optimum PCS led to a significant improvement in MP imaging independently on the thickness of the studied sample. The benefits of this procedure in order to reduce non-controlled photo-damage in biological samples have also been analyzed. Since aberrations and chromatic dispersion are two independent physical phenomena, the combination of pulse compression and AO into MP microscopy has a big potential for biomedical imaging. This may even help to improve the performance of the ophthalmic-imaging MP-based devices.

CHAPTER 6

CONCLUSIONS

The aim of this work has been to optimize the MP imaging performance by means of both AO and pulse compression operations. The presented methods were evaluated in a number of samples, with special interest in ocular tissues. The main conclusions of this Doctoral Thesis are summarized in the following.

1. A custom-built MP microscope including an LCoS-SLM in the illumination pathway has been used to correct for plane-by-plane specimen-induced aberrations. A WFSL-AO technique based on a deterministic hill-climbing algorithm has been developed for this purpose. Despite using a low-NA air objective and a microscope configuration in backscattered mode, the procedure provided significant improved images at different depth locations for both TPEF and SHG signals.

2. Although the AO correction was particular for each sample, the amount of aberration linearly increased with depth. Moreover, the WA optimizing the MP image at a particular location was not dependent on the field-of-view. However, this may depend on the specimen structure and imaged depth location.

3. The combination of Zernike modes optimizing the MP image depended on the correction control sequence. The hill-climbing algorithm was effective for both increasing and decreasing directions. Despite the optimum WA maps differed, the final enhanced images were similar.

4. SA was found to be the dominant aberration term, especially at deeper locations within the samples. The correction of this term itself provides improved MP images of similar quality to those including the correction of other terms such as coma and astigmatism.

5. An alternative AO module composed of a HS sensor and a DM mirror was used to manipulate the SA pattern of the incident beam in order to increase the DOF.

6. A unique SA pattern was determined via a fast tomography imaging technique to avoid plane-by-plane corrections. While controlled amounts of SA reduced the image quality of shallow planes, these also led to better images at deeper layers, independently of the specimen-induced aberrations.

7. A variable pulse compressor was used to pre-compensate the dispersion of the laser pulses produced by the microscope optics and the sample. This operation increased the effectiveness of the MP processes and then the total TPEF and SHG signal up to a factor larger than 2x.

8. The PCS providing the best image was particular for each sample but kept constant with depth location.

9. This pulse compensation operation also allowed reducing the laser power use for MP imaging and minimize photo-damage effects. This is extremely important in biological samples. Results show that the use of an optimum PCS permits a decrease of about 50% in laser power.

REFERENCES

Albert, O., Sherman, L., Mourou, G., Norris, T.B., and Vdovin, G. (2000) Smart microscope: an adaptive optics learning system for aberration correction in multiphoton confocal microscopy. *Opt. Lett.* **25**: 52–54.

Aptel, F., Olivier, N., Deniset-Besseau, A., Legeais, J.-M., Plamann, K., Schanne-Klein, M.-C., and Beaurepaire, E. (2010) Multimodal nonlinear imaging of the human cornea. *Invest. Ophthalmol. Vis. Sci.* **51**: 2459–2465.

Arigovindan, M., Sedat, J.W., and Agard, D.A. (2012) Effect of depth dependent spherical aberrations in 3D structured illumination microscopy. *Opt. Express* **20**: 6527–6541.

Aviles-Espinosa, R., Olarte, O.E., Porcar-Guezenec, R., Levecq, X., Artigas, D., Nieto, M., et al. (2011) Measurement and correction of in vivo sample aberrations employing a nonlinear guide-star in two-photon excited fluorescence microscopy. *Biomed. Opt. Express* **2**: 3135.

Azucena, O., Crest, J., Cao, J., Sullivan, W., Kner, P., Gavel, D., et al. (2010) Wavefront aberration measurements and corrections through thick tissue using fluorescent microsphere reference beacons. *Opt. Express* **18**: 17521.

Bewersdorf, J., Pick, R., and Hell, S.W. (1998) Multifocal multiphoton microscopy. *Opt. Lett.* **23**: 655–657.

Bonora, S. and Zawadzki, R.J. (2013) Wavefront sensorless modal deformable mirror correction in adaptive optics: optical coherence tomography. *Opt. Lett.* **38**: 4801–4804.

Booth, M.J., Neil, M.A.A., and Wilson, T. (1998) Aberration correction for confocal imaging in refractive-index-mismatched media. *J. Microsc.* **192**: 90–98.

Booth, M.J. and Wilson, T. (2001) Refractive-index-mismatch induced aberrations in single-photon and two-photon microscopy and the use of aberration correction. *J. Biomed. Opt.* **6**: 266–272.

Booth, M.J., Neil, M.A.A., Juškaitis, R., and Wilson, T. (2002) Adaptive aberration correction in a confocal microscope. *Proc. Natl. Acad. Sci.* **99**: 5788–5792.

Booth, M.J. (2004) Wave front sensorless adaptive optics, modal wave front sensing, and sphere packings. In, *Proc. of SPIE Vol.*, p. 151.

Booth, M.J. (2006) Wave front sensor-less adaptive optics: a model-based approach using sphere packings. *Opt. Express* **14**: 1339–1352.

Booth, M.J. (2007) Adaptive optics in microscopy. *Philos. Trans. R. Soc. A Math. Phys. Eng. Sci.* **365**: 2829–2843.

Botcherby, E.J., Juškaitis, R., and Wilson, T. (2006) Scanning two photon fluorescence microscopy with extended depth of field. *Opt. Commun.* **268**: 253–260.

Bueno, J.M. and Artal, P. (2001) Polarization and retinal image quality estimates in the human eye. *JOSA A* **18**: 489–496.

Bueno, J.M., Berrio, E., and Artal, P. (2006) Corneal polarimetry after LASIK refractive surgery. *J. Biomed. Opt.* **11**: 14001.

Bueno, J.M., Vohnsen, B., Roso, L., and Artal, P. (2009) Temporal wavefront stability of an ultrafast high-power laser beam. *Appl. Opt.* **48**: 770–777.

Bueno, J.M., Gualda, E.J., and Artal, P. (2010) Adaptive optics multiphoton microscopy to study ex vivo ocular tissues. *J. Biomed. Opt.* **15**: 66004.

Bueno, J.M., Giakoumaki, A., Gualda, E.J., Schaeffel, F., and Artal, P. (2011a) Analysis of the chicken retina with an adaptive optics multiphoton microscope. *Biomed. Opt. Express* **2**: 1637.

Bueno, J.M., Gualda, E.J., and Artal, P. (2011b) Analysis of corneal stroma organization with wavefront optimized nonlinear microscopy. *Cornea* **30**: 692–701.

Bueno, J.M., Skorsetz, M., Palacios, R., Gualda, E.J., and Artal, P. (2014) Multiphoton imaging microscopy at deeper layers with adaptive optics control of spherical aberration. *J. Biomed. Opt.* **19**: 11007.

Campagnola, P.J., Lewis, A., Loew, L.M., Clark, H.A., and Mohler, W.A. (2001) Second-harmonic imaging microscopy of living cells. *J. Biomed. Opt.* **6**: 277–286.

Cha, J.W., Ballesta, J., and So, P.T.C. (2010) Shack-Hartmann wavefront-sensor-based adaptive optics system for multiphoton microscopy. *J. Biomed. Opt.* **15**: 46022.

Cox, G. (2002) Biological confocal microscopy. *Mater. Today* **5**: 34–41.

Cristóbal, G., Schelkens, P., and Thienpont, H. (2011) Optical and Digital Image Processing.

David, V., Krueger, A., and Feru, P. (2007) Dispersion compensation sharpens multiphoton microscopy. *Laser Focus world* **43**: 117.

Débarre, D., Booth, M.J., and Wilson, T. (2007) Image based adaptive optics through optimisation of low spatial frequencies. *Opt. Express* **15**: 8176–8190.

Débarre, D., Botcherby, E.J., Watanabe, T., Srinivas, S., Booth, M.J., and Wilson, T. (2009) Image-based adaptive optics for two-photon microscopy. *Opt. Lett.* **34**: 2495–2497.

DeLong, K.W., Trebino, R., Hunter, J., and White, W.E. (1994) Frequency-resolved optical gating with the use of second-harmonic generation. *JOSA B* **11**: 2206–2215.

Denk, W., Strickler, J.H., and Webb, W.W. (1990) Two-photon laser scanning fluorescence microscopy. *Science (80-.).* **248**: 73–76.

Dorrer, C., De Beauvoir, B., Le Blanc, C., Ranc, S., Rousseau, J.-P., Rousseau, P., et al. (1999) Single-shot real-time characterization of chirped-pulse amplification systems by spectral phase interferometry for direct electric-field reconstruction. *Opt. Lett.* **24**: 1644–1646.

Dufour, P., Piché, M., De Koninck, Y., and McCarthy, N. (2006) Two-photon excitation fluorescence microscopy with a high depth of field using an axicon. *Appl. Opt.* **45**: 9246–9252.

Fahrbach, F.O., Gurchenkov, V., Alessandri, K., Nassoy, P., and Rohrbach, A. (2013) Light-sheet microscopy in thick media using scanned Bessel beams and two-photon fluorescence excitation. *Opt. Express* **21**: 13824–13839.

Fermann, M.E., Galvanauskas, A., and Sucha, G. (2002) Ultrafast lasers: Technology and applications CRC Press.

Fernández, E.J., Prieto, P.M., and Artal, P. (2009) Wave-aberration control with a liquid crystal on silicon (LCOS) spatial phase modulator. *Opt. Express* **17**: 11013–11025.

Fork, R.L., Martinez, O.E., and Gordon, J.P. (1984) Negative dispersion using pairs of prisms. *Opt. Lett.* **9**: 150–152.

Gallmann, L., Sutter, D.H., Matuschek, N., Steinmeyer, G., Keller, U., Iaconis, C., and Walmsley, I.A. (1999) Characterization of sub-6-fs optical pulses with spectral phase interferometry for direct electric-field reconstruction. *Opt. Lett.* **24**: 1314–1316.

Girkin, J.M., Poland, S., and Wright, A.J. (2009) Adaptive optics for deeper imaging of biological samples. *Curr. Opin. Biotechnol.* **20**: 106–110.

Gould, T.J., Burke, D., Bewersdorf, J., and Booth, M.J. (2012) Adaptive optics enables 3D STED microscopy in aberrating specimens. *Opt. Express* **20**: 20998–21009.

Guild, J.B., Xu, C., and Webb, W.W. (1997) Measurement of group delay dispersion of high numerical aperture objective lenses using two-photon excited fluorescence. *Appl. Opt.* **36**: 397–401.

Hell, S., Reiner, G., Cremer, C., and Stelzer, E.H.K. (1993) Aberrations in confocal fluorescence microscopy induced by mismatches in refractive index. *J. Microsc.* **169**: 391–405.

Helmchen, F. and Denk, W. (2005) Deep tissue two-photon microscopy. *Nat. Methods* **2**: 932–940.

Hofer, H., Sredar, N., Queener, H., Li, C., and Porter, J. (2011) Wavefront sensorless adaptive optics ophthalmoscopy in the human eye. *Opt. Express* **19**: 14160–14171.

Hovhannisyan, V.A., Su, P.-J., and Dong, C.Y. (2008) Characterization of optical-aberration-induced lateral and axial image inhomogeneity in multiphoton microscopy. *J. Biomed. Opt.* **13**: 44023.

Iaconis, C. and Walmsley, I.A. (1998) Spectral phase interferometry for direct electric-field reconstruction of ultrashort optical pulses. *Opt. Lett.* **23**: 792–794.

Iwaniuk, D., Rastogi, P., and Hack, E. (2011) Correcting spherical aberrations induced by an unknown medium through determination of its refractive index and thickness. *Opt. Express* **19**: 19407–19414.

Jesacher, A., Thayil, A., Grieve, K., Débarre, D., Watanabe, T., Wilson, T., et al. (2009) Adaptive harmonic generation microscopy of mammalian embryos. *Opt. Lett.* **34**: 3154–3156.

Ji, N., Milkie, D.E., and Betzig, E. (2010) Adaptive optics via pupil segmentation for high-resolution imaging in biological tissues. *Nat. Methods* **7**: 141–147.

Ji, N., Sato, T.R., and Betzig, E. (2012) Characterization and adaptive optical correction of aberrations during in vivo imaging in the mouse cortex. *Proc. Natl. Acad. Sci.* **109**: 22–27.

Kirkpatrick, S., Gelatt, C.D., and Vecchi, M.P. (1983) Optimization by simmulated annealing. *Science (80-.).* **220**: 671–680.

Kner, P., Sedat, J.W., Agard, D.A., and Kam, Z. (2010) High-resolution wide-field microscopy with adaptive optics for spherical aberration correction and motionless focusing. *J. Microsc.* **237**: 136–147.

Lechleiter, J.D., Lin, D.-T., and Sieneart, I. (2002) Multi-photon laser scanning microscopy using an acoustic optical deflector. *Biophys. J.* **83**: 2292–2299.

Lenz, M.O., Sinclair, H.G., Savell, A., Clegg, J.H., Brown, A.C.N., Davis, D.M., et al. (2014) 3-D stimulated emission depletion microscopy with programmable aberration correction. *J. Biophotonics* **7**: 29–36.

Leray, A. and Mertz, J. (2006) Rejection of two-photon fluorescence background in thick tissue by differential aberration imaging. *Opt. Express* **14**: 510–565.

Leray, A., Lillis, K., and Mertz, J. (2008) Enhanced background rejection in thick tissue with differential-aberration two-photon microscopy. *Biophys. J.* **94**: 1449–1458.

Liang, X., Hu, W., and Fu, L. (2010) Pulse compression in two-photon excitation fluorescence microscopy. *Opt. Express* **18**: 14893–14904.

Lo, W., Lin, S.-J., Jee, S.-H., Dong, C.-Y., and Sun, Y. (2005) Spherical aberration correction in multiphoton fluorescence imaging using objective correction collar. *J. Biomed. Opt.* **10**: 34006–340065.

Lubeigt, W., Poland, S.P., Valentine, G.J., Wright, A.J., Girkin, J.M., and Burns, D. (2010) Search-based active optic systems for aberration correction in time-independent applications. *Appl. Opt.* **49**: 307–314.

Man, K.-F., Tang, K.S., and Kwong, S. (1999) Genetic Algorithms: Concepts and Designs (Advanced Textbooks in Control and Signal Processing). *Springer*.

Marsh, P.N., Burns, D., and Girkin, J.M. (2003) Practical implementation of adaptive optics in multiphoton microscopy. *Opt. Express* **11**: 1123–1130.

Master, B.R. and So, P.T.C. (2008) Biomedical nonlinear optical microscopy Oxford University Press New York.

Milkie, D.E., Betzig, E., and Ji, N. (2011) Pupil-segmentation-based adaptive optical microscopy with full-pupil illumination. *Opt. Lett.* **36**: 4206–4208.

Mouroulis, P. (2008) Depth of field extension with spherical optics. *Opt. Express* **16**: 12995–13004.

Müller, M., Squier, J., and Brakenhoff, G.J. (1995) Measurement of femtosecond pulses in the focal point of a high-numerical-aperture lens by two-photon absorption. *Opt. Lett.* **20**: 1038–1040.

Müller, M., Squier, J., Wolleschensky, R., Simon, U., and Brakenhoff, G.J. (1998) Dispersion pre-compensation of 15 femtosecond optical pulses for high-numerical-aperture objectives. *J. Microsc.* **191**: 141–150.

Muller, R.A. and Buffington, A. (1974) Real-time correction of atmospherically degraded telescope images through image sharpening. *JOSA* **64**: 1200–1210.

Muriello, P.A. and Dunn, K.W. (2008) Improving signal levels in intravital multiphoton microscopy using an objective correction collar. *Opt. Commun.* **281**: 1806–1812.

Neil, M.A.A., Juskaitis, R., and Wilson, T. (1997) Method of obtaining optical sectioning by using structured light in a conventional microscope. *Opt. Lett.* **22**: 1905–1907.

Neil, M.A.A., Juskaitis, R., Booth, M.J., Wilson, T., Tanaka, T., Kawata, S., and Juškaitis, R. (2000) Adaptive aberration correction in a two-photon microscope. *J. Microsc.* **200**: 105–108.

Ogilvie, J.P., Débarre, D., Solinas, X., Martin, J.-L., Beaurepaire, E., and Joffre, M. (2006) Use of coherent control for selective two-photon fluorescence microscopy in live organisms. *Opt. Express* **14**: 759–766.

Olivier, N. (2009) Contrast mechanisms and wavefront control in coherent nonlinear microscopy.

Olivier, N., Débarre, D., and Beaurepaire, E. (2009a) Dynamic aberration correction for multiharmonic microscopy. *Opt. Lett.* **34**: 3145–3147.

Olivier, N., Mermillod-Blondin, A., Arnold, C.B., and Beaurepaire, E. (2009b) Two-photon microscopy with simultaneous standard and extended depth of field using a tunable acoustic gradient-index lens. *Opt. Lett.* **34**: 1684–1686.

Olivier, N., Aptel, F., Plamann, K., Schanne-Klein, M.-C., and Beaurepaire, E. (2010) Harmonic microscopy of isotropic and anisotropic microstructure of the human cornea. *Opt. Express* **18**: 5028–5040.

Palczewska, G., Maeda, T., Imanishi, Y., Sun, W., Chen, Y., Williams, D.R., et al. (2010) Noninvasive multiphoton fluorescence microscopy resolves retinol and retinal condensation products in mouse eyes. *Nat. Med.* **16**: 1444–1449.

Pastirk, I., Cruz, J.M. Dela, Walowicz, K.A., Lozovoy, V. V, and Dantus, M. (2003) Selective two-photon microscopy with shaped femtosecond pulses. *Opt. Express* **11**: 1695–1701.

Pawley, J.B. and Masters, B.R. (1996) Handbook of biological confocal microscopy. *Opt. Eng.* **35**: 2765–2766.

Planchon, T.A., Gao, L., Milkie, D.E., Davidson, M.W., Galbraith, J.A., Galbraith, C.G., and Betzig, E. (2011) Rapid three-dimensional isotropic imaging of living cells using Bessel beam plane illumination. *Nat. Methods* **8**: 417–423.

Quirin, S., Peterka, D.S., and Yuste, R. (2013) Instantaneous three-dimensional sensing using spatial light modulator illumination with extended depth of field imaging. *Opt. Express* **21**: 16007–16021.

Raja, A.M., Xu, S., Sun, W., Zhou, J., Tai, D.C.S., Chen, C.-S., et al. (2010) Pulse-modulated second harmonic imaging microscope quantitatively demonstrates marked increase of collagen in tumor after chemotherapy. *J. Biomed. Opt.* **15**: 56016.

Rhoades, R. and Tanner, G.A. (2003) Medical physiology Lippincott Williams & Wilkins.

Rueckel, M., Mack-Bucher, J.A., and Denk, W. (2006) Adaptive wavefront correction in two-photon microscopy using coherence-gated wavefront sensing. *Proc. Natl. Acad. Sci.* **103**: 17137–17142.

Sasaki, K., Kurokawa, K., Makita, S., and Yasuno, Y. (2012) Extended depth of focus adaptive optics spectral domain optical coherence tomography. *Biomed. Opt. Express* **3**: 2353–2370.

Schelhas, L.T., Shane, J.C., and Dantus, M. (2006) Advantages of ultrashort phase-shaped pulses for selective two-photon activation and biomedical imaging. *Nanomedicine Nanotechnology, Biol. Med.* **2**: 177–181.

Schwertner, M., Booth, M.J., Neil, M.A.A., and Wilson, T. (2004) Measurement of specimen-induced aberrations of biological samples using phase stepping interferometry. *J. Microsc.* **213**: 11–19.

Secker, G.A. and Daniels, J.T. (2009) Limbal epithelial stem cells of the cornea. Harvard Stem Cell Institute.

Shao, Y., Qin, W., Liu, H., Qu, J., Peng, X., Niu, H., and Gao, B.Z. (2012) Multifocal multiphoton microscopy based on a spatial light modulator. *Appl. Phys. B* **107**: 653–657.

Shaw, M., Hall, S., Knox, S., Stevens, R., and Paterson, C. (2010) Characterization of deformable mirrors for spherical aberration correction in optical sectioning microscopy. *Opt. Express* **18**: 6900–6913.

Sheppard, C.J.R. (1988) Aberrations in high aperture conventional and confocal imaging systems. *Appl. Opt.* **27**: 4782–4786.

Sheppard, C.J.R. and Wilson, T. (1979) Effect of spherical aberration on the imaging properties of scanning optical microscopes. *Appl. Opt.* **18**: 1058–1063.

Sherman, L., Ye, J.Y., Albert, O., and Norris, T.B. (2002) Adaptive correction of depth-induced aberrations in multiphoton scanning microscopy using a deformable mirror. *J. Microsc.* **206**: 65–71.

Simmonds, R.D. and Booth, M.J. (2013) Modelling of multi-conjugate adaptive optics for spatially variant aberrations in microscopy. *J. Opt.* **15**: 94010.

Skorsetz, M., Artal, P., and Bueno, J.M. (2014) Modal-based algorithms for sensorless adaptive optics multiphoton microscopy. In, *Focus on Microscopy Meeting, Program and Abstract Book.*, p. 321.

Szipöcs, R., Spielmann, C., Krausz, F., and Ferencz, K. (1994) Chirped multilayer coatings for broadband dispersion control in femtosecond lasers. *Opt. Lett.* **19**: 201–203.

Tang, J., Germain, R.N., and Cui, M. (2012) Superpenetration optical microscopy by iterative multiphoton adaptive compensation technique. *Proc. Natl. Acad. Sci.* **109**: 8434–8439.

Tao, X., Fernandez, B., Azucena, O., Fu, M., Garcia, D., Zuo, Y., et al. (2011) Adaptive optics confocal microscopy using direct wavefront sensing. *Opt. Lett.* **36**: 1062–1064.

Tao, X., Norton, A., Kissel, M., Azucena, O., and Kubby, J. (2013) Adaptive optical two-photon microscopy using autofluorescent guide stars. *Opt. Lett.* **38**: 5075–5078.

Thériault, G., De Koninck, Y., McCarthy, N., Koninck, Y. De, and Theriault, G. (2013) Extended depth of field microscopy for rapid volumetric two-photon imaging. *Opt. Express* **21**: 10095–10104.

Török, P., Hewlett, S.J., and Varga, P. (1997) The role of specimen-induced spherical aberration in confocal microscopy. *J. Microsc.* **188**: 158–172.

Träger, F. (2007) Springer Handbook of Lasers and Optics Träger,F. (ed) Springer New York, New York, NY.

Treacy, E. (1969) Optical pulse compression with diffraction gratings. *Quantum Electron. IEEE J.* **5**: 454–458.

Trebino, R., DeLong, K.W., Fittinghoff, D.N., Sweetser, J.N., Krumbügel, M.A., Richman, B.A., and Kane, D.J. (1997) Measuring ultrashort laser pulses in the time-frequency domain using frequency-resolved optical gating. *Rev. Sci. Instrum.* **68**: 3277–3295.

Trebino, R. and Kane, D.J. (1993) Using phase retrieval to measure the intensity and phase of ultrashort pulses: frequency-resolved optical gating. *JOSA A* **10**: 1101–1111.

Tsai, P.S., Migliori, B., Campbell, K., Kim, T.N., Kam, Z., Groisman, A., and Kleinfeld, D. (2007) Spherical aberration correction in nonlinear microscopy and optical ablation using a transparent deformable membrane. *Appl. Phys. Lett.* **91**: 191102.

Vorontsov, M. a, Carhart, G.W., and Ricklin, J.C. (1997) Adaptive phase-distortion correction based on parallel gradient-descent optimization. *Opt. Lett.* **22**: 907–909.

Vorontsov, M.A., Carhart, G.W., Cohen, M., and Cauwenberghs, G. (2000) Adaptive optics based on analog parallel stochastic optimization: analysis and experimental demonstration. *J. Opt. Soc. Am. A* **17**: 1440–1453.

Wang, K., Milkie, D.E., Saxena, A., Engerer, P., Misgeld, T., Bronner, M.E., et al. (2014) Rapid adaptive optical recovery of optimal resolution over large volumes. *Nat. Methods* **11**: 625–628.

Wang, X., Pouch, J., Anderson, J.E., Bos, P.J., Miranda, F., and Wang, B. (2004) Performance evaluation of a liquid-crystal-on-silicon spatial light modulator. *Opt. Eng.* **43**: 2769–2774.

Weiner, A.M. (2000) Femtosecond pulse shaping using spatial light modulators. *Rev. Sci. Instrum.* **71**: 1929–1960.

Weiner, A.M. (2011) Ultrafast optical pulse shaping: A tutorial review. *Opt. Commun.* **284**: 3669–3692.

Wright, A.J., Burns, D., Patterson, B.A., Poland, S.P., Valentine, G.J., and Girkin, J.M. (2005) Exploration of the optimisation algorithms used in the implementation of adaptive optics in confocal and multiphoton microscopy. *Microsc. Res. Tech.* **67**: 36–44.

Wright, A.F., Chakarova, C.F., El-Aziz, M.M.A., and Bhattacharya, S.S. (2010) Photoreceptor degeneration: genetic and mechanistic dissection of a complex trait. *Nat. Rev. Genet.* **11**: 273–284.

Xi, P., Andegeko, Y., Pestov, D., Lovozoy, V. V, and Dantus, M. (2009) Two-photon imaging using adaptive phase compensated ultrashort laser pulses. *J. Biomed. Opt.* **14**: 14002.

Xu, B., Gunn, J.M., Cruz, J.M. Dela, Lozovoy, V. V, and Dantus, M. (2006) Quantitative investigation of the MIIPS method for phase measurement and compensation of femtosecond laser pulses. *J. Opt. Soc. Am. B* **23**: 750–759.

Yuan, S. and Preza, C. (2011) Point-spread function engineering to reduce the impact of spherical aberration on 3D computational fluorescence microscopy imaging. *Opt. Express* **19**: 23298–23314.

Zeng, J., Mahou, P., Schanne-Klein, M.-C., Débarre, D., and Beaurepaire, E. (2012) 3D resolved mapping of optical aberrations in thick tissues. *Biomed. Opt. Express* **3**: 1898–1913.

Zhang, K., Zhang, L., and Weinreb, R.N. (2012) Ophthalmic drug discovery: novel targets and mechanisms for retinal diseases and glaucoma. *Nat. Rev. Drug Discov.* **11**: 541–559.

Zheng, G., Ou, X., Horstmeyer, R., and Yang, C. (2013) Characterization of spatially varying aberrations for wide field-of-view microscopy. *Opt. Express* **21**: 15131–15143.

Zhou, Y., Bifano, T., and Lin, C. (2011) Adaptive optics two-photon scanning laser fluorescence microscopy. In, *SPIE MOEMS-MEMS.*, p. 79310H–79310H.

Zipfel, W.R., Williams, R.M., and Webb, W.W. (2003) Nonlinear magic: multiphoton microscopy in the biosciences. *Nat. Biotechnol.* **21**: 1369–1377.

Zommer, S. and Ribak, E. (2006) Adaptive optics almost without wave front sensing. In, *2006 Conference on Visual Optics, Ed. WF Harris, Mopani Camp, Kruger National Park, South Africa.*

Acknowledgments

The work presented in this Thesis would not have been possible without the assistance of a lot of people. I would like to say thanks to whom have helped me finish this research, in many different ways.

First and foremost, I would like to thank my supervisor Juanma Bueno for introducing me to the world of multiphoton microscopy. I arrived as a Leonardo Da Vinci fellowship, and he gave me the opportunity of being part of the word-wide known Laboratorio de Óptica de la Universidad de Murcia (LO · UM). I greatly appreciate his supervision, guidance and tremendous support through the 4 years of my PhD. I am thankful for experiences, skills and knowledge I acquired from him to become a better scientist, not only IN the lab, but also OUT of it. He taught me how to prepare a presentation for a conference (we enjoyed much during a bunch of them, filling the gap between Santiago de Compostela and Sydney), gave me advices in writing papers and showed me how to control the "biggest and most expensive" home-made machine in the lab. Especially, I want to thank him for taking me to the bullfighting arena, where after attending the fight, we took fresh eyes to be imaged.

Equally, many thanks for the financial support and scientific help to Pablo Artal, co-supervisor of this work and group leader of the LO · UM. His advice often served me to center the research topics and avoid useless ideas to interfere.

I would like also to say thanks to the different members of the lab, motivated, talented and inspiring people: Antonio Benito, Eloy Villegas, Juan Tabernero, Pedro Prieto, Lucía Hervella, Josua Fernández, Adrián Gambín, Carmen Martínez, Juan Mompean and Alejandro Mira. Lunch and coffee breaks plenty of fruitful discussions will be always on my mind. Special thanks go to Raquel Palacios and Silvestre Manzanera for their experimental support at the beginning of this porject. I also want to remember Astrid Duque for her help during my first month in Spain. To Fran Ávila, Oscar del Barco and Geovanni Hernández…. thank you for the great time we had at different conferences (including the photo with the *nobel laureate* Stefan Hell, soon awarded with N likes in Facebook!!). Special mention goes to Esther Berrio, for always having an ear for me and for the pleasant time we had when doing the catamaran sealing course in La Manga. Further, thank goes to Benjamin Lochocki for the motivated bicycle tours at the weekends. It was a lot fun.

Over these years I shared the office with great persons, also working on their PhDs: Christina Schwarz, Emmanuel Chirre, Alex Pennos and Dimitrios Christaras. We had a great time "in&out" our European office.

Additional thanks also go to my friends in Berlin, Thomas Scheske and Lisa Hartmann. When it comes so hot in Murcia, it was nice to have a place in Berlin.

Finally, I owe special thanks to my parents, Dr. Sylvia Skorsetz and Wolfgang Skorsetz. They gave me all the freedom and they have always supported me in every possible aspect.